

(2)

RADC-TR-89-32
In-House Report
March 1989

AD-A225 643

DTIC FILE COPY



A SPATIAL FILTERING TECHNIQUE FOR REDUCING PHASE ERRORS IN AUTOMATED SWEEP-ANGLE BISTATIC SCATTERING MEASUREMENTS

Marc G . Cote

DTIC
ELECTE
AUG 23 1990
S D
Co

APPROVED FOR PUBLIC RELEASE; DISTRIBUTION UNLIMITED

ROME AIR DEVELOPMENT CENTER
Air Force Systems Command
Griffiss Air Force Base, NY 13441-5700

90 08 22 048

This report has been reviewed by the RADC Public Affairs Office (PA) and is releasable to the National Technical Information Service (NTIS). At NTIS it will be releasable to the general public, including foreign nations.

RADC TR-89-32 has been reviewed and is approved for publication.

APPROVED:



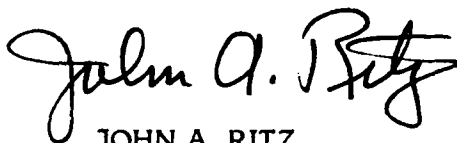
J. LEON POIRIER
Chief, Applied Electromagnetics Division
Directorate of Electromagnetics

APPROVED:



JOHN K. SCHINDLER
Director of Electromagnetics

FOR THE COMMANDER:



JOHN A. RITZ
Directorate of Plans and Programs

If your address has changed or if you wish to be removed from the RADC mailing list, or if the addressee is no longer employed by your organization, please notify RADC (EECT) Hanscom AFB MA 01731-5000. This will assist us in maintaining a current mailing list.

Do not return copies of this report unless contractual obligations or notices on a specific document requires that it be returned.

REPORT DOCUMENTATION PAGE				Form Approved OMB No. 0704-0188	
1a. REPORT SECURITY CLASSIFICATION Unclassified			1b. RESTRICTIVE MARKINGS N/A		
2a. SECURITY CLASSIFICATION AUTHORITY			3. DISTRIBUTION / AVAILABILITY OF REPORT Approved for public release, distribution unlimited.		
2b. DECLASSIFICATION / DOWNGRADING SCHEDULE					
4. PERFORMING ORGANIZATION REPORT NUMBER(S) RADC-TR-89-32			5. MONITORING ORGANIZATION REPORT NUMBER(S)		
6a. NAME OF PERFORMING ORGANIZATION Rome Air Development Center		6b. OFFICE SYMBOL (If applicable) EECT	7a. NAME OF MONITORING ORGANIZATION		
6c. ADDRESS (City, State, and ZIP Code) Hanscom AFB Massachusetts 01731-5000			7b. ADDRESS (City, State, and ZIP Code)		
8a. NAME OF FUNDING / SPONSORING ORGANIZATION		8b. OFFICE SYMBOL (If applicable)	9. PROCUREMENT INSTRUMENT IDENTIFICATION NUMBER		
8c. ADDRESS (City, State, and ZIP Code)			10. SOURCE OF FUNDING NUMBERS		
PROGRAM ELEMENT NO. 62702F		PROJECT NO. 4600	TASK NO. 15	WORK UNIT ACCESSION NO. 06	
11. TITLE (Include Security Classification) A Spatial Filtering Technique For Reducing Phase Errors in Automated Swept-Angle Bistatic Scattering Measurements					
12. PERSONAL AUTHOR(S) Marc G. Cote					
13a. TYPE OF REPORT In-House		13b. TIME COVERED FROM Nov 87 TO Aug 88	14. DATE OF REPORT (Year, Month, Day) 1989 March		15. PAGE COUNT 92
16. SUPPLEMENTARY NOTATION *NRC Fellow					
17. COSATI CODES			18. SUBJECT TERMS (Continue on reverse if necessary and identify by block number)		
FIELD 20	GROUP 14	SUB-GROUP	Swept-Angle Bistatic Scattering Measurements Spatial Filtering Bistatic RCS Measurements		
19. ABSTRACT (Continue on reverse if necessary and identify by block number) A spatial filtering scheme for reducing phase errors in electromagnetic scattering data is examined experimentally and theoretically. Measuring the coherent narrowband planewave scattering pattern of an object (target) as a continuous function of bistatic angle is difficult because the direct coupling between the transmit and receive antennas may dominate the total field. This problem can be alleviated in many cases by using a background subtraction technique. The technique requires measuring the amplitude and phase of the total electric field with and without the target. Subtracting the background field, that is, the field without the target, from the total field with the target leaves the scattered field of the target, provided multiple interactions between the target and its surroundings are negligible. Gross uncertainties in the resultant data can arise from small errors in the phase of the background data if the target scattered field is small relative to the background.					
20. DISTRIBUTION / AVAILABILITY OF ABSTRACT <input type="checkbox"/> UNCLASSIFIED / UNLIMITED <input checked="" type="checkbox"/> SAME AS RPT. <input type="checkbox"/> DTIC USERS			21. ABSTRACT SECURITY CLASSIFICATION Unclassified		
22a. NAME OF RESPONSIBLE INDIVIDUAL Marc G. Cote			22b. TELEPHONE (Include Area Code) (617) 377-4267		22c. OFFICE SYMBOL RADC/EECT

BLOCK #19 (continued)

This uncertainty shows up as high frequency variations in the target scattering pattern. To reduce this uncertainty we filter the data applying the natural $k(a + \lambda)$ spatial frequency band limit common to ordinary radiating objects.

Preface

I am indebted to Arthur D. Yaghjian for his many insightful consultations and review of the manuscript, and to James L. Schmitz and Ernest J. Yasso for their help in performing the bistatic scattering measurements.

Accession For	
NTIS - CRA&I	<input checked="" type="checkbox"/>
DTIC - TAB	<input type="checkbox"/>
Unannounced	<input type="checkbox"/>
Justification	
By	
Distribution /	
Availability Codes	
Dist	Avail. and/or Sec. Code
A-1	

Contents

1. INTRODUCTION	1
2. OBTAINING THE DATA	2
3. EFFECTS OF SAMPLING ERRORS ON THE MEASURED SCATTERED FIELD	5
4. SPATIAL FILTER	28
5. EXAMPLES OF SPATIAL FILTERING APPLIED TO THE MEASUREMENT OF BISTATIC SCATTERING FROM METAL CUBES	40
6. SUMMARY AND CONCLUSIONS	51
REFERENCES	57
APPENDIX A: DISCUSSION OF THE GENERAL BEHAVIOR OF SCATTERING FROM TARGETS OF FINITE SIZE.	59
APPENDIX B: A DEMONSTRATION OF THE PHYSICAL BAND LIMIT OF A GENERAL TARGET	77
BIBLIOGRAPHY	81

Illustrations

1.	Geometry of the Automated Swept-Angle Bistatic Scattering Measurement System.	3
2.	Inside the Anechoic Chamber of the RADC Automated Swept-Angle Bistatic Scattering Measurement System.	4
3.	Error (U) in the Measured Scattered Field Versus Phase Error in the Background Field for 5 Different Background to True-Scattered-Field Ratios.	6
4(a).	Total Field with Aluminum Cube (side length = 1.5λ) Present and Background Field.	7
4(b).	Phase of the Total Field (E_t) with Target Present.	8
4(c).	Phase of the Background Field (E_b) (Target not present).	9
5(a).	Direct Coupling Path Length and its First Derivative with Respect to Bistatic Angle.	10
5(b).	Phase of Direct Coupling Path Normalized to the Measured Background Phase at Forward Scatter ($\theta = 180^\circ$) for the X-Band Wavelength of 2.667 Centimeters.	11
6(a).	Measured E-Plane Scattered Electric Field of an Aluminum Cube with Side Length 1.5λ	12
6(b).	Measured E-Plane Scattered Electric Field of an Aluminum Cube with Side Length 1.5λ	13
7(a).	Amplitude of the True E-Plane Scattered Electric Field of an Aluminum Cube with Side Length 1.5λ as Computed Using a Uniform High-Frequency Diffraction Solution. ²	14

7(b). Phase of the True E-Plane Scattered Electric Field of an Aluminum Cube with Side Length 1.5λ as Computed Using a Uniform High-Frequency Diffraction Solution. ²	15
8(a). Amplitude of the Background Field Relative to the True Scattered Field of an Aluminum Cube (Side Length = 1.5λ) for Broadside Plane-Wave Incidence.	16
8(b). Phase Difference Between the Measured Background Field and the True Scattered Field of an Aluminum Cube (Side Length = 1.5λ) for broadside plane-wave incidence.	17
9 (a). Magnitude of the Perturbation Phasor Computed from Two Distinct Background Measurements, $E_{b1}(\theta)$ and $E_{b2}(\theta)$.	18
9(b). Phase of the Perturbation Phasor Computed from Two Distinct Background Measurements. This Gives the Phase Error Introduced in the Measured Scattered Field when Background Subtraction is Performed.	19
10(a). Predicted Error in the Measured E-Plane Scattered Field of an Aluminum Cube with Side Length 1.5λ .	20
10 (b). Actual Error in the Measured E Plane Scattered Field of an Aluminum Cube with Side Length 1.5λ .	21
11(a). Predicted Error in the Measured E-Plane Scattered Field of an Aluminum Sphere 18λ in Circumference.	22
11(b). Actual Error in the Measured E-Plane Scattered Field of an Aluminum Sphere 18λ in Circumference.	23
12(a). True E-Plane Scattered Field of a Perfectly Conducting (PEC) Sphere 18λ in Circumference Computed Using the Mie Series Solution.	24
12(b). True E-Plane Scattered Field of a PEC Sphere with 18λ Circumference.	25
13(a). Amplitude of the Measured E-Plane Scattered Field of an Aluminum Sphere with 18λ Circumference.	26
13(b). Phase of the Measured E-Plane Scattered Field of an Aluminum Sphere with 18λ Circumference.	27
14(a). Spatial Spectrum of the Measured E-Plane Scattered Field of an Aluminum Cube with Side Length 1.5λ .	30
14(b). Spatial Spectrum of True E-Plane Scattered Field of a PEC Cube with Side Length 1.5λ .	31
15(a). Amplitude of the Measured E-Plane Scattered Field of an Aluminum Cube with Side Length 1.5λ After Spatial Filtering.	32
15(b). Phase of the Measured E-Plane Scattered Field of an Aluminum Cube with Side Length 1.5λ After Spatial Filtering.	33

16.	Actual Error in the Filtered Measured E-Plane Scattered Field of an Aluminum Cube with Side Length 1.5λ .	34
17(a).	Spatial Spectrum of the Measured E Plane Scattered Field of an Aluminum Sphere with 18λ Circumference.	35
17(b).	Spatial Spectrum of the True E-Plane Scattered Field of a PEC Sphere with 18λ Circumference.	36
18(a).	Amplitude of the Measured E-Plane Scattered Field of an Aluminum Sphere with 18λ Circumference After Spatial Filtering.	37
18(b).	Phase of the Measured E-Plane Scattered Field of an Aluminum Sphere with 18λ Circumference After Spatial Filtering.	38
19.	Actual Error in the Filtered Measured E-Plane Scattered Field of an Aluminum Sphere with 18λ Circumference.	39
20(a).	Measured E-Plane RCS of an Aluminum Cube with Side Length 1.5λ Before Spatial Filtering and with the Backscattering Lobe Artificially Fit to the $\sin(x)/x$ Function.	41
20(b).	Measured E-Plane RCS of an Aluminum Cube with Side Length 1.5λ After Spatial Filtering.	42
21(a).	Measured 45° -Plane RCS of an Aluminum Cube with Side Length 1.5λ Before Spatial Filtering and with the Backscattering Lobe Artificially Fit to the $\sin(x)/x$ Function.	43
21(b).	Measured 45° -Plane RCS of an Aluminum Cube with Side Length 1.5λ After Spatial Filtering.	44
22.	Scattering from Cube with Side Length 1.5λ .	45
23(a).	Measured E-Plane RCS of an Aluminum Cube with Side Length 3.0λ Before Spatial Filtering and with the Backscattering Lobe Artificially Fit to the $\sin(x)/x$ Function.	46
23(b).	Measured E-Plane RCS of an Aluminum Cube with Side Length 3.0λ After Spatial Filtering.	47
24(a).	Measured 45° -Plane RCS of an Aluminum Cube with Side Length 3.0λ Before Spatial Filtering and with the Backscattering Lobe Artificially Fit to the $\sin(x)/x$ Function.	48
24(b).	Measured 45° -Plane RCS of an Aluminum Cube with Side Length 3.0λ After Spatial Filtering.	49
25.	Scattering from Cube with Side Length 3.0λ .	50
26(a).	Measured E-Plane RCS of an Aluminum Cube with Side Length 3.0λ Before Spatial Filtering and With Both Forward-Scattering and Backscattering Lobes Artificially Set to a Constant.	52

26(b). Measured E-Plane RCS of an Aluminum Cube with Side Length 3.0λ After Spatial Filtering.	53
27. Scattering from Cube with Side Length 3.0λ .	54
A1(a). Geometry, and Measurement Parameters for E-Plane Scattering from an Aluminum Cube with a Side Length of 0.75λ . [Example 1 page 1]	61
A1(b). Measured Background Field (Amplitude and Phase) Associated with Scattering from a 0.75λ Cube. [Example 1 page 2]	62
A1(c). Measured Total Field (Amplitude and Phase) Associated with Scattering from a 0.75λ Cube. [Example 1 page 3]	63
A1(d). Measured Scattered Field (Amplitude and Phase) of an Aluminum Cube with Side Length 0.75λ . [Example 1 page 4]	64
A1(e). Spatial Spectra of the Background, Total, and Target Scattered Fields Associated with Scattering From a 0.75λ Cube. [Example 1 page 5]	65
A2(a). Geometry, and Measurement Parameters for E-Plane Scattering From an Aluminum Cube with a Side Length of 5.0λ . [Example 2 page 1]	66
A2(b). Measured Background Field (Amplitude and Phase) Associated With Scattering From a 5.0λ Cube. [Example 2 page 2]	67
A2(c). Measured Total Field (Amplitude and Phase) Associated With Scattering From a 5.0λ Cube. [Example 2 page 3]	68
A2(d). Measured Scattered Field (Amplitude and Phase) of an Aluminum Cube With Side Length 5.0λ . [Example 2 page 4]	69
A2(e). Spatial Spectra of the Background, Total, and Target Scattered Fields Associated with Scattering from a 5.0λ Cube. [Example 2 page 5]	70
A3(a). Geometry, and Measurement Parameters for H-Plane Scattering From an Aluminum Sphere 17.95λ in Circumference. [Example 3 page 1]	71
A3(b). Measured Background Field (Amplitude and Phase) Associated with Scattering From a 17.95λ Sphere. [Example 3 page 2]	72
A3(c). Measured Total Field (Amplitude and Phase) Associated with Scattering From a 17.95λ Sphere. [Example 3 page 3]	73
A3(d). Measured Scattered Field (Amplitude and Phase) of an Aluminum Sphere With Circumference 17.95λ . [Example 3 page 4]	74
A3(e). Spatial Spectra of the Background, Total, and Target Scattered Fields Associated with Scattering from a 17.95λ Sphere. [Example 3 page 5]	75

Table

1. Truncation criterion.

79

A Spatial Technique for Reducing Phase Errors in Automated Swept-Angle Bistatic Scattering Measurements

1. INTRODUCTION

This report describes and examines a spatial filtering technique for reducing phase errors in measured electromagnetic swept-angle bistatic scattering data.

Measuring the coherent narrow-band plane-wave scattering pattern of a low radar cross section (RCS) target like a cone sphere, as a continuous function of bistatic angle, is difficult because the direct coupling between the transmit and receive antennas often dominates the total field over a wide range of bistatic angles. The experimental technique requires measuring the amplitude and phase of the electric field with and without the target. Subtracting the field without the target (background field) from the field with the target leaves the measured scattered field of the target, provided the multiple interactions between the target and its surroundings are negligible. The accuracy of the measured scattered field is directly related to the relative intensities of the background and target scattered fields. If the target scattered field is small relative to the background, gross errors in the measured target RCS arise from small phase errors in the background field when the background field is subtracted from the total field to obtain the measured target RCS. For a 10 dB background-to-target ratio, a 5 degree phase error in the measured background produces a 90 percent error in the amplitude of the measured electric field scattered by the target. This error shows up as high-frequency variations in the measured target scattering pattern. We show that this prohibitive error can be minimized by filtering the data and

(Received for publication 5 April 1989)

applying the natural $k(a + \lambda)^{1/2}$ spatial frequency band limit common to ordinary radiating objects. The bandlimited filtering has allowed the accurate automated measurement of bistatic scattering from targets with regions of low RCS.

2. OBTAINING THE DATA

The measurement geometry used is sketched in Figure 1. The transmitting antenna is located along the z-axis sufficiently far from the origin to ensure that the incident spherical wave has a nearly planar phase front over the region occupied by the target. The receiving probe can be moved along a circle centered at the origin and far enough from the target so that the scattered field is nearly planar over the probe aperture. The transmitting antenna, target, and receiving antenna subtend the bistatic angle, θ .

A typical measurement is made by fixing the transmitter and target and moving the receiving antenna along the circular path in θ , recording the amplitude and phase of the voltage at the terminal of the receiving antenna relative to a sample of the stable, coherent narrow-band, continuous-wave transmitted signal, at regular bistatic angle intervals. The recorded voltages are proportional to the component of the total electric field aligned with the polarization of the receiving antenna. The total electric field component polarized with the receiving antenna E_t can be written as the phasor sum of the three terms: background field E_b , true target scattered field E_s , and multiple interaction field E_m . Symbolically the total field is:

$$E_t = E_b + E_s + E_m. \quad (1)$$

The background field is made up of the incident field plus the scattered field that exists when the target is not present. This component is dominated by the incident field, especially in the forward scattering region. The multiple interaction field contributes to the total field through multiple interactions of the target with its surroundings. This component depends on the scatterer and typically can be made negligible by using radar absorbing materials (RAM) and target support structures with low dielectric constant. For the rest of this report we assume E_m is negligible. The target scattered field is the quantity of interest to be extracted from the total field. An experimental determination of the true target scattered field can be made by measuring the total field with the target removed (the background) and the total field with the target in place, and subtracting the two data sets. We assume that the incident field and the target surroundings are the same for the two measurements. The accuracy of the resulting target scattered field will depend on how precisely the spatial sampling with the target in place was repeated in the background measurement. If at any bistatic angle the measurement system behaves differently during the background measurement than during the measurement of the total field with the target in place, subtracting the two data sets will result in a measured target scattered field differing from the true scattered field of the target. The formulation used here assumes that the target scattered field varies much more slowly in phase than the background field, otherwise the

¹Chu, L. J. (1948), Physical Limitations of Omni-Directional Antennas *Journal of Applied Physics*, **19**:1163-1175, December 1948.

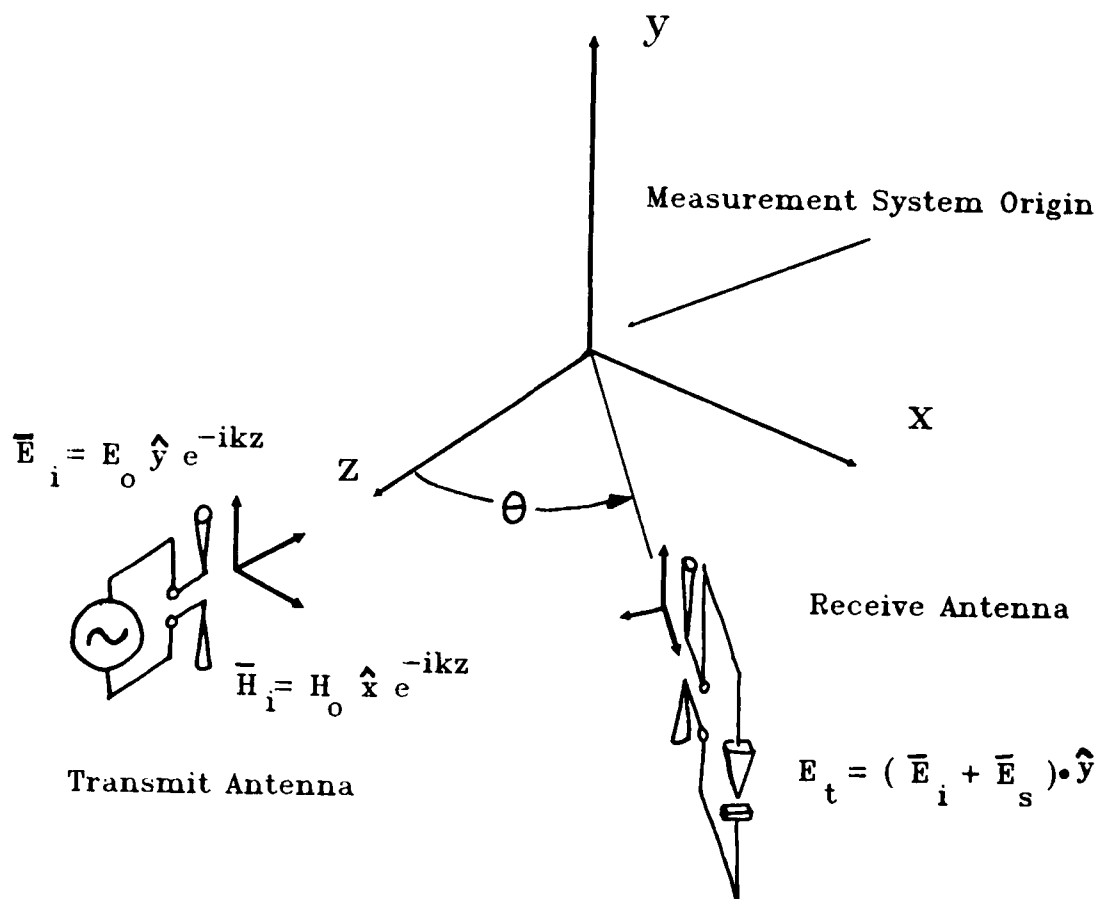


Figure 1. Geometry of the Automated Swept-Angle Bistatic Scattering Measurement System.

positioning error could significantly affect the target scattered field. This assumption allows us to treat the measured total field as the true total field and to place all the measurement error in the background field. In Appendix A we show that a typical target scattered field necessarily varies more slowly than the phase variation of the background field.

Two major sources of error account for the inaccuracies in the sampled background field: receiver amplitude and phase error, and antenna positioning error. The receiver accuracy is specified by the manufacturer. For example, under typical measurement conditions, the receiver (Scientific Atlanta (SA) model-1783) used in Rome Air Development Center's (RADC) RCS measurement system is rated to give amplitude data accurate to within 0.05 dB per 10 dB separation from the reference RF-power level and relative phase data accurate to within 0.4 degree per 10 dB separation from the reference RF-power level. The accuracy specifications of the receiver determines the highest accuracy achievable for the measurement system. In practice, the RADC/EECT system provides a maximum accuracy of 99.3 percent for the measured scattered field amplitude of a typical scatterer in the forward scattering region. The positioning mechanism is responsible for three related spatial sampling errors: the rotating positioner, sampling integration, and the transmitting antenna mount. First, the rotating positioner's rated

error is a significant source of phase measurement errors. The RADC/EECT positioner (SA model-1562) is capable of repeatedly positioning the rotating antenna (transmitting antenna in our measurements) to within 0.03 degree of any given angle. This accuracy specification translates to a spatial deviation of $0.03\pi/180$ at a distance r units from the center of rotation of the positioner. The fixed receiving probe is located about 3.5 meters from the center of the positioner which means that a positioning error of as much as 0.2 cm is possible. At X-band, 0.2 cm is 7 percent of a wavelength or about 25 degrees. This may be a significant phase error, as we show in Section 3. Second, there are sources of error in the sampling integration interval. Because the receiving probe moves at a constant angular velocity (as viewed from the rotating target-transmitting-antenna boom) during an entire data collection run, each field sample is really an integration of the field over the interval that the receiving antenna moves (window) in the time it takes the receiver to take one sample. For the RADC/EECT system, the integration window is typically 0.1 degree, which leads to a negligible error, since the fields vary slowly (<1.0 dB/degree) in amplitude and are nearly constant in phase. Third, vibrations and shifts of the transmitting antenna may lead to phase measurement errors. In the RADC/EECT system (see Figure 2) the receiving antenna is fastened to the wall of an anechoic chamber, while the

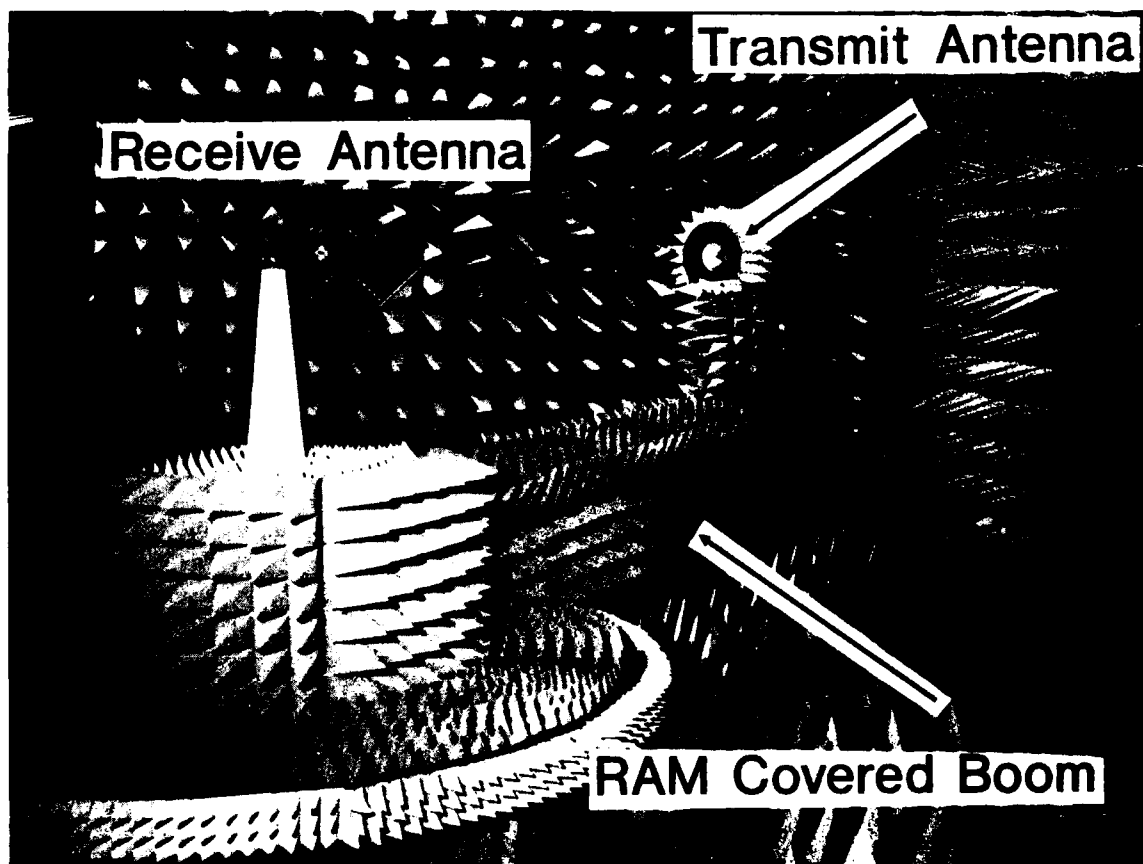


Figure 2. Inside the Anechoic Chamber of the RADC Automated Swept-Angle Bistatic Scattering Measurement System.

transmitting antenna is fastened to the end of a trussed wooden boom, with the other end bolted to the azimuth positioner. The target transmitting antenna assembly rotates at a constant angular velocity during a typical measurement. The transmitting antenna, located at the end of the long (3m) boom, may vibrate and shift slightly when it is accelerated up to speed at the start of each measurement. This source of sampling error has been estimated at 0.32 cm maximum, tangent to the measuring circle, or 0.6 degree in bistatic angle. This may cause a phase error of up to 35 degrees at X-band.

3. EFFECTS OF SAMPLING ERRORS ON THE MEASURED SCATTERED FIELD

As explained in Section 2, the measured scattered field of the target is extracted from the measured total field by subtracting two data sets, one collected with the target present [measured total field, $E_t(\theta)$, which is taken as the true total field] and the other collected without the target [measured background field, $E'_b(\theta)$, which may contain errors]. In this section we discuss the effect of the inaccuracies in the measurement of the background field on the measurement of the scattered field, $E'_s(\theta)$.

Neglecting target-surrounding interactions ($E_m \rightarrow 0$) we can write the measured total field as the phasor sum of the true target scattered field and the true background field [note Eq. (1)].

$$E_t(\theta) = E_s(\theta) + E_b(\theta). \quad (2)$$

To understand how sampling errors affect the measured scattered field, we assume that the measured background field is related to the true background component of the measured total field by:

$$E'_b(\theta) = E_b(\theta) \epsilon(\theta). \quad (3)$$

where ϵ is a phasor quantity representing a perturbation that might be caused by sampling errors. The measured scattered field of the target is given by

$$E'_s(\theta) = E_t(\theta) - E'_b(\theta). \quad (4)$$

Substituting the expressions for $E_t(\theta)$ and $E'_b(\theta)$ from Eq. (2) and (3) into Eq. (4), we obtain an expression for the measured scattered field in terms of the perturbation phasor:

$$E'_s(\theta) = E_s(\theta) + E_b(\theta)(1 - \epsilon(\theta)). \quad (5)$$

We define the phasor error $U(\theta)$ as the difference between the measured and the true scattered-fields divided by the true scattered field. Expressed mathematically we have,

$$U(\theta) = \frac{E'_s(\theta) - E_s(\theta)}{E_s(\theta)}. \quad (6)$$

Replacing the measured scattered field in Eq. (6) with its equivalent found in Eq. (5), we find the error to be

$$U(\theta) = \frac{E_b(\theta)}{E_s(\theta)} [1 - \epsilon(\theta)]. \quad (7)$$

Equation (7) shows that the error⁹ in the measured scattered field is proportional to the relative amplitudes of the measured background field and the true scattered field of the target. This suggests the expected result that larger sampling errors can be tolerated in regions of high target scattered fields relative to the background field. Figure 3 shows the error in the measured scattered field (U) versus phase error in the background field for a constant background amplitude error of 25 percent. The error is plotted for five different background-to-scattered-field

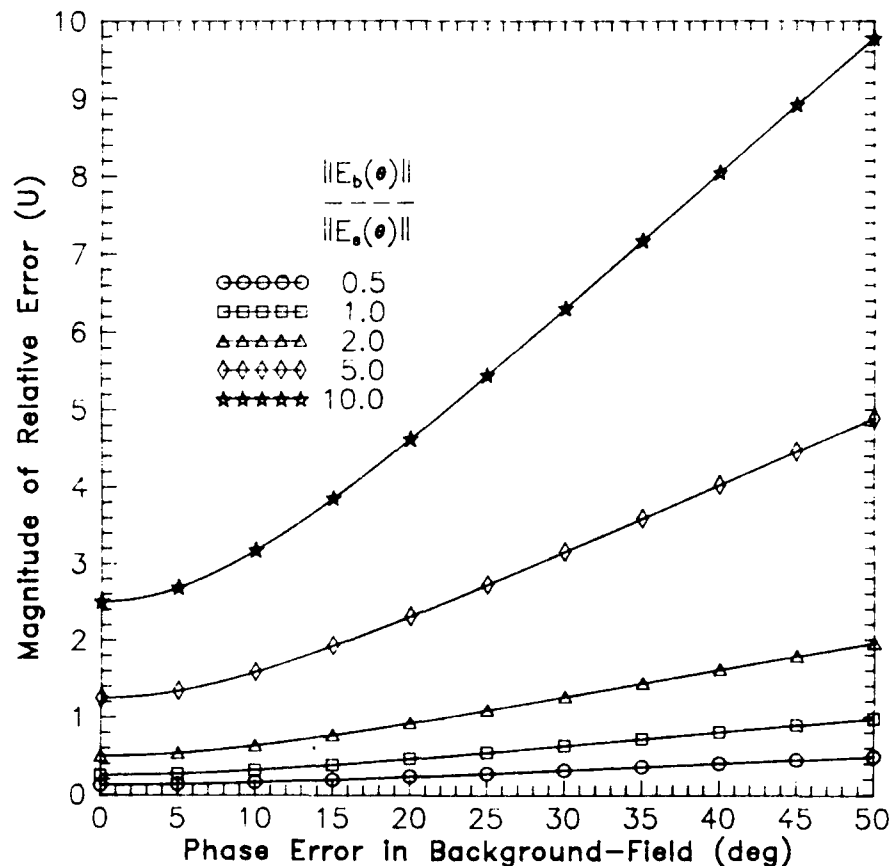


Figure 3. Error (U) in the Measured Scattered Field Versus Phase Error in the Background Field for 5 Different Background to True-Scattered-Field Ratios. A constant background amplitude error of 25% is assumed.

⁹Blacksmith, P., Hiatt, R. E., and Mack, R. B., "Introduction to Radar Cross-Section Measurements," *Proceedings of the IEEE*, Vol. 53, No. 8, pp. 901-920, August 1965.

ratios. From the curves we can see that a small phase error can cause an appreciable error in the measured scattered field. For example, a phase error of 25 degrees causes a 280 percent error in the scattered field in regions where the background is five times higher (that is, 7 dB greater) than the true scattered field of the target.

We investigate the error further with an example. For this example, a y-polarized, z-directed CW plane-wave illuminates an aluminum cube with a side length of 1.5λ . The receiving probe is moved in the $\phi = 90^\circ$ plane (E-plane) along a circular arc centered at the origin, and the directed component of the total electric field (E_t) is recorded at every 0.2° over the interval $0^\circ \leq \theta \leq 180^\circ$. The cube is then removed from the anechoic chamber and the measurement repeated, this time recording the background field E_b . Amplitude* and phase plots of E_t and E_b are shown in Figure 4. The amplitude plots [Figure 4(a)] show that the total field and the background field approach

*The amplitude plots are not strictly the amplitude of the electric field, but are the square root of the radar cross section (RCS) and have units of meters. The plotted values are proportional to the electric field aligned with the receiver polarization. For the remainder of this report the plotted values referred to as the amplitude of the electric field are $\sqrt{\text{RCS}}$ in meters.

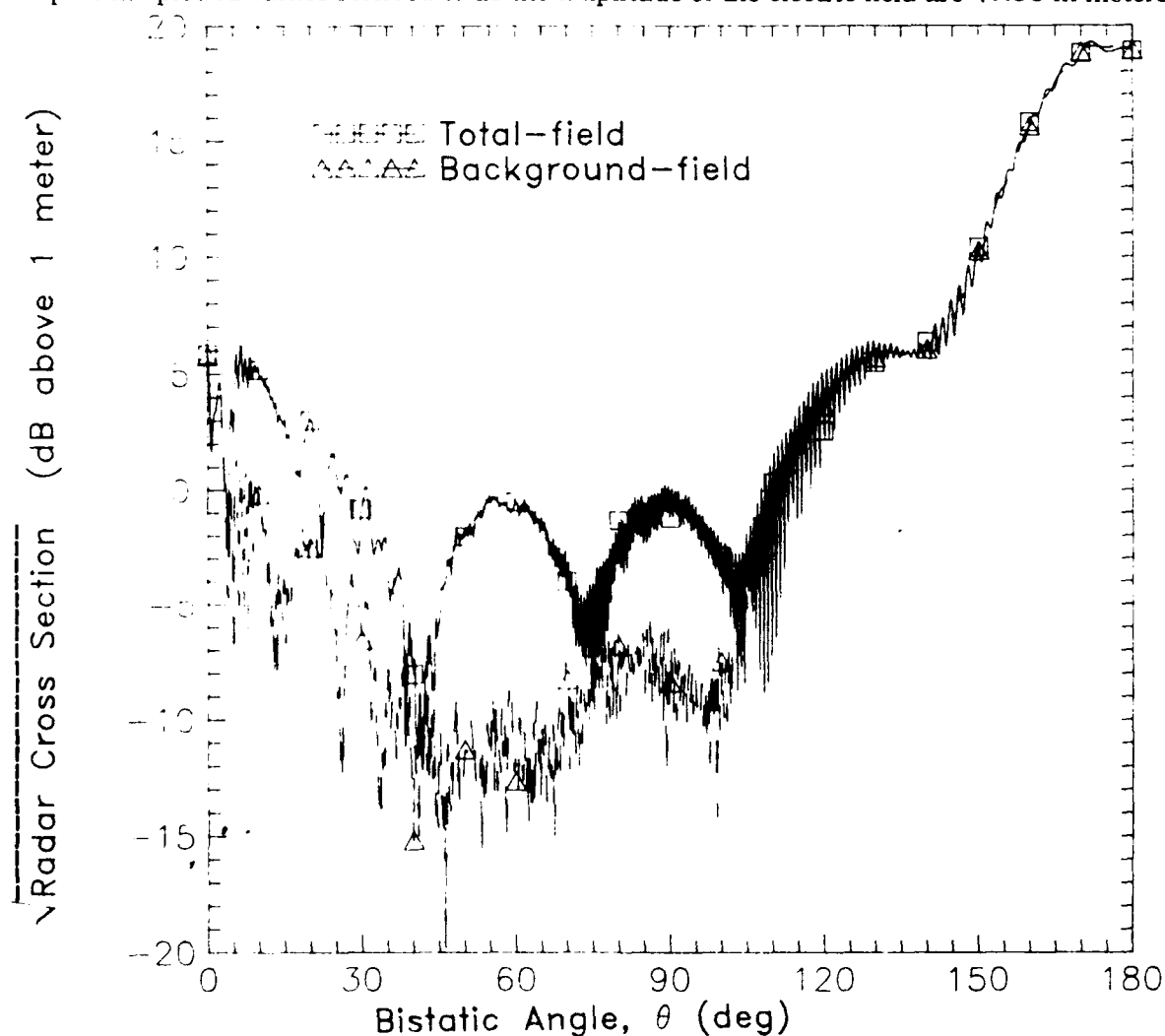


Figure 4(a). Total Field with Aluminum Cube (side length = 1.5λ) Present and Background Field.

the same intensity level as the bistatic angle increases toward forward scatter. This is what we expect because in the forward scattering region the main beam of the receiving probe overlaps the main beam of the transmitting antenna and significantly increases the antenna-antenna coupling. The graph shows that this direct coupling dominates the total field in the forward scattering region. The phase plots [Figures 4(b) and 4(c)] also show that the forward scattering region is dominated by the direct coupling field. For observation angles less than about 100 degrees, the phase of the total field [target present, Figure 4(b)] varies slowly as one would expect (see Appendix A). As the observation angle increases past 100 degrees the phase suddenly begins to vary much faster (this is where the direct coupling component becomes dominant) and then the variation slows near forward scatter. The phase of the background field [Figure 4(c)] changes rapidly throughout the observation sector, but in the forward scattering region it has the same behavior as the phase of the total field. The variation in the rate of change of the phase with

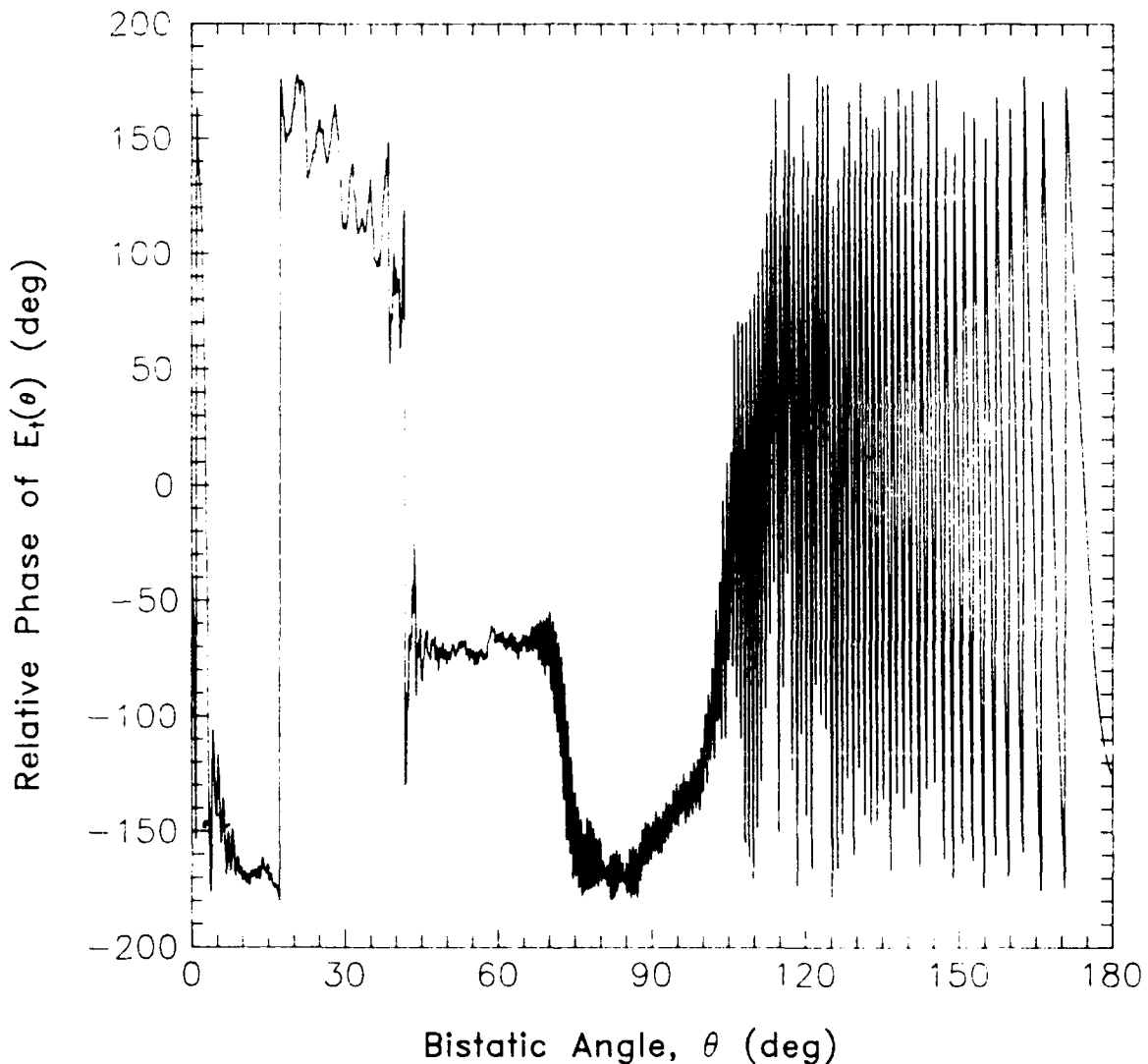


Figure 4(b). Phase of the Total Field (E_t) with Target Present.

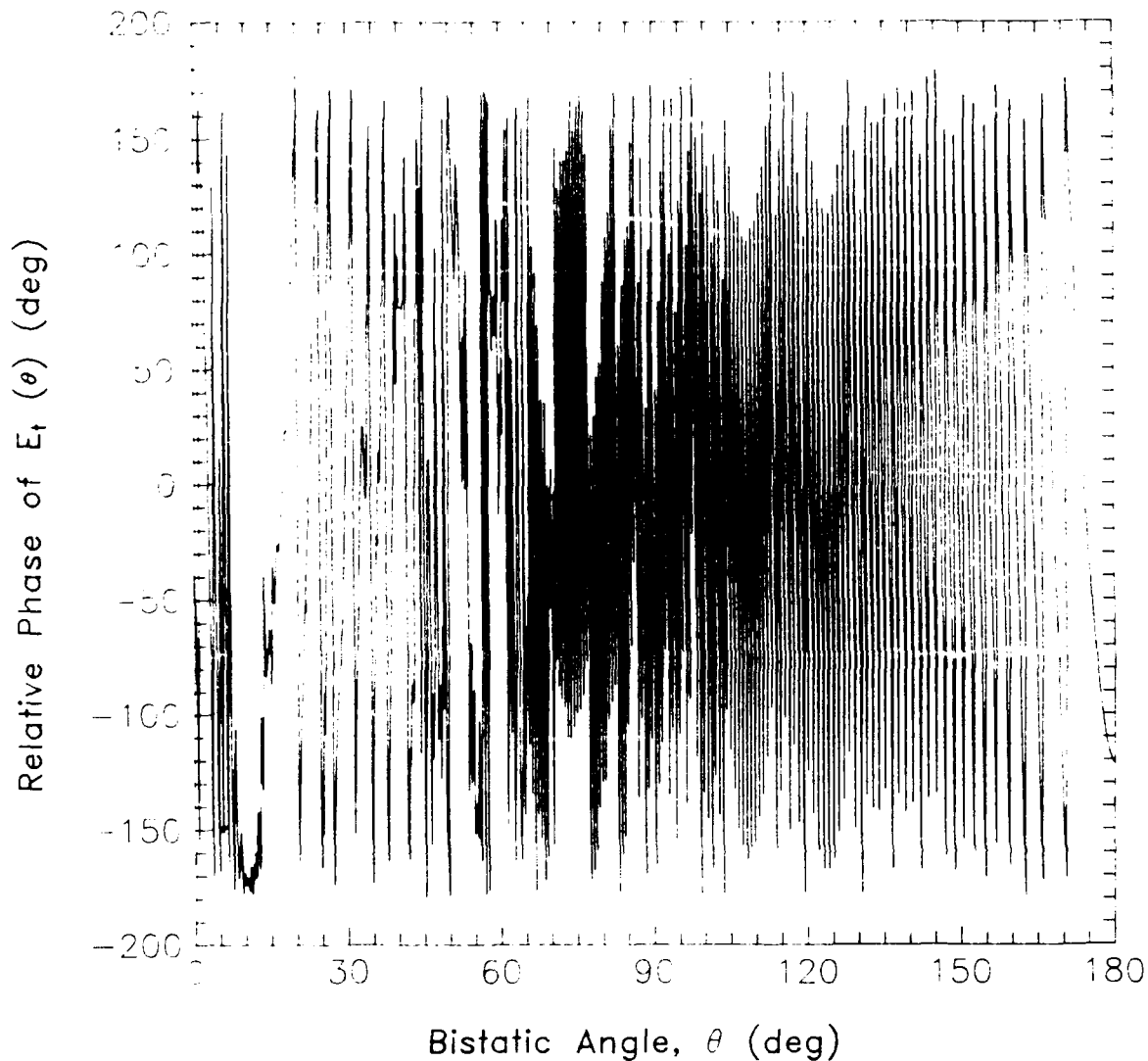


Figure 4(c). Phase of the Background Field (E_b) (Target not present).

observation angle is completely consistent with what one calculates for the rate of change of phase due to the changes in direct coupling path length. Figure 5(a) shows the antenna-antenna coupling path length (solid line) as a function of observation angle, and the rate of change in the path length (dashed line) with observation angle. The phase due to path length changes is plotted in Figure 5(b). In the forward scattering region ($\theta > 120^\circ$) the computed phase curve matches the measured curves for both the total and the background fields.

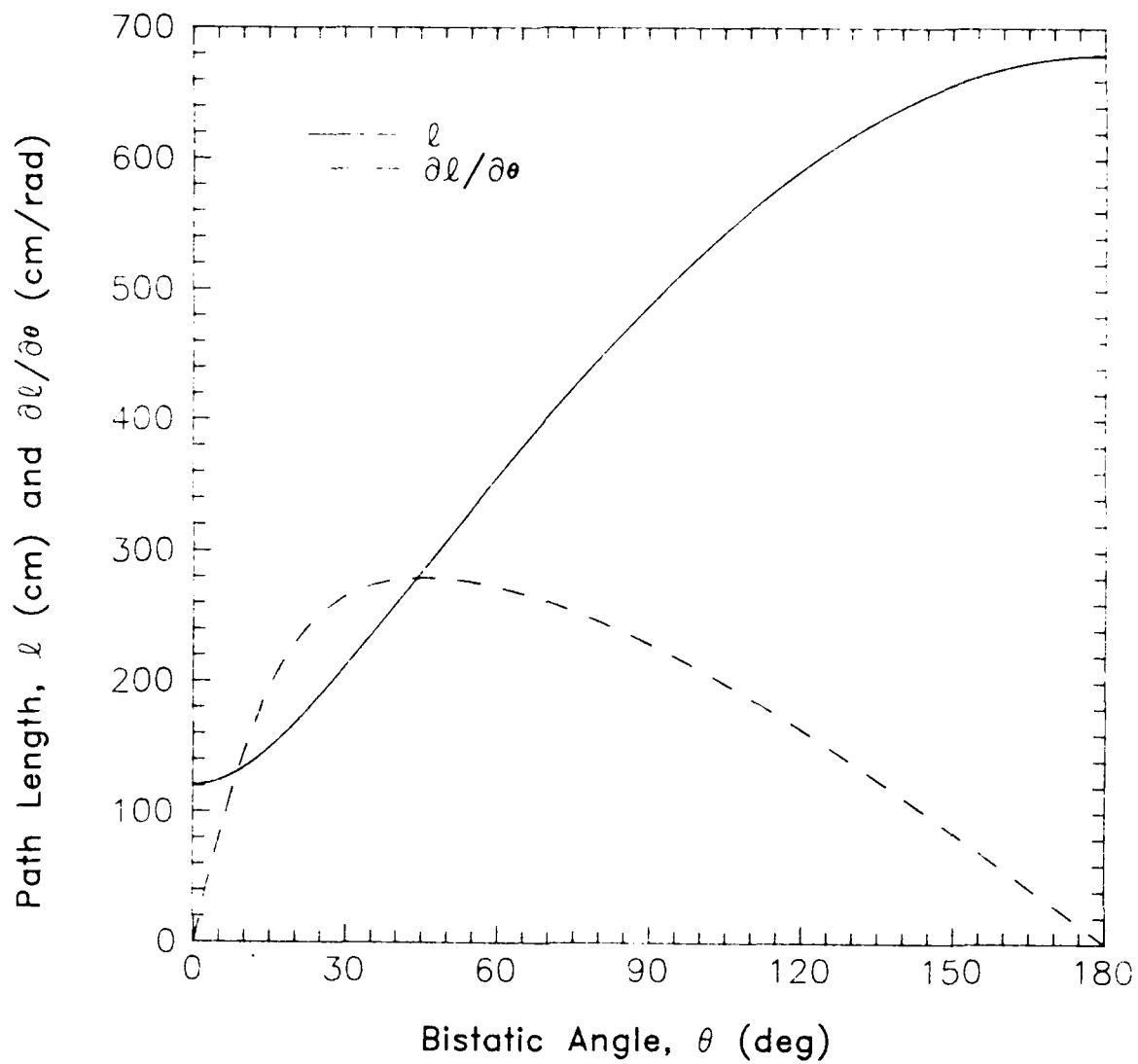


Figure 5(a). Direct Coupling Path Length and its First Derivative with Respect to Bistatic Angle.

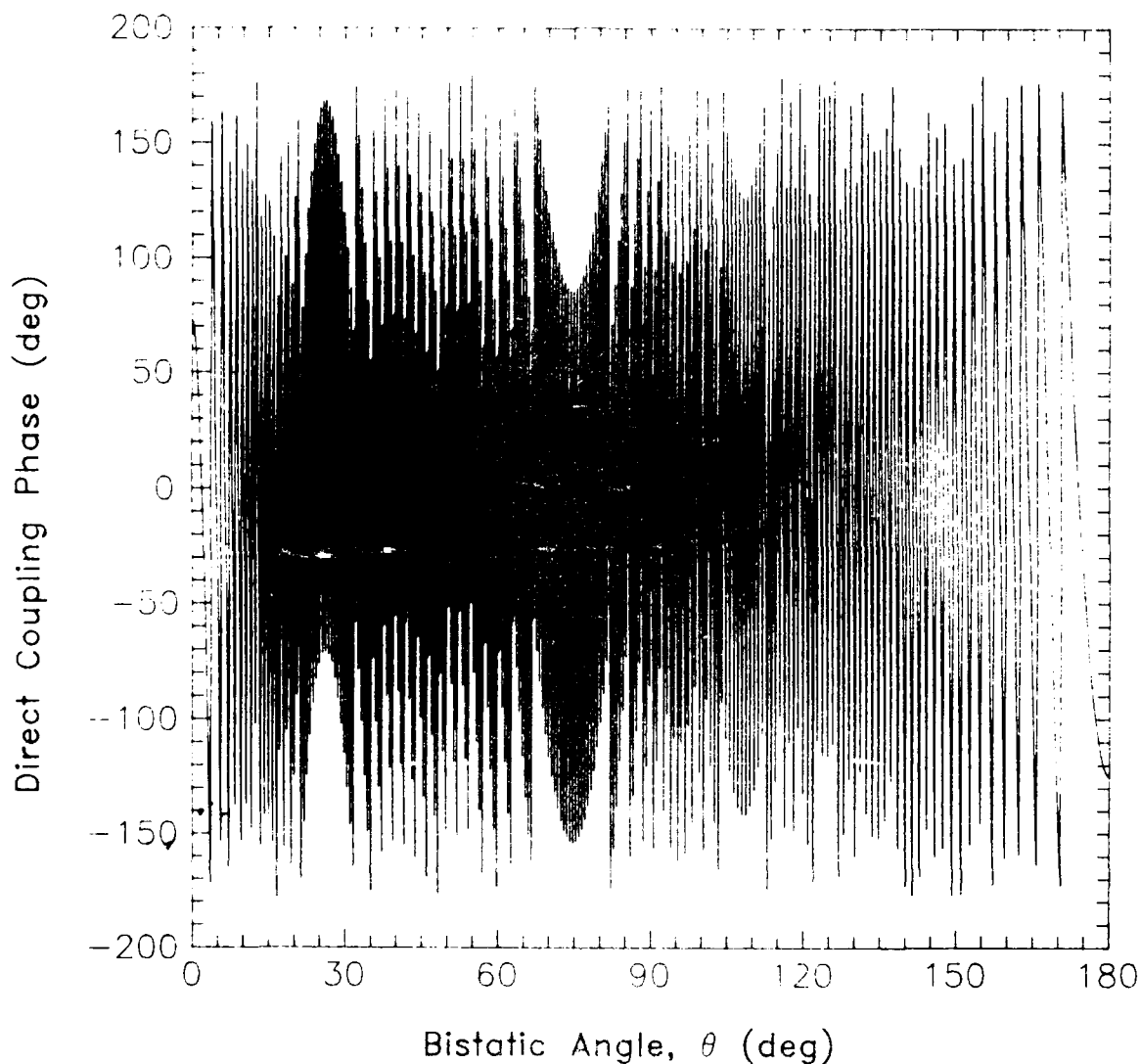


Figure 5(b). Phase of Direct Coupling Path Normalized to the Measured Background Phase at Forward Scatter ($\theta = 180^\circ$) for the X-Band Wavelength of 2.667 Centimeters.

The measured scattered field $E_s(\theta)$ that results from subtracting the background field from the total field is shown in Figure 6. For observation angles less than 10 degrees, the transmitting antenna shadowed the receiving antenna, causing the sharp rise in amplitude and erratic behavior in phase. This part of the measured scattered field should be disregarded. We notice that for observation angles between 10 and 120 degrees, both the amplitude and phase of the measured scattered field are very smooth and slowly varying. For observation angles greater than 120 degrees the gross behavior of both curves is slowly varying, but there is also a rapidly varying component riding on the curves. This component is both frequency and amplitude modulated, beginning with faster variations at a low level and progressing toward slower variations at higher levels. This rapidly varying component is not part of the true target scattered field but is an error caused in part by receiver and positioning errors.

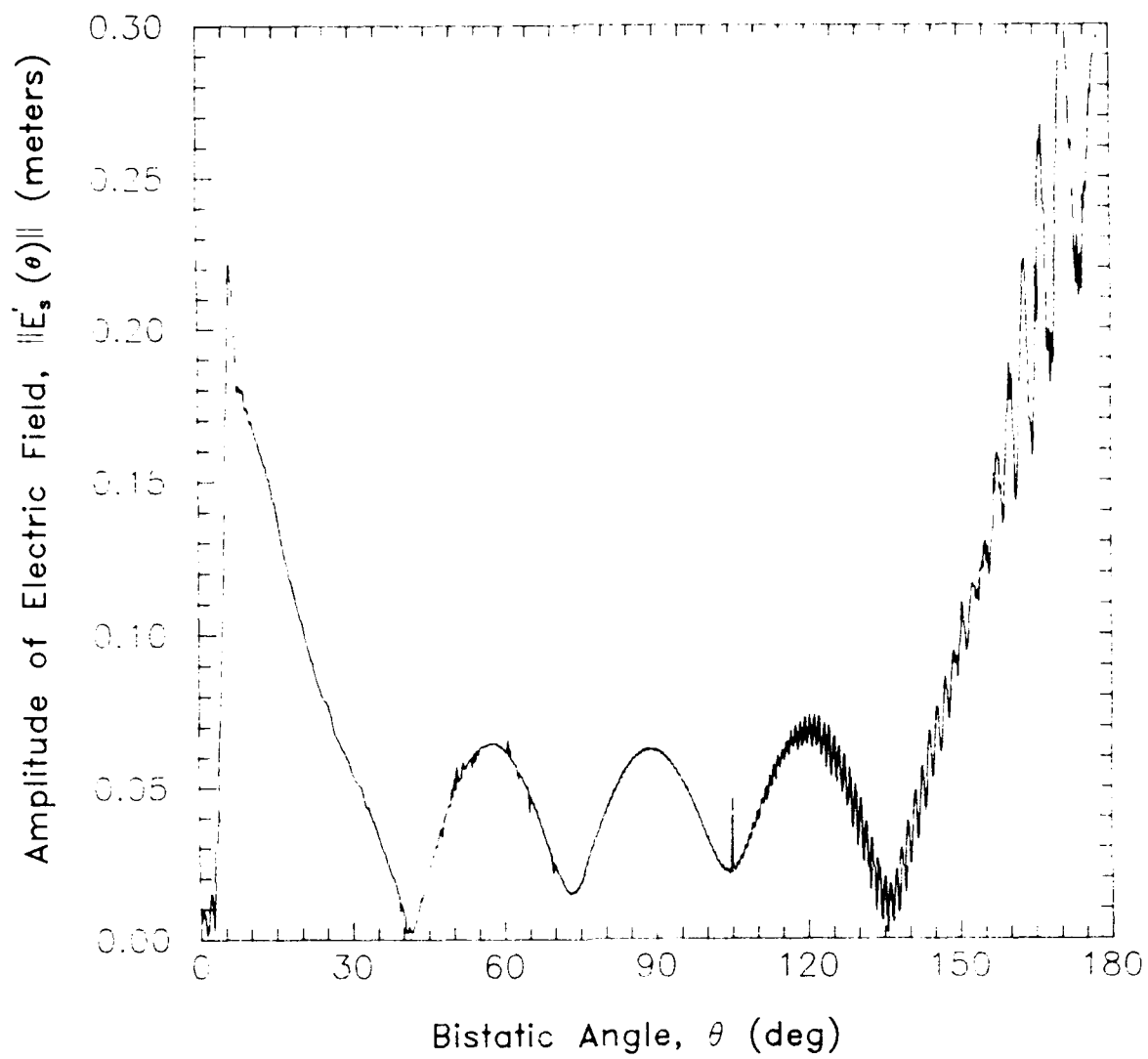


Figure 6(a). Measured E-Plane Scattered Electric Field of an Aluminum Cube with Side Length 1.5λ

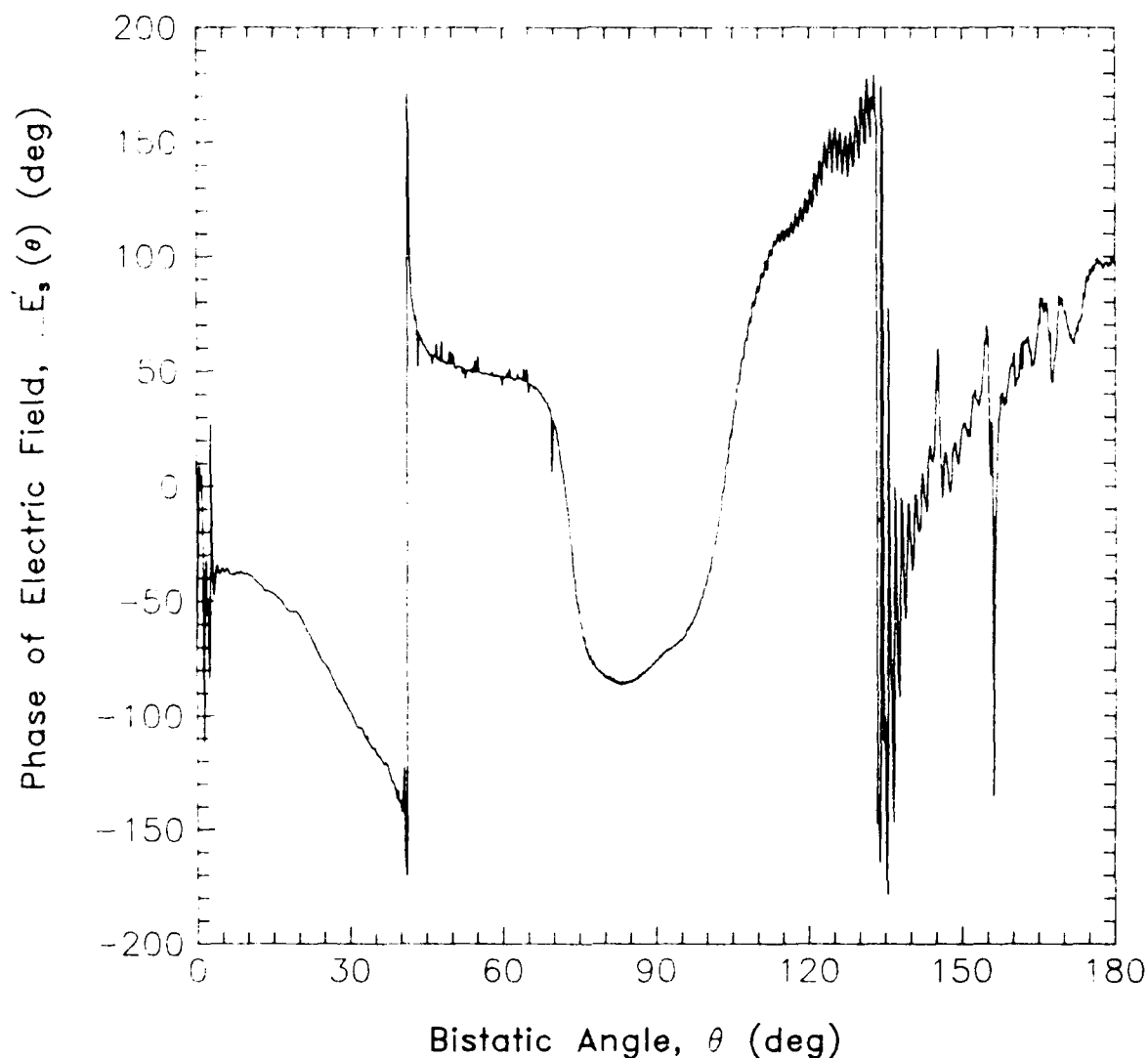


Figure 6(b). Measured E-Plane Scattered Electric Field of an Aluminum Cube with Side Length 1.5λ

According to Eq. (7), $U(\theta)$ is the product of the two factors E_b/E_s and $[1 - \epsilon(\theta)]$. We compute the first factor by dividing the measured background field E'_b (see Figure 4) by the true scattered field E_s , shown in Figure 7, computed using a uniform high-frequency diffraction solution.² A graph of this factor is shown in Figure 8. The graph exhibits the expected behavior, low in the back-scattering region and high in the forward scattering region. The sharp rise and fall occurring around $\theta = 135$ degrees is due to a deep null in the true scattered field and is not present in general. The second factor (perturbation phasor) $\epsilon(\theta)$ is estimated by dividing two background field data sets. One background field was measured before, and the other after, measuring the

²Cote M. G., Woodworth M. M., and Yaghjian A.D. (1988). "Scattering from the Perfectly Conducting Cube," *IEEE Transactions on Antennas and Propagation*, Vol. AP-36, No. 9.

total field with the target present. The amplitude and phase plots of ϵ are given in Figure 9. The reader will notice that in general $\epsilon(\theta)$ is largest where the measured background field intensity is lowest [refer to Figure 4(a), dashed line]. This phenomenon is consistent with receiver measurement error. The SA-1783 receiver rated amplitude and phase error for this example in the region where the measured power is lowest (about $\theta = 60^\circ$) are 23 percent and 6.5 degrees.

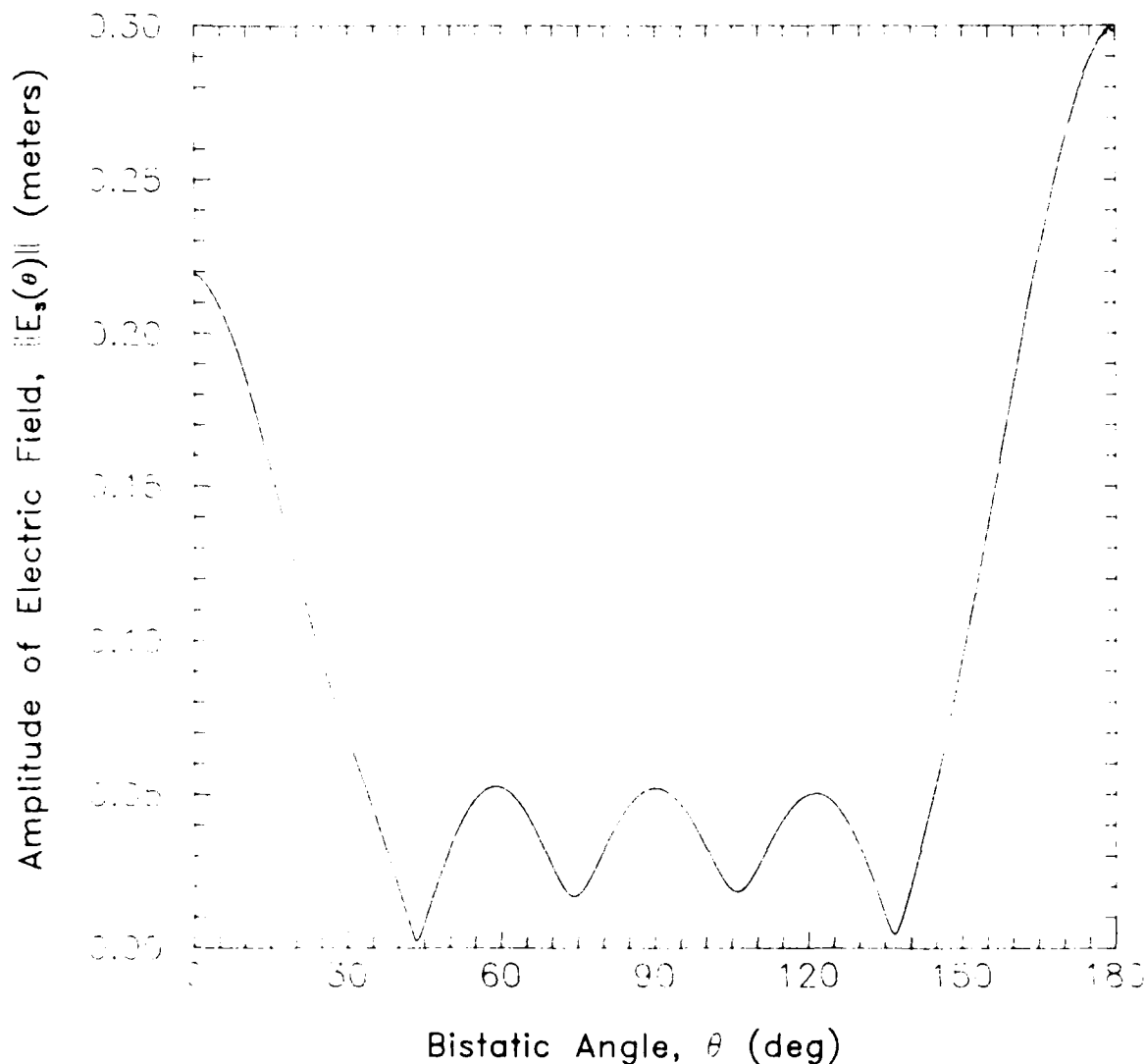


Figure 7(a). Amplitude of the True E-Plane Scattered Electric Field of an Aluminum Cube with Side Length 1.5λ as Computed Using a Uniform High-Frequency Diffraction Solution.²

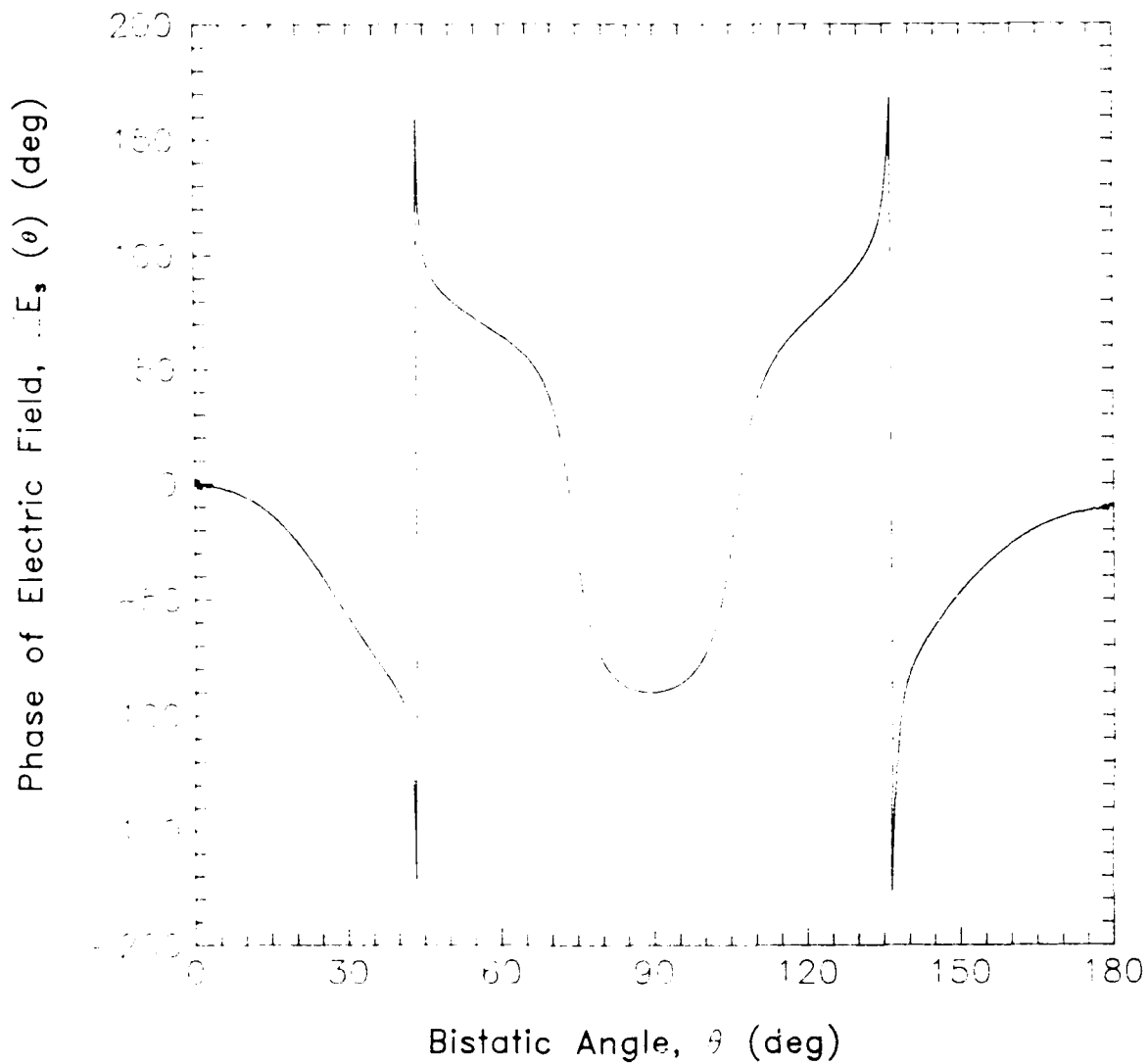


Figure 7(b). Phase of the True E-Plane Scattered Electric Field of an Aluminum Cube with Side Length 1.5λ as Computed Using a Uniform High-Frequency Diffraction Solution.²

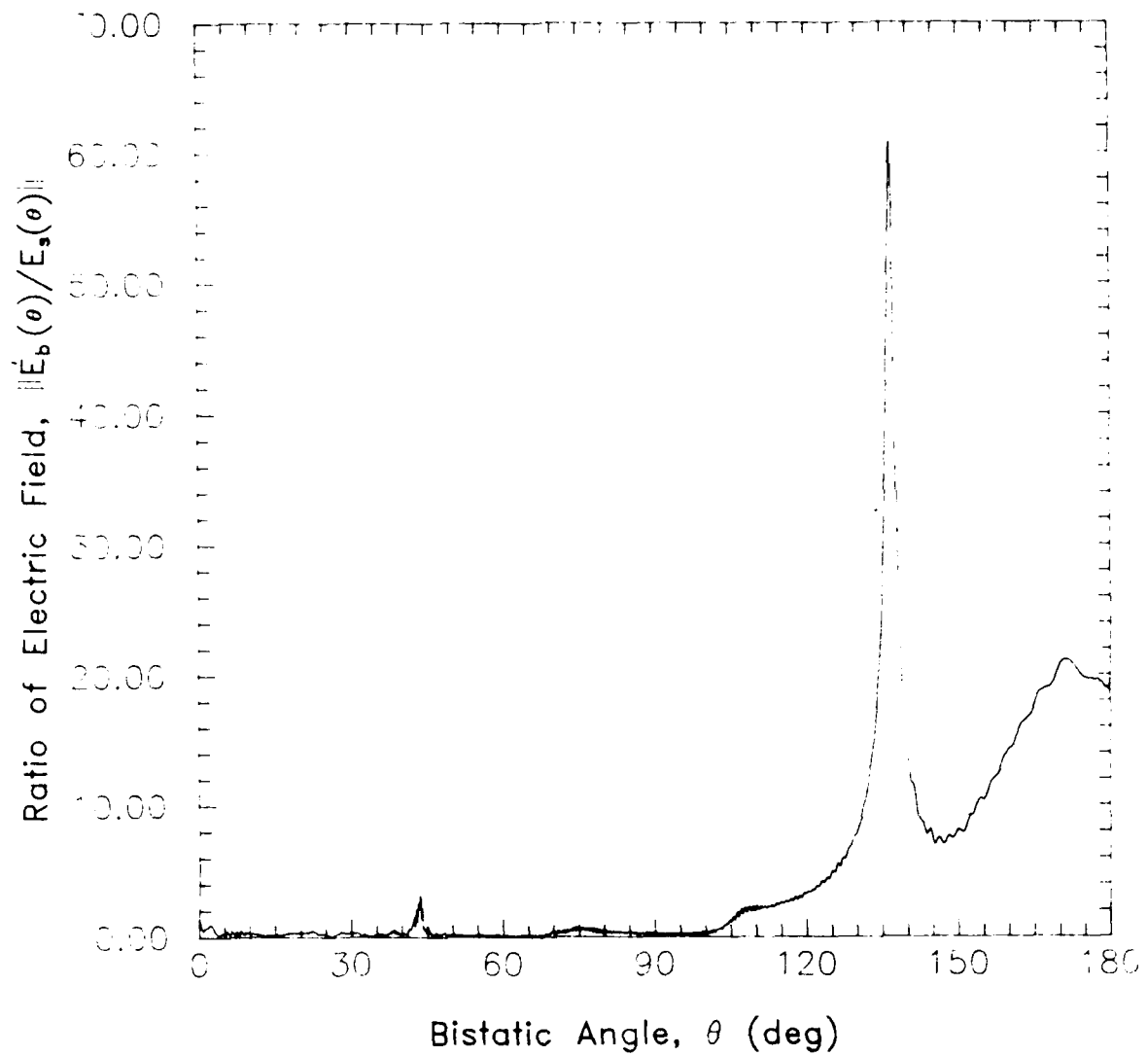


Figure 8(a). Amplitude of the Background Field Relative to the True Scattered Field of an Aluminum Cube (Side Length = 1.5λ) for Broadside Plane-Wave Incidence.

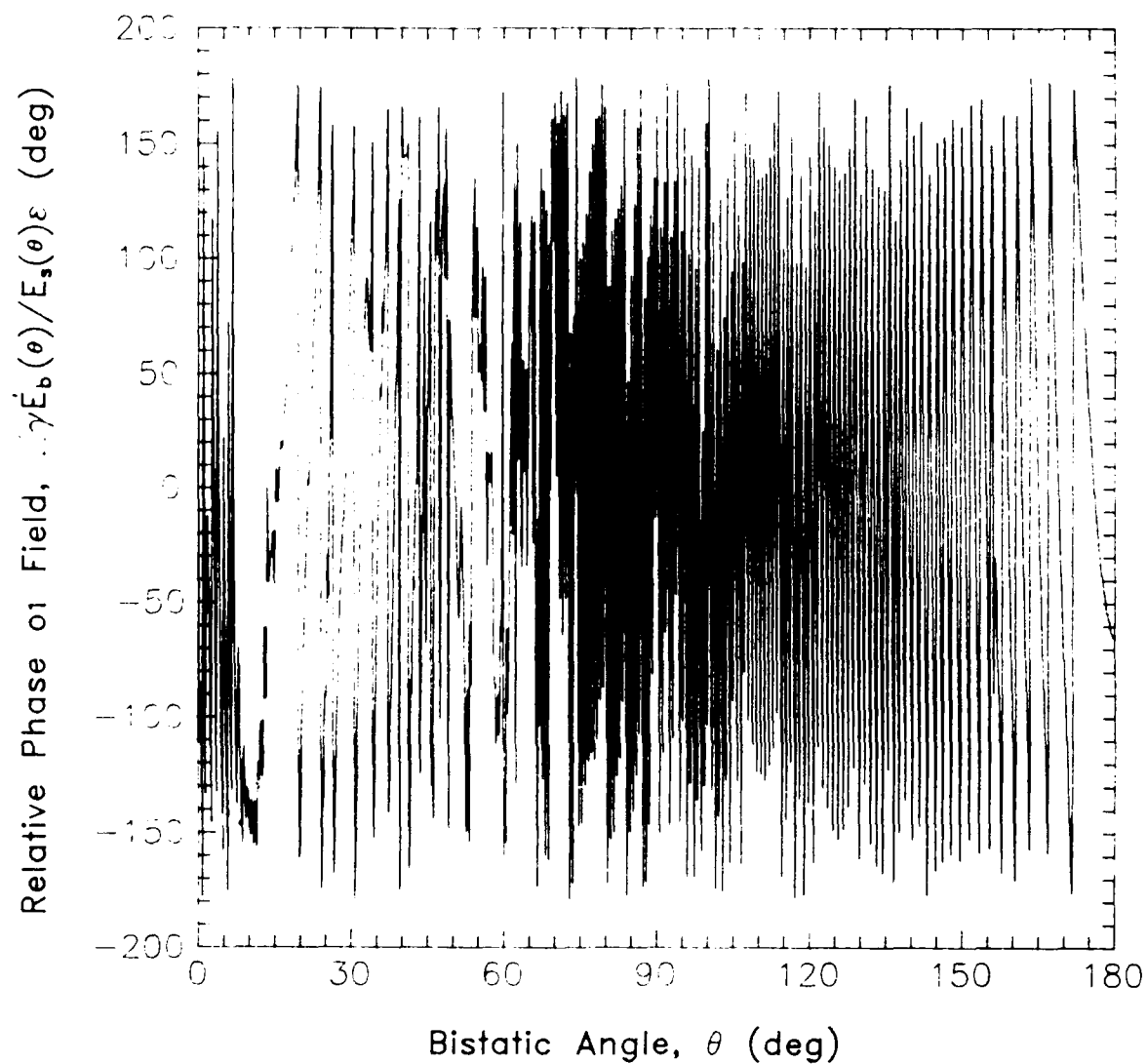


Figure 8(b). Phase Difference Between the Measured Background Field and the True Scattered Field of an Aluminum Cube (Side Length = 1.5λ) for broadside plane-wave incidence.

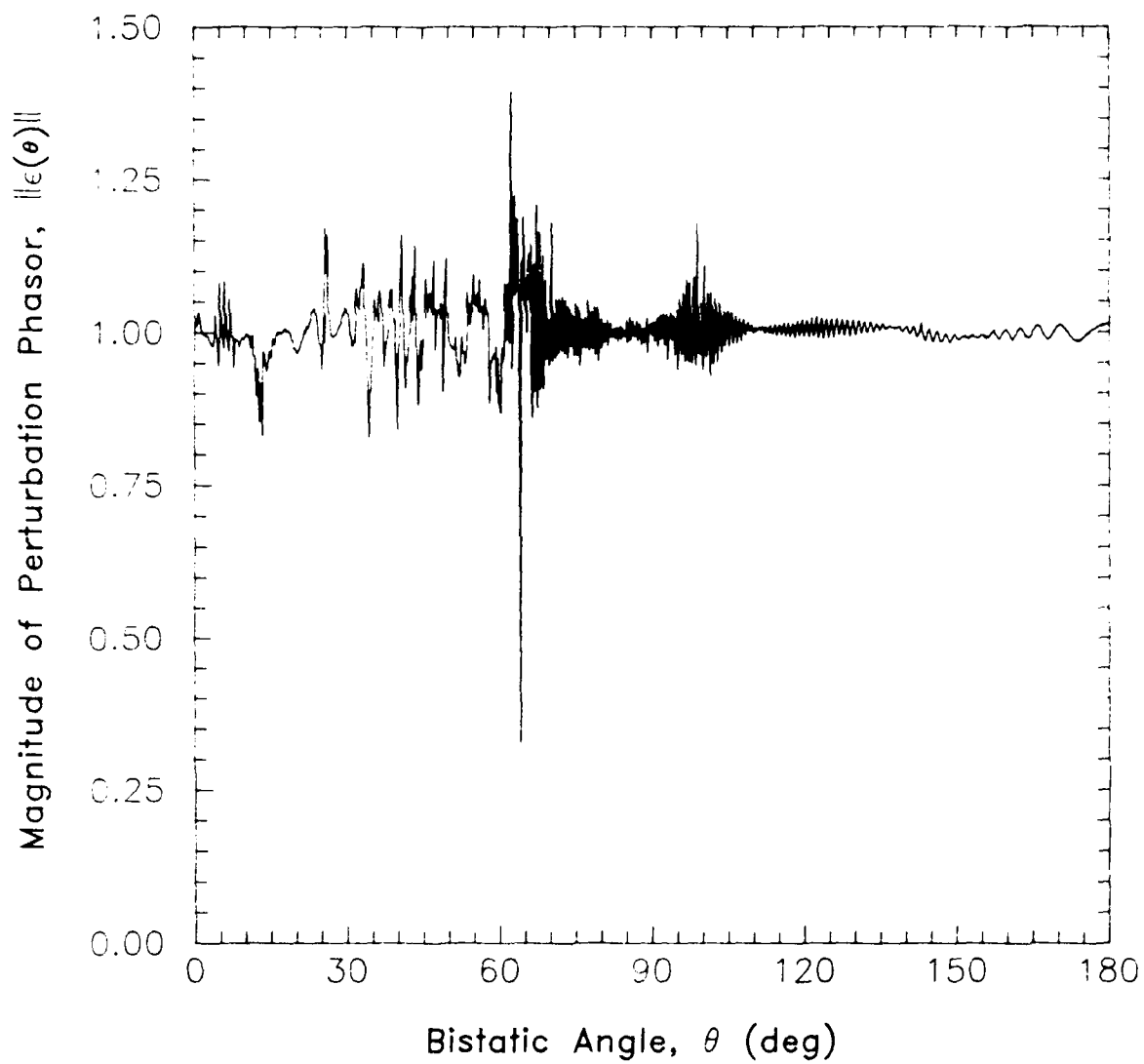


Figure 9(a). Magnitude of the Perturbation Phasor Computed from Two Distinct Background Measurements, $E'_{b1}(\theta)$ and $E'_{b2}(\theta)$.

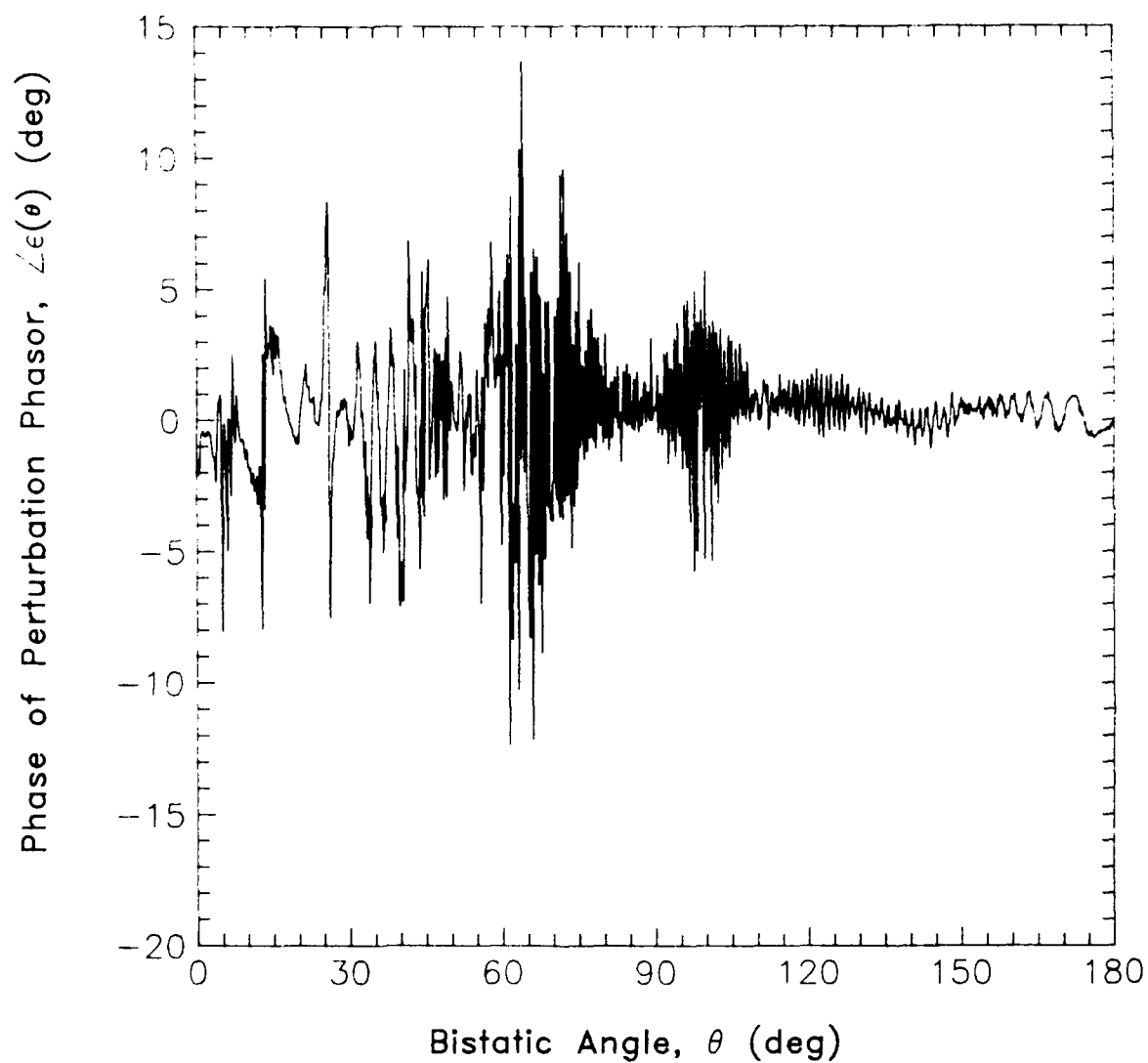


Figure 9(b). Phase of the Perturbation Phasor Computed from Two Distinct Background Measurements. This Gives the Phase Error Introduced in the Measured Scattered Field when Background Subtraction is Performed.

respectively. In this region we measure amplitude change from scan to scan of about 25 percent ($|\epsilon(\theta \approx 60^\circ)| = 1 \pm 0.25$) and a phase difference of about 10 degrees. The additional 3.5 degree phase error can be attributed to the positioning system. The reader will notice that in the forward scattering region the amplitude and phase of $\epsilon(\theta)$ exhibits a frequency modulated behavior that is nearly identical to the behavior of the measured scattered field [we stress that $\epsilon(\theta)$ is derived from measurements not linked to the total field measurements with the target present] which supports the assumption that the dominant error in the measured scattered field is due to imperfect background measurements rather than multiple interactions or variations in the true target scattered field. The target scattered field measurement error resulting from combining the two data sets, E'_b/E_s and $\epsilon(\theta)$, according to Eq. (7) is shown in Figure 10(a). The error curve has the same shape envelope as the amplitude of the background-to-scattered field ratio (Figure 8a). Figure 10(b) shows the amplitude of the error computed directly (that is, subtract the measured scattered field from the true scattered field and divide the result by the true scattered field). Comparing the predicted measurement error [error due to receiver and positioning errors shown in Figure 10(a)] with the actual measurement error [error computed directly, shown

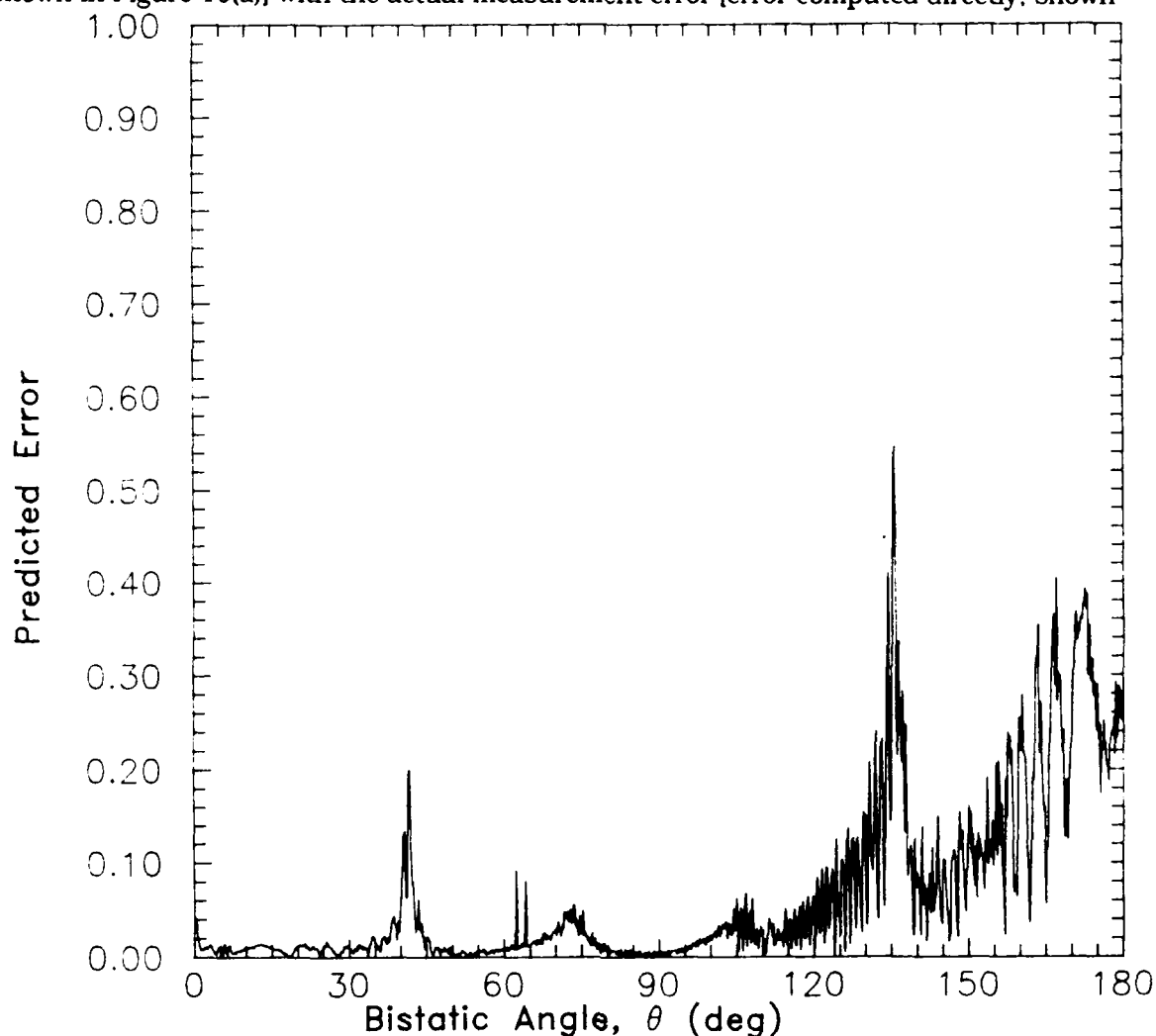


Figure 10(a). Predicted Error in the Measured E-Plane Scattered Field of an Aluminum Cube with Side Length 1.5λ .

in Figure 10(b)] shows that the true error is generally higher than the predicted error but that the gross variations in the forward scattering regions of both curves are similar. The actual error is larger than predicted near the midrange peaks, a result that is not consistent with receiver and positioning system errors. This means that either there are other unaccounted contributors to the error in the measured scattered field or that inaccuracies in the high frequency diffraction solution used for the true scattered-field solution are dominating the actual error. Our second example indicates the latter.

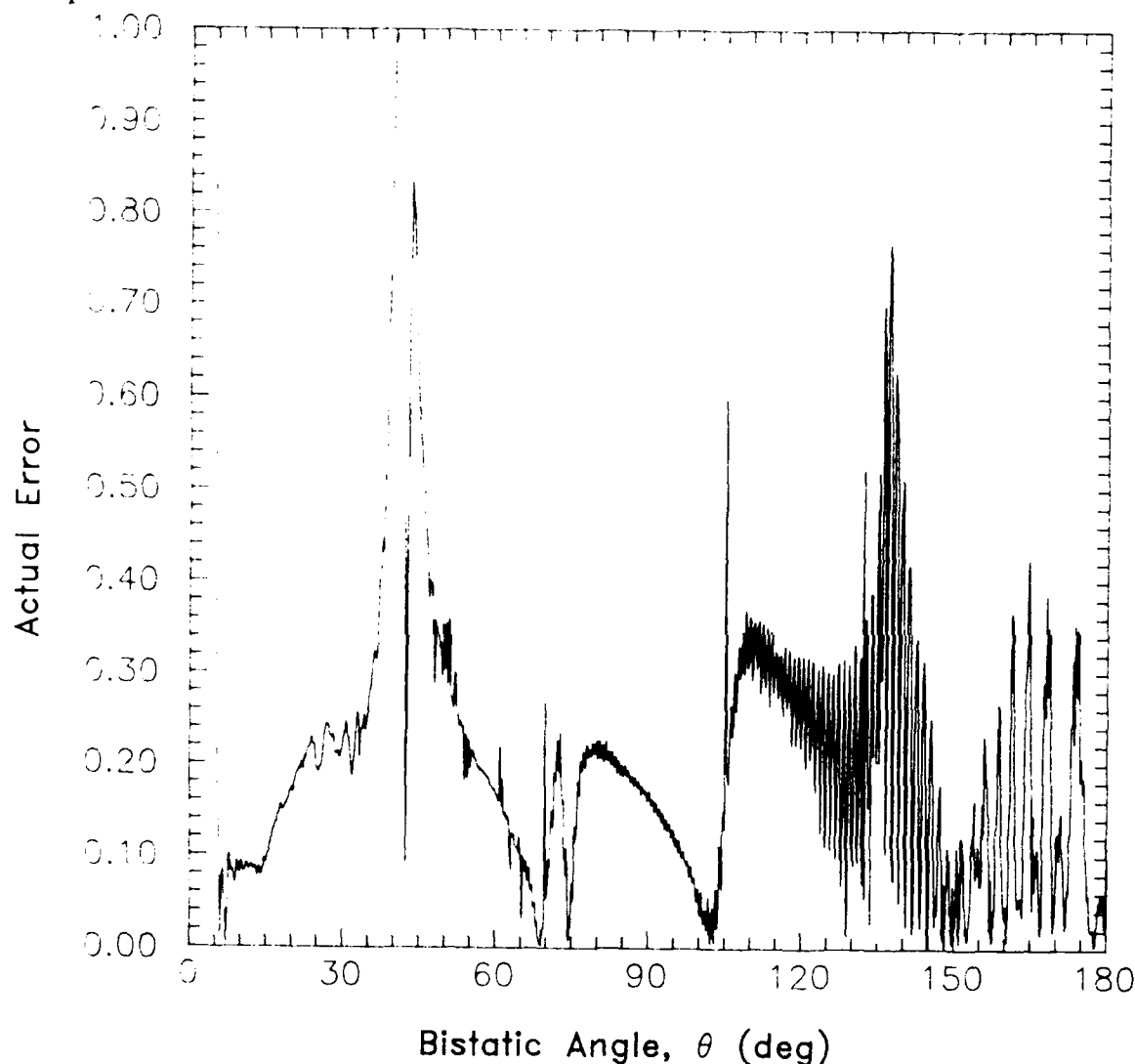


Figure 10(b). Actual Error in the Measured E-Plane Scattered Field of an Aluminum Cube with Side Length 1.5λ .

We include a second example, that of scattering from an aluminum sphere (18λ in circumference), which has an exact solution for the scattered field, to determine the reason for

the discrepancy that arose in the cube example. Figures 11(a) and 11(b) show the predicted and actual errors in the measured scattered field respectively. Figures 12(a) and 12(b) are the amplitude and phase curves for the true scattered field of the sphere as computed using the Mie series solution.³ Figures 13(a) and 13(b) are the measured scattered field, amplitude and phase. There is much better agreement between the two error curves (Figure 11) for the sphere example than for the cube. This suggests that for the sphere, the major contributors to the error in the measured scattered field are indeed the receiver and positioning system, and that the discrepancy between the predicted and actual errors for the cube are caused by inaccuracies in the high-frequency diffraction solution we used for the scattered field of the cube. Both examples show that the error varies more rapidly than the scattered field with respect to bistatic angle.

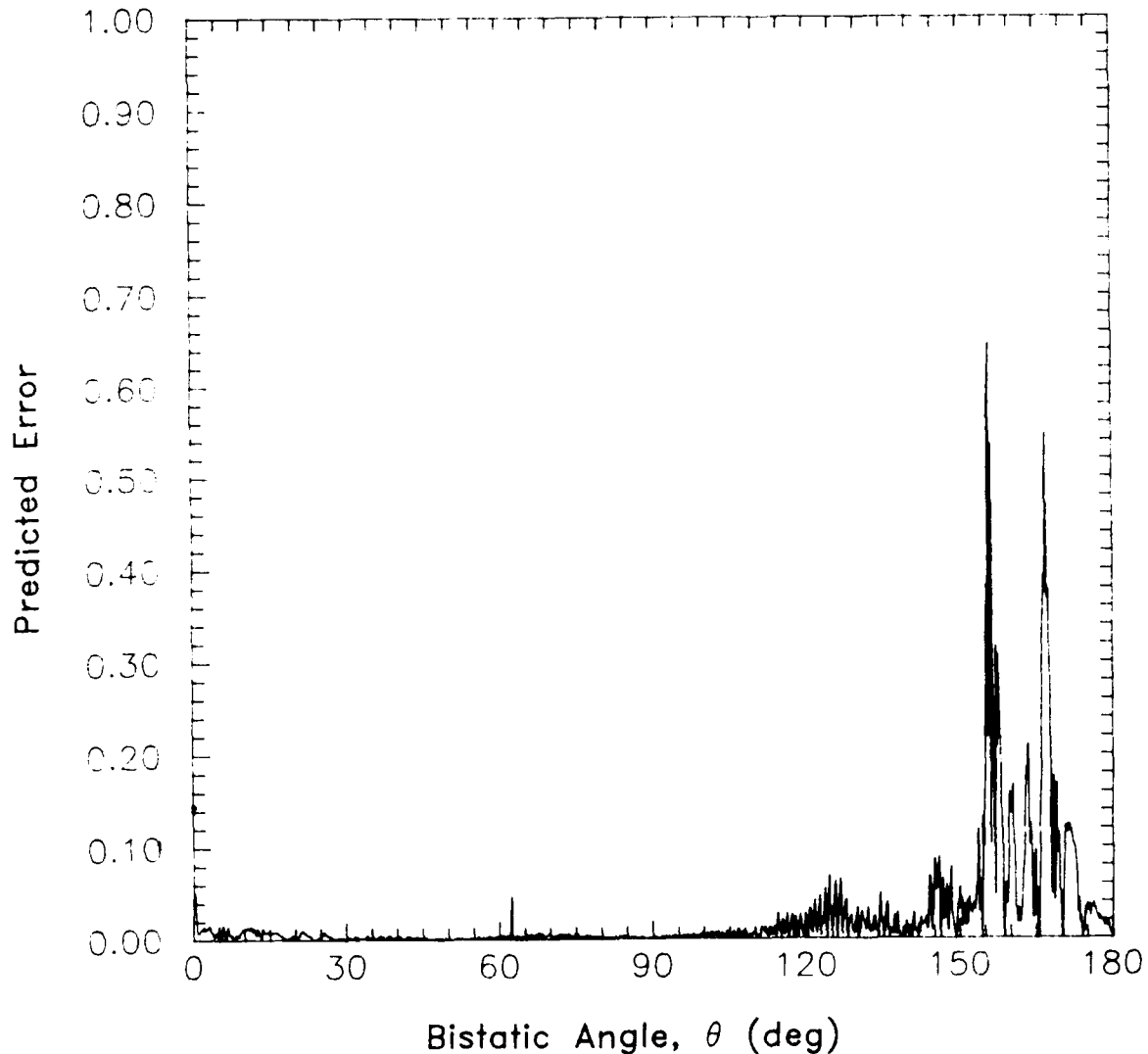


Figure 11 (a). Predicted Error in the Measured E-Plane Scattered Field of an Aluminum Sphere 18λ in Circumference.

³DiBeneditto, J. P. (1984), *Bistatic Scattering From Conducting Calibration Spheres*, RADC-TR-84-93. ADA154173

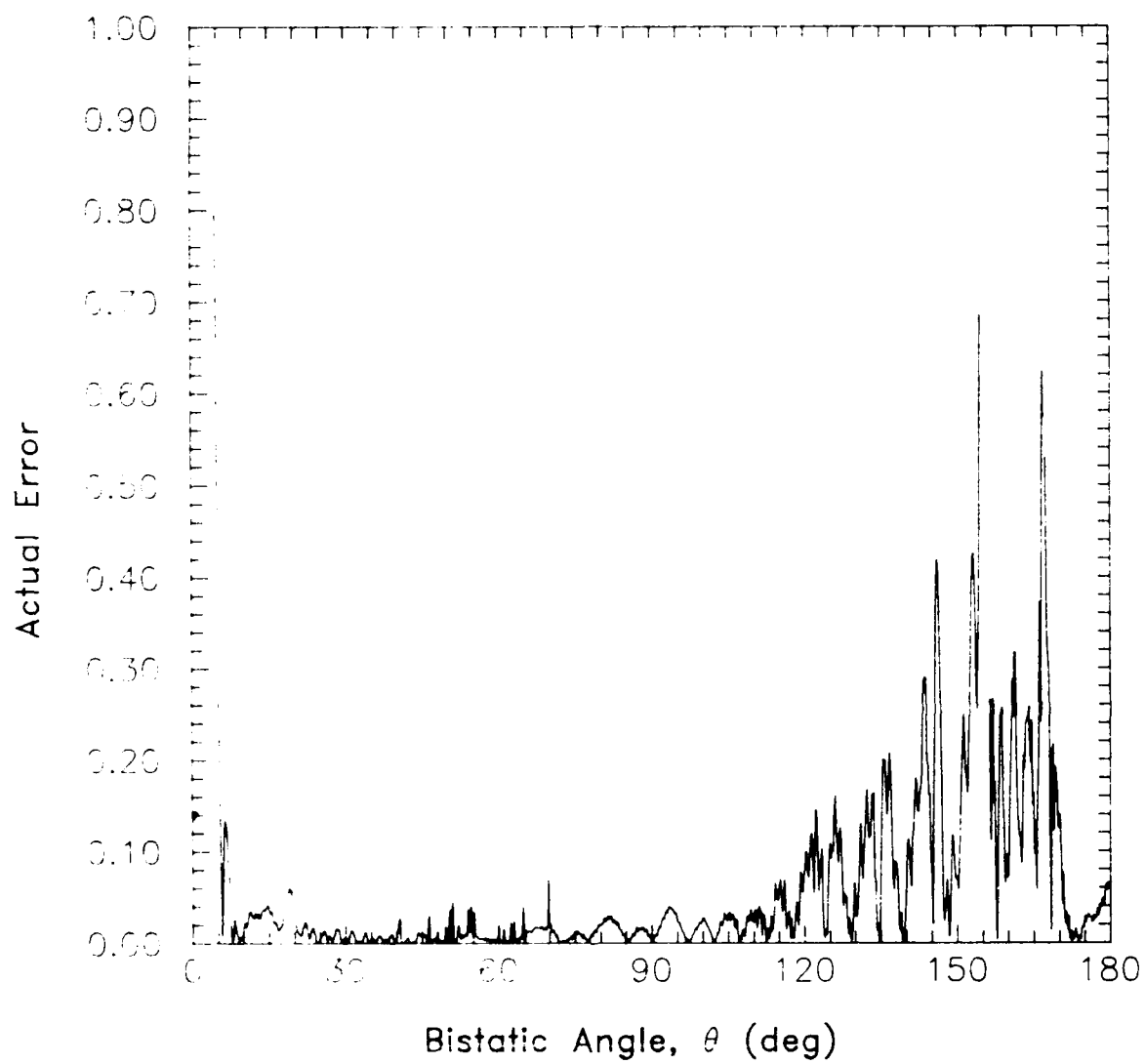


Figure 11(b). Actual Error in the Measured E-Plane Scattered Field of an Aluminum Sphere 18λ in Circumference.

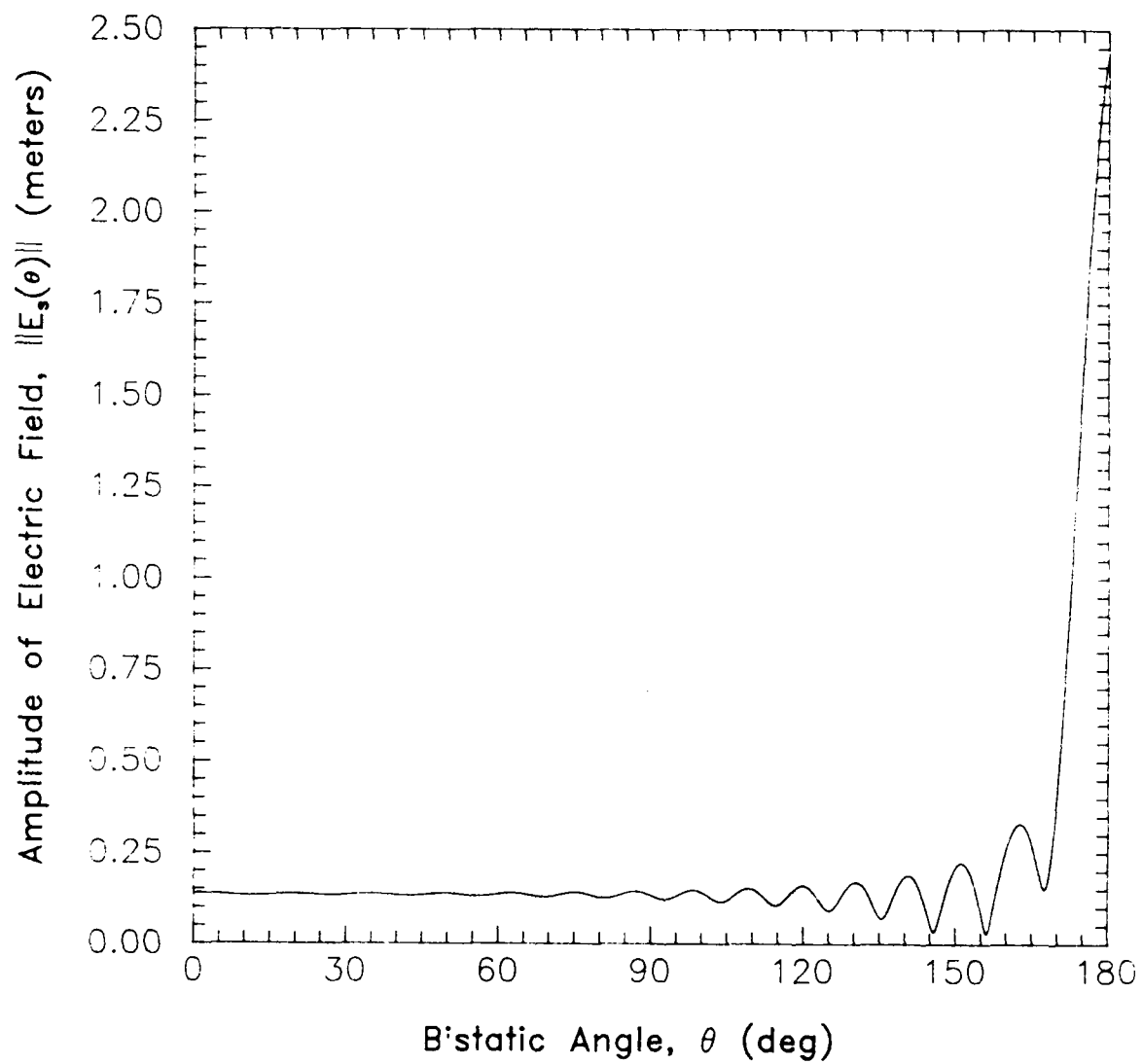


Figure 12(a). True E-Plane Scattered Field of a Perfectly Conducting (PEC) Sphere 18λ in Circumference Computed Using the Mie Series Solution.

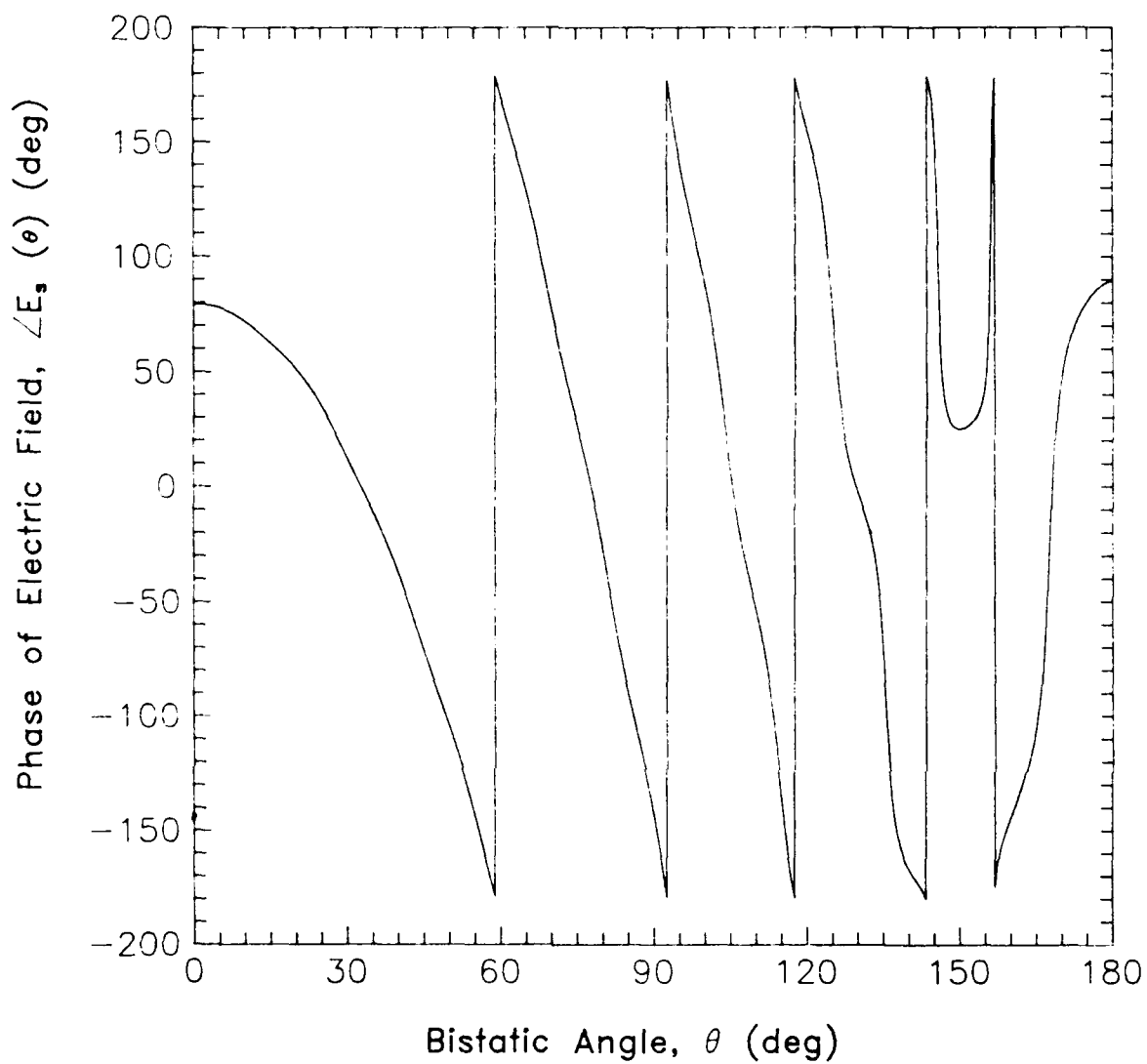


Figure 12(b). True E-Plane Scattered Field of a PEC Sphere with 18λ Circumference.

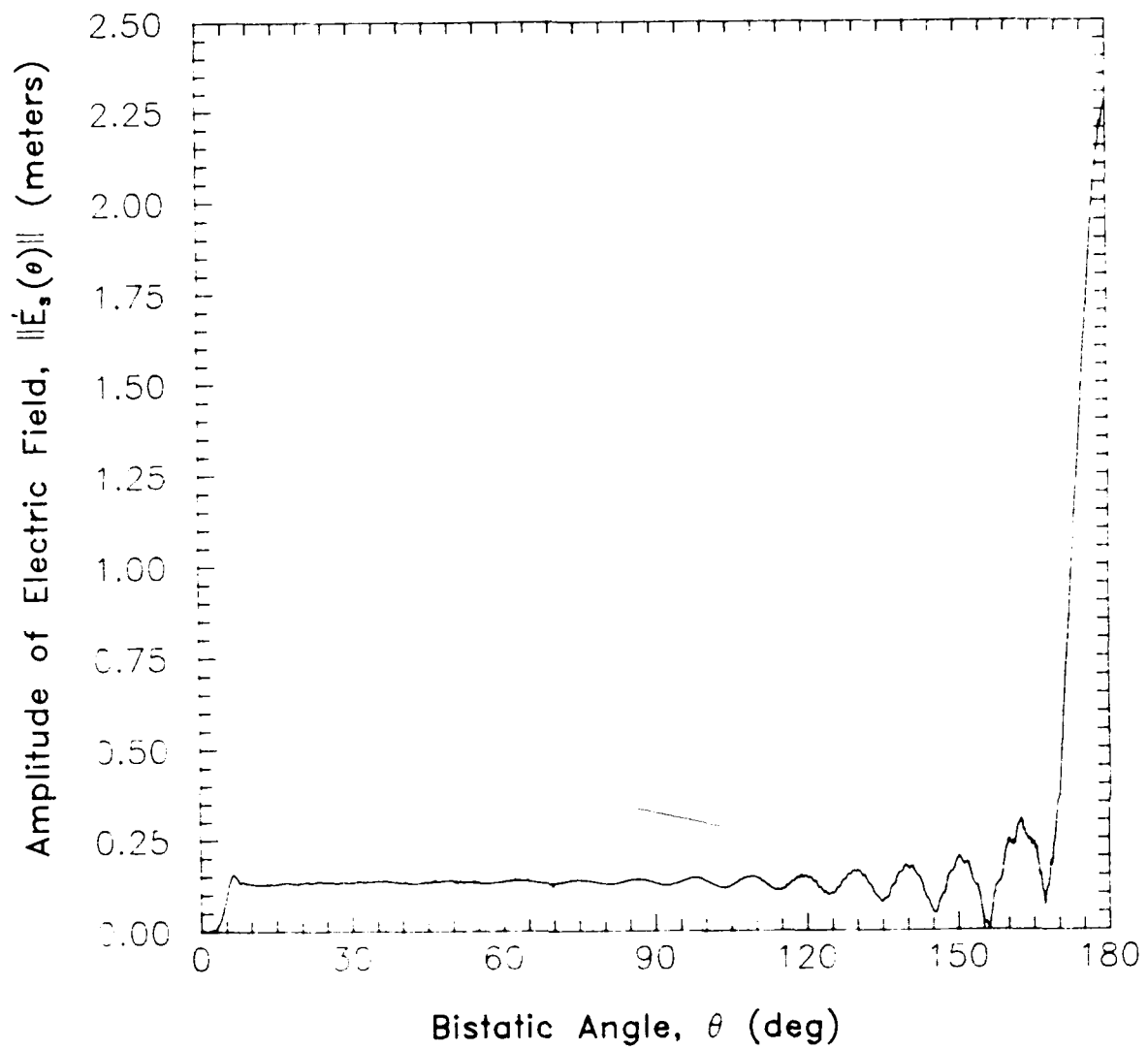


Figure 13(a). Amplitude of the Measured E-Plane Scattered Field of an Aluminum Sphere with 18λ Circumference.

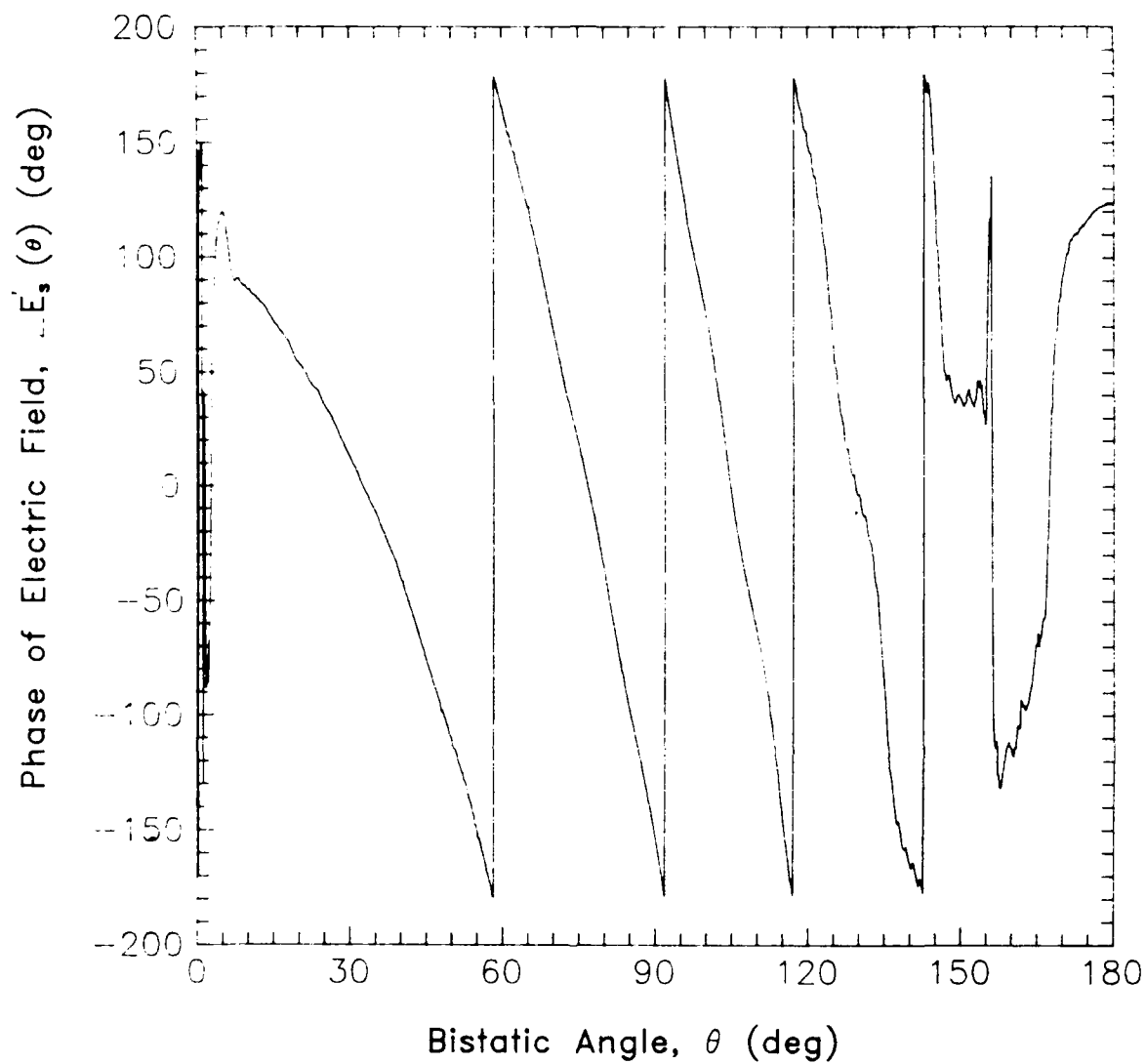


Figure 13(b). Phase of the Measured E-Plane Scattered Field of an Aluminum Sphere with 18λ Circumference.

4. SPATIAL FILTERING

In Section 3 we observed that much of the error in the measured scattered field takes the form of a high frequency rippling riding on top of the true scattered field. Because the data forms a function of observation angle that is Fourier transformable, one might consider removing the error by low-pass filtering the data. Without a truncation criterion, this idea is flawed because for general targets one cannot be sure which frequency components are attributable to the target and which are error. We require a truncation criterion that will insure that the entire spectral content of the target-scattered-field is recovered after filtering. Such a truncation criterion was developed first by L.J. Chu¹ and later confirmed by Collin and Rothchild.⁴ Chu found that for ordinary antennas (current distribution) totally contained within a spherical surface of radius "a," the quality factor Q_n of any given spherical mode increases astronomically when the mode number n becomes larger than the wavenumber-radius product ka . This means that outside of the reactive region the electric field produced by an antenna contains spherical modes of order ka or less. This physical band limit has defined the sampling criteria for calculating far field antenna patterns from cylindrical and spherical near-field measurements.⁵ A general rule used by people in the near-field antenna pattern measurement community is that accurate antenna far field patterns are computed if the near field is sampled sufficiently to recover spatial frequencies of $1.1k(a + \lambda)$.

Specifically, the general solution to the wave equation in spherical coordinates⁶ for the true scattered field of the target reduces to

$$E_s(\theta) = \sum_{m=-1.1k(a+\lambda)}^{1.1k(a+\lambda)} B_m e^{im\theta} \quad (8)$$

in the plane of measurement of our RADAR/EECT RCS range, where B_m are the Fourier modal coefficients. We see that in the measurement plane the spherical modes of the scattered field are just sines and cosines and the field solution is a band limited Fourier series with $B_m = 0$ for $|m| > 1.1k(a + \lambda)$. We return to the examples of the cube and sphere of Section 3 to investigate the practical aspects of the filtering scheme.

The measured scattered field can also be expanded formally into a Fourier series:

$$E'_s(\theta) = \sum_{m=-\infty}^{\infty} B_m e^{im\theta}, \quad (9)$$

where B'_m is not necessarily band limited by $|m| = 1.1k(a + \lambda)$ because $E'_s(\theta)$ includes measurement errors.

⁴Collin, R. E. and Rothchild, S. (1963), Evaluation of Antenna Q *IEEE Transactions on Antennas and Propagation*, **AP-12**:23-27, January 1964.

⁵Yaghjian A.D. (1986), "An Overview of Near-Field Antenna Measurements," *IEEE Transactions on Antennas and Propagation*, Vol. AP-34, No. 1, 30-45, January.

⁶Stratton, J. A., (1941), *Electromagnetic Theory*, McGraw-Hill, pp. 392-420.

Because the expansion functions are orthogonal, the expansion modal coefficients B'_m can be computed from the measurements by the integral

$$B'_m = \frac{1}{2} \pi \int_0^{2\pi} E'_s e^{-im\theta} d\theta. \quad (10)$$

The filtered measured scattered field $E''_s(\theta)$ is now computed by summing the contributing Fourier expansion coefficients according to the bandwidth of Eq. (8) that is

$$E''_s(\theta) = \sum_{m=-1.1k(a+\lambda)}^{+1.1k(a+\lambda)} B'_m e^{+im\theta}. \quad (11)$$

To insure the best accuracy this technique requires that the scattered field be sampled over the entire 2π radians at the Nyquist rate (or higher) of the measured scattered field, $E'_s(\theta)$. The Nyquist rate is greater than that of the true scattered field, $E_s(\theta)$, which requires only $2.2k(a+\lambda)$ samples/radian. The sampling interval in the example at hand was 0.0035 radian which gives a sufficiently high sampling rate of 286.5 samples per radian. (This sampling rate corresponds to the highest sampling rate that the RADC/EECT system can comfortably achieve, and was used here so that we could recover the spectrum of all sources of the measured total field, and thus measured scattered field as accurately as possible). Figures 14(a) and 14(b) show the spatial amplitude spectrum of the measured scattered field of the cube and the true scattered field as determined by the high-frequency diffraction solution. We notice that the measured scattered field spectrum has a considerably broader bandwidth than the true scattered field, whose spectrum dies rapidly for harmonics larger than $1.1k(a+\lambda)$ (15 in this case). We can see that the measured scattered field spectral content outside of the $1.1k(a+\lambda)$ bandwidth is in error (that is, not part of the true target scattered field). Summing the measured scattered field spectrum according to Eq. (11) produces the filtered measured cube scattered field, which is graphed in Figures 15(a) (amplitude) and 15(b) (phase) (compare to the unfiltered plots in Figures 6(a) and 6(b)). A plot of the actual error in the filtered measured scattered field is given in Figure 16. Comparing this curve with the actual error in the measured scattered field of the cube before filtering [Figure 10(b)] shows that filtering smooths the error curve and reduces the error in the forward scattering region significantly.

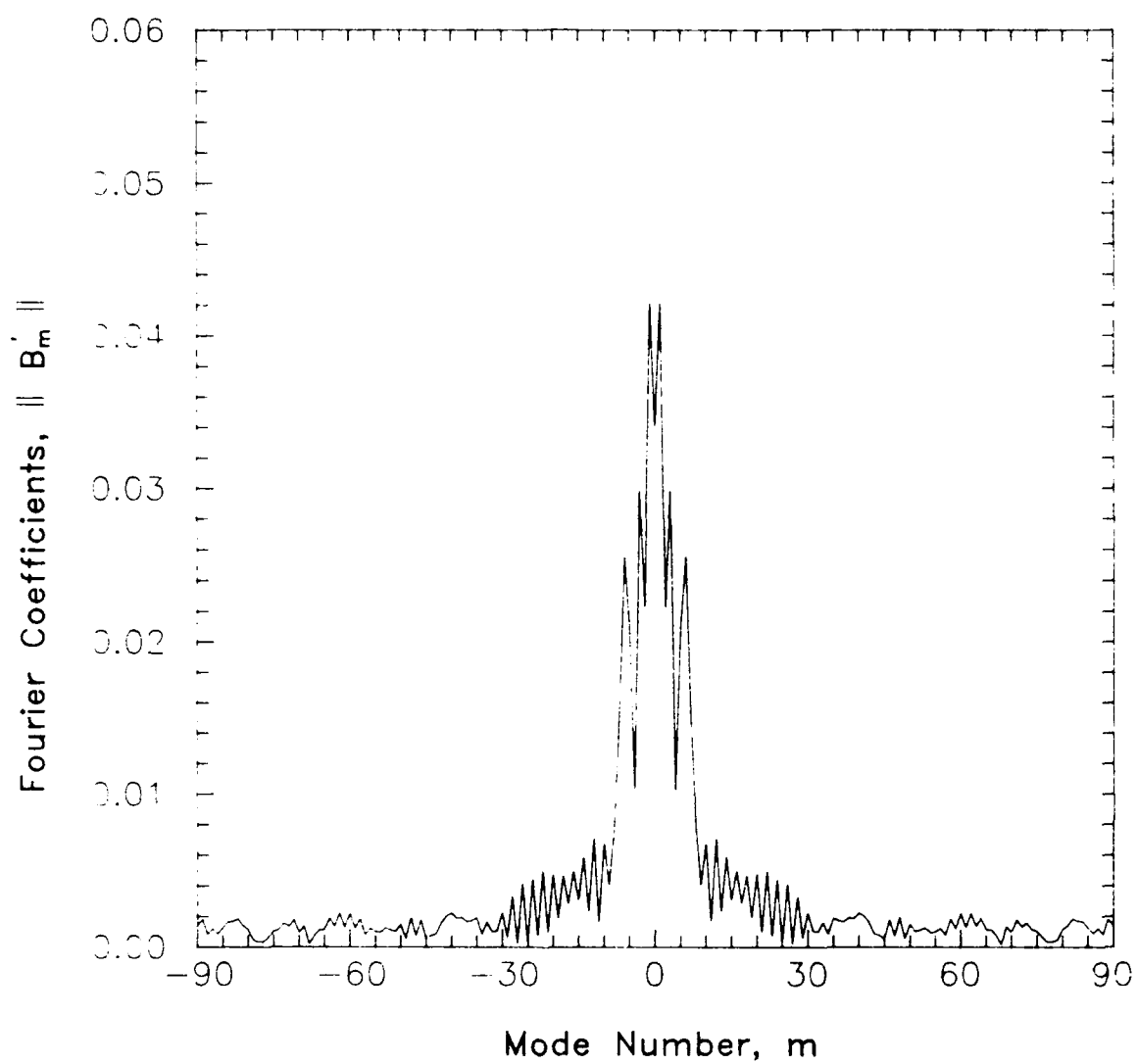


Figure 14(a). Spatial Spectrum of the Measured E-Plane Scattered Field of an Aluminum Cube with Side Length 1.5λ .

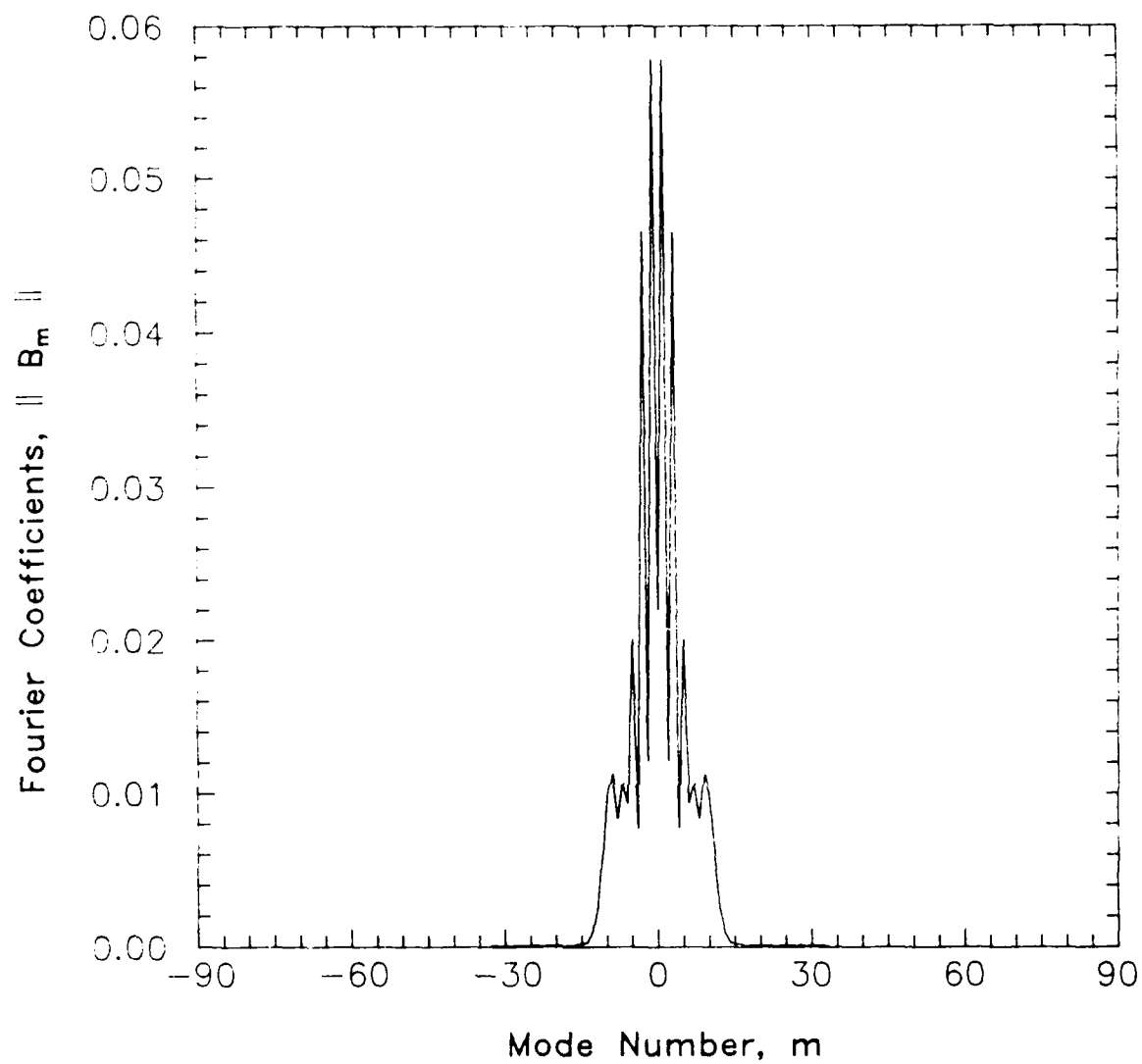


Figure 14(b). Spatial Spectrum of True E-Plane Scattered Field of a PEC Cube with Side Length 1.5λ .

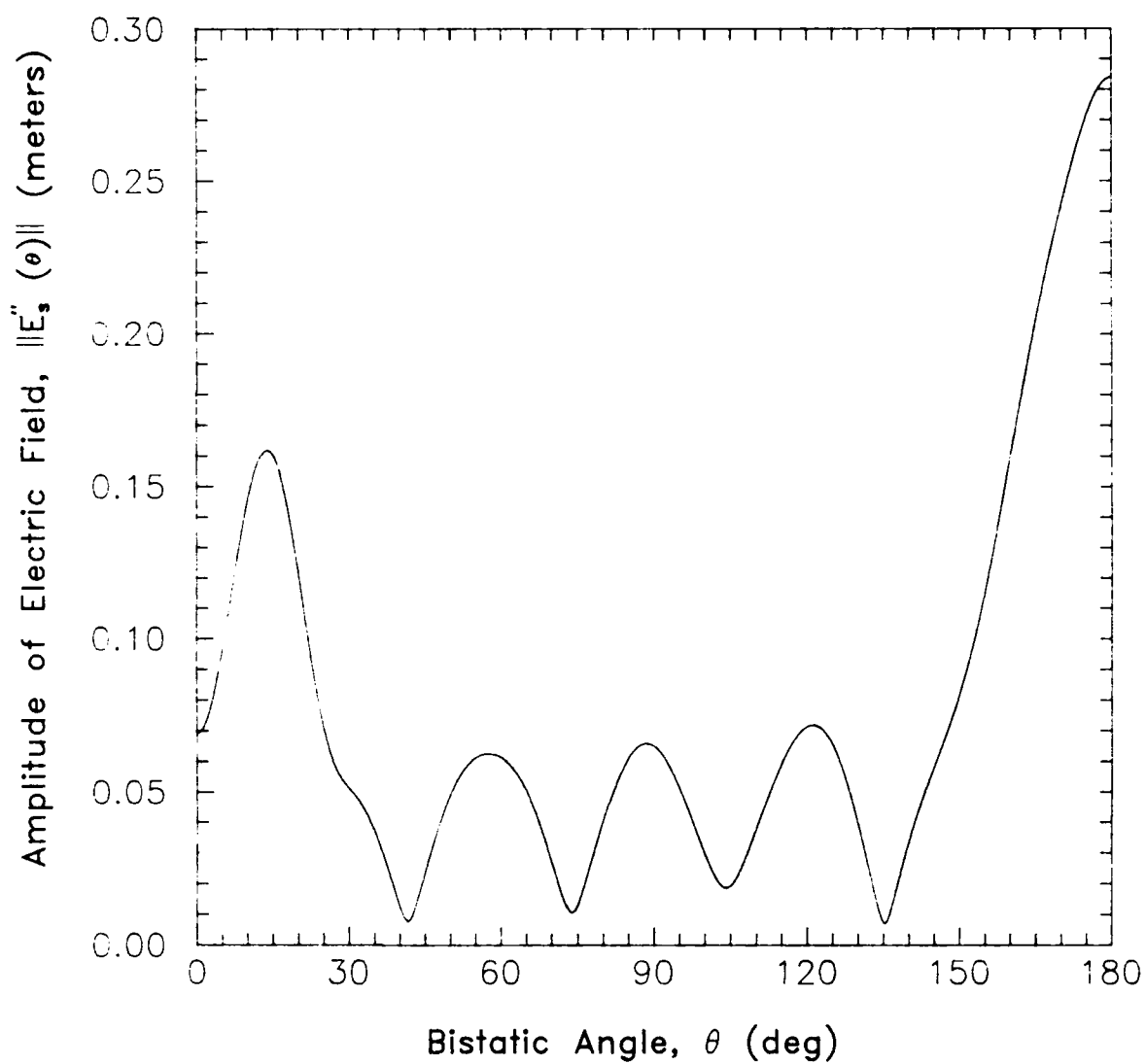


Figure 15(a). Amplitude of the Measured E-Plane Scattered Field of an Aluminum Cube with Side Length 1.5λ After Spatial Filtering.

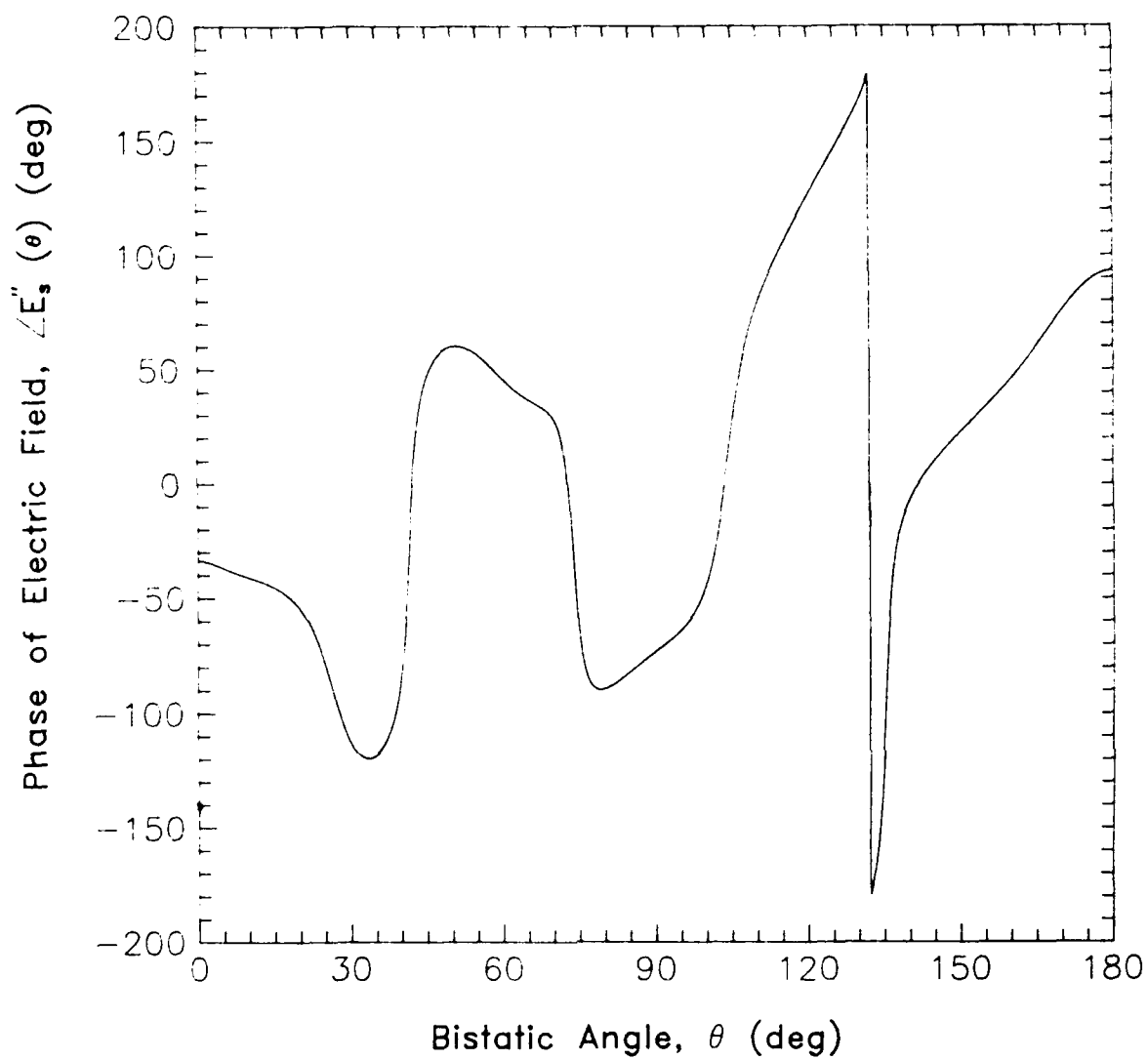


Figure 15(b). Phase of the Measured E-Plane Scattered Field of an Aluminum Cube with Side Length 1.5λ After Spatial Filtering.

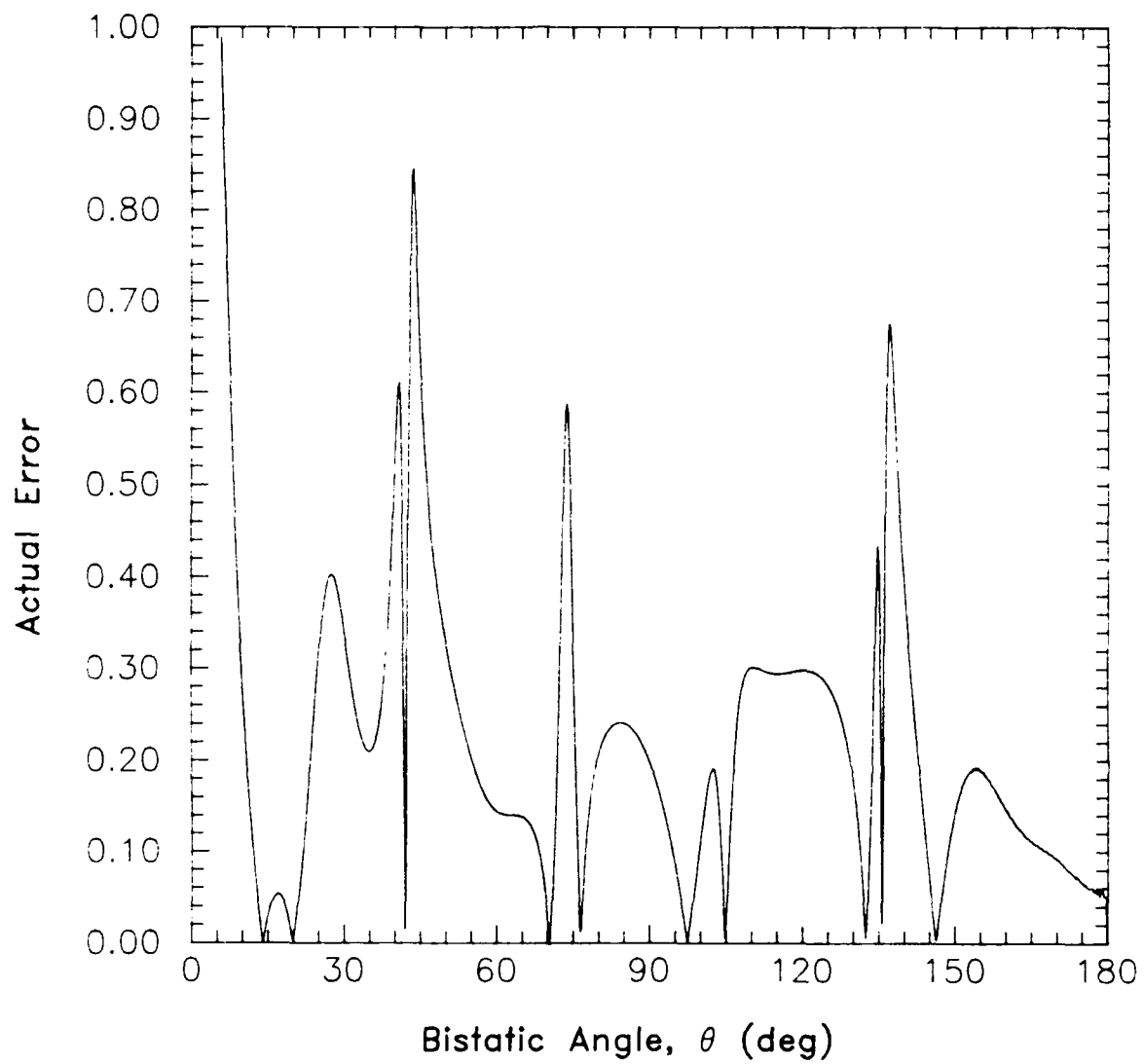


Figure 16. Actual Error in the Filtered Measured E-Plane Scattered Field of an Aluminum Cube with Side Length 1.5λ .

Figures 17(a) and 17(b) show the spatial spectra of the measured, and true scattered fields for the aluminum sphere. Figures 18(a) and 18(b) show the amplitude and phase of the measured scattered field of the sphere after filtering (24 modes used). The actual error in the filtered data is plotted in Figure 19. Comparing this curve with the error in the unfiltered measurements [Figure 11(b)] shows again that filtering smooths the curve and reduces the forward scattering errors.

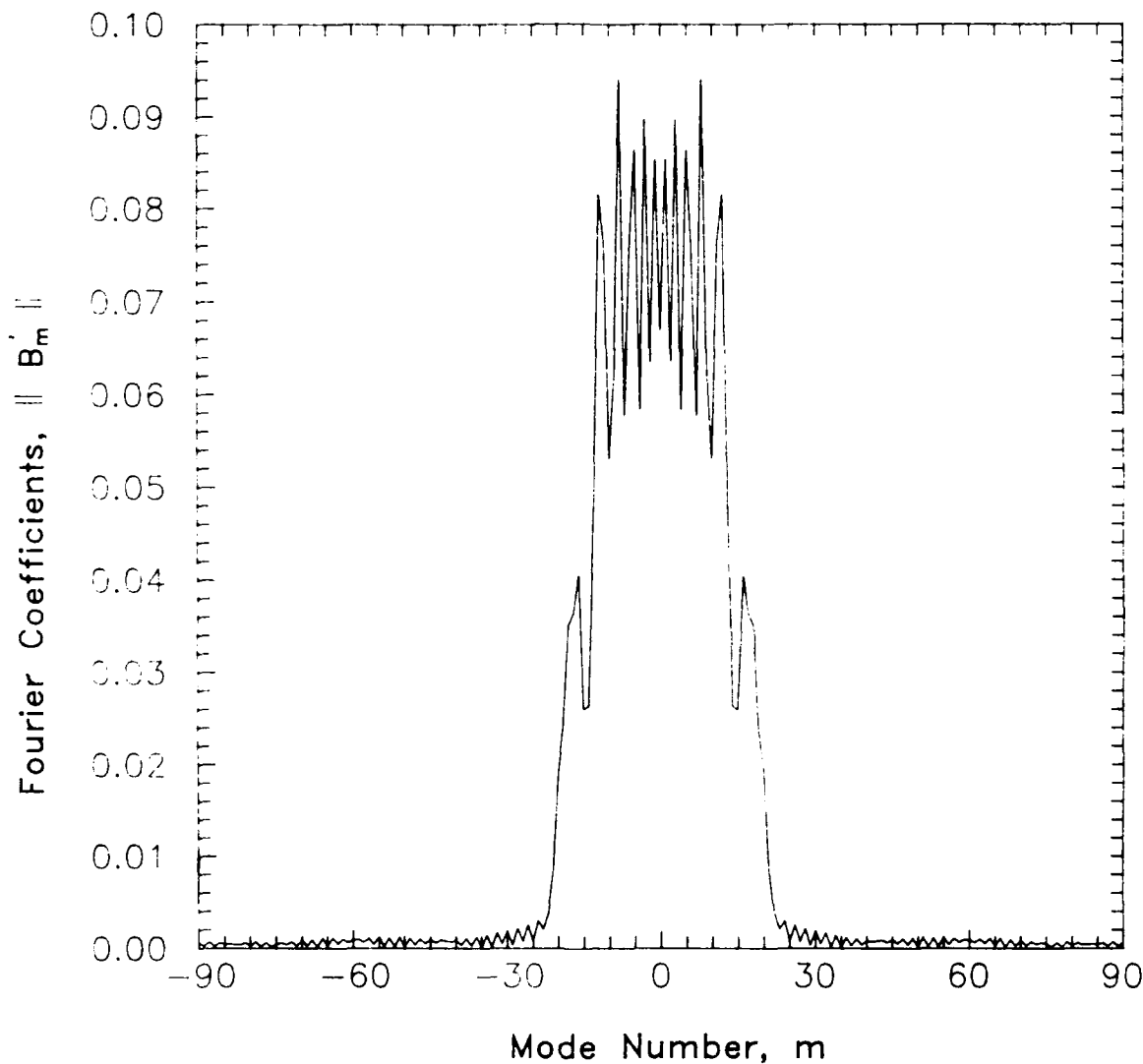


Figure 17(a). Spatial Spectrum of the Measured E-Plane Scattered Field of an Aluminum Sphere with 18λ Circumference.

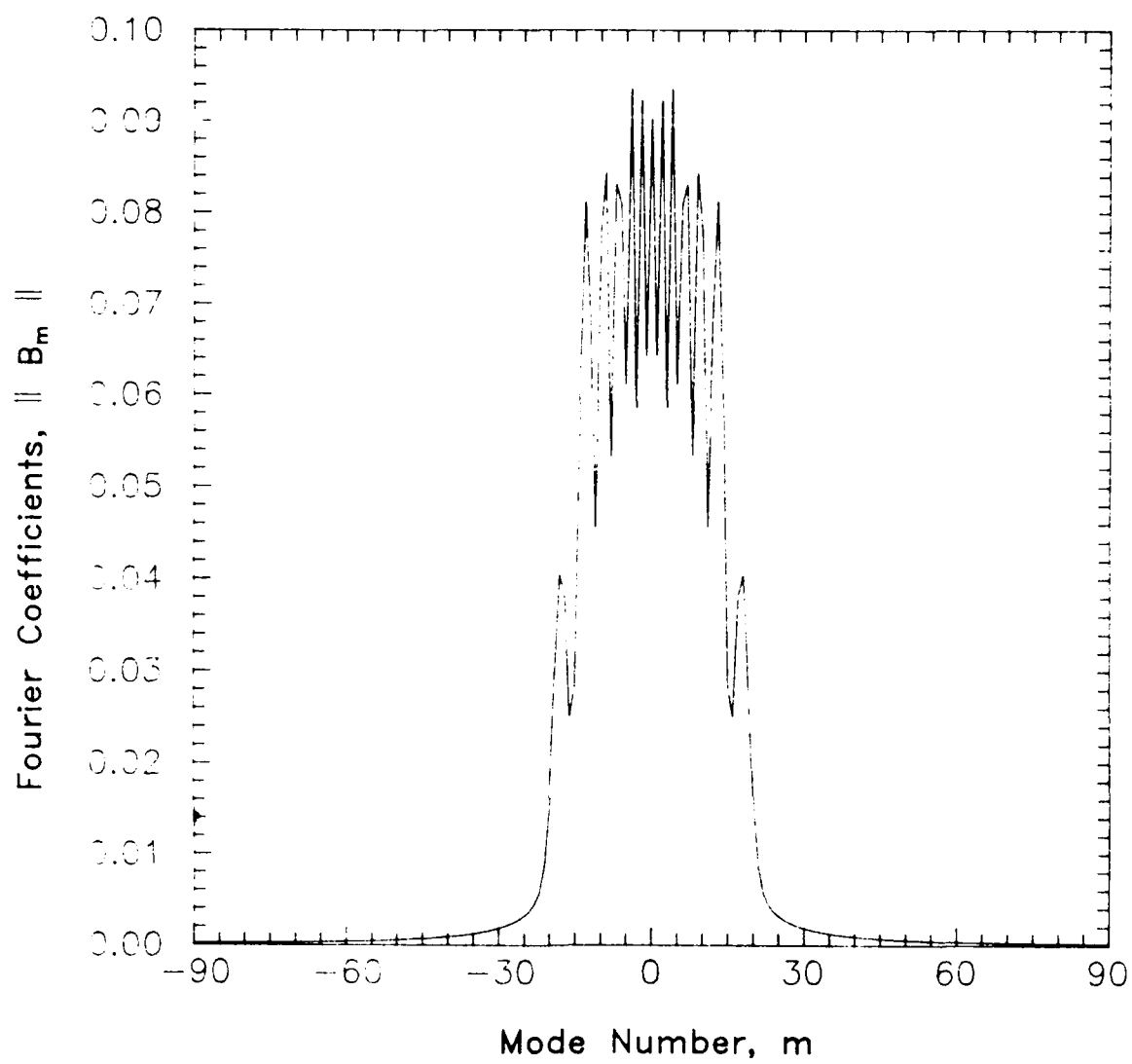


Figure 17(b). Spatial Spectrum of the True E-Plane Scattered Field of a PEC Sphere with 18λ Circumference.

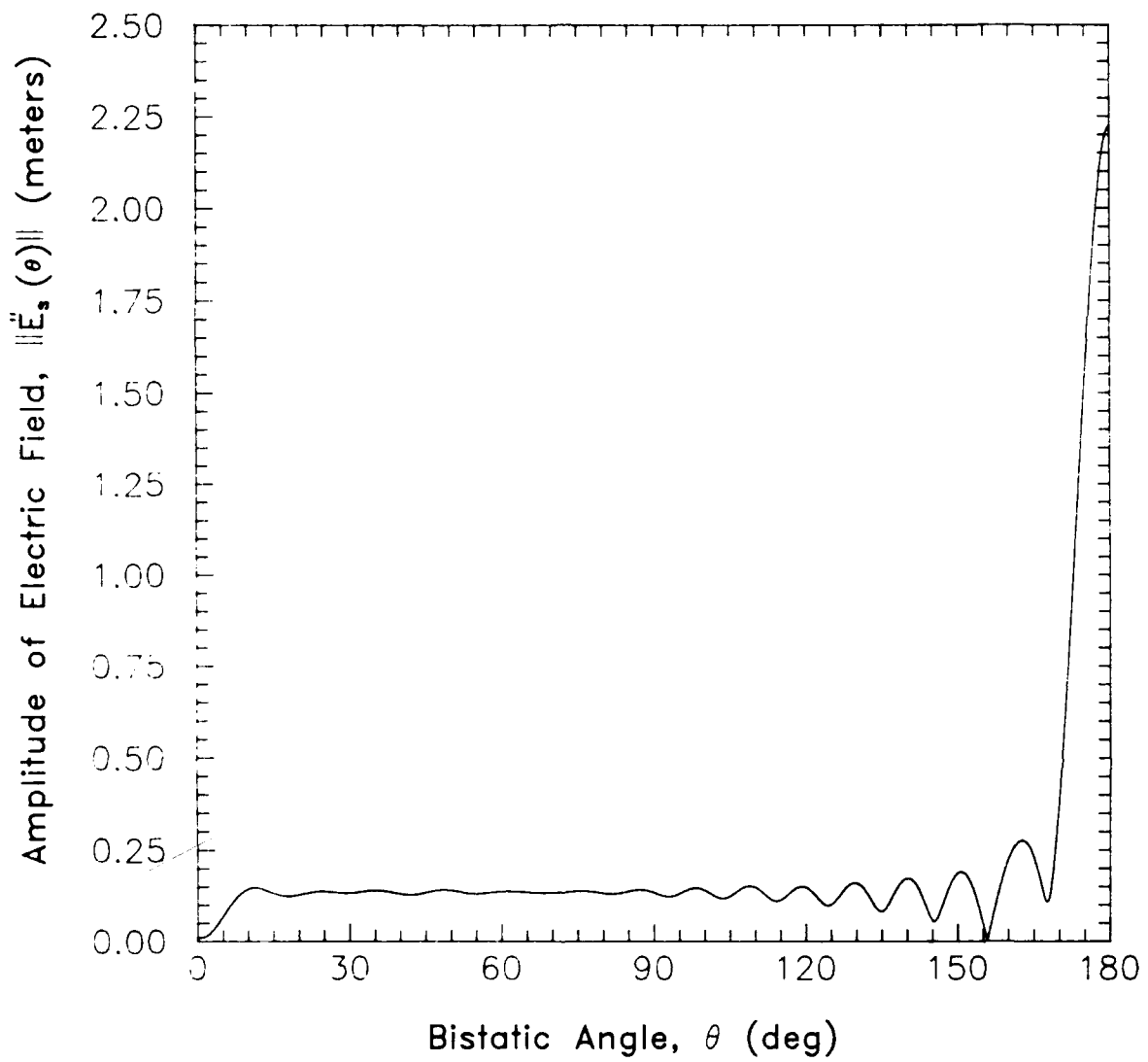


Figure 18(a). Amplitude of the Measured E-Plane Scattered Field of an Aluminum Sphere with 18λ Circumference After Spatial Filtering.

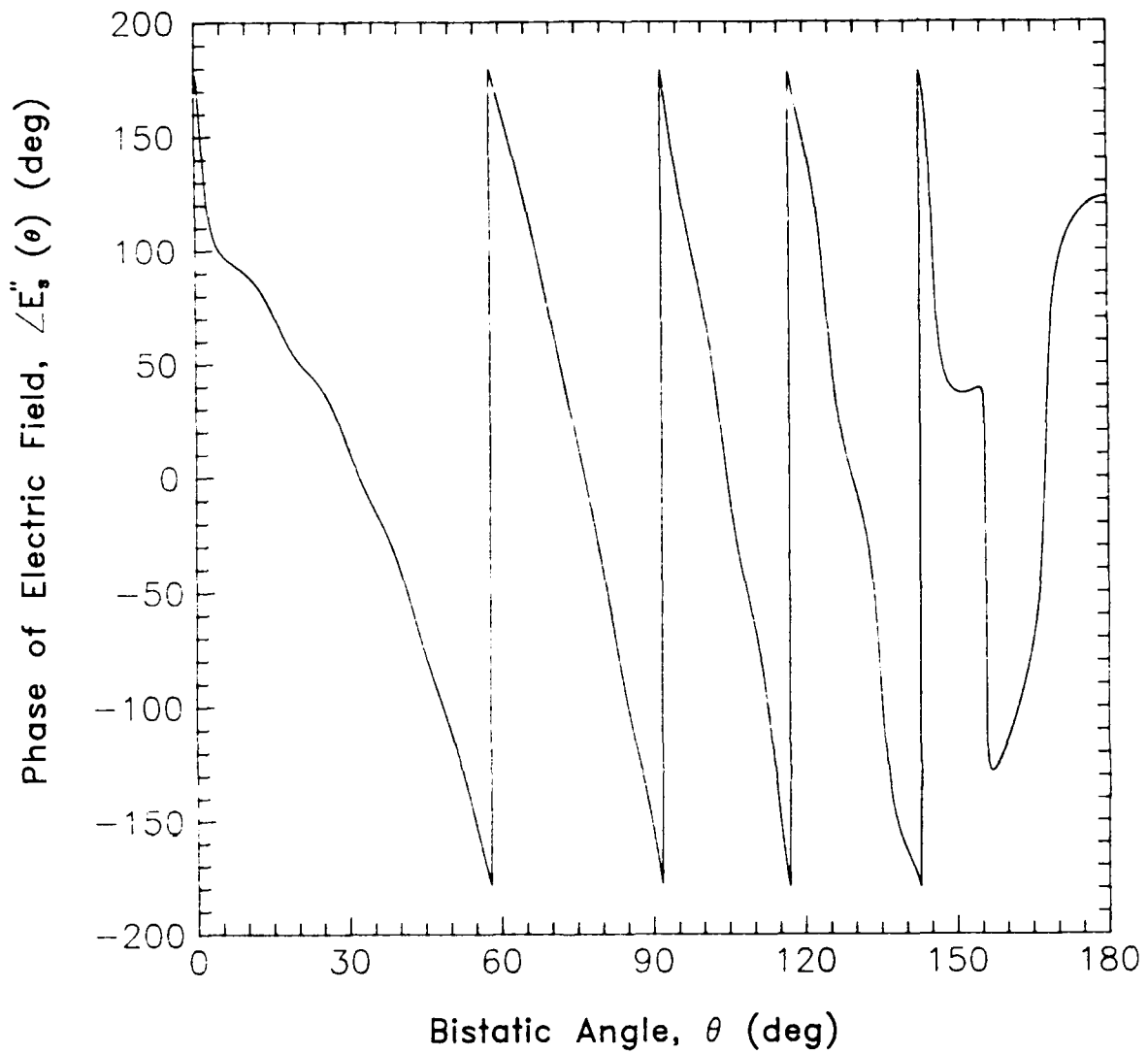


Figure 18(b). Phase of the Measured E-Plane Scattered Field of an Aluminum Sphere with 18λ Circumference After Spatial Filtering.

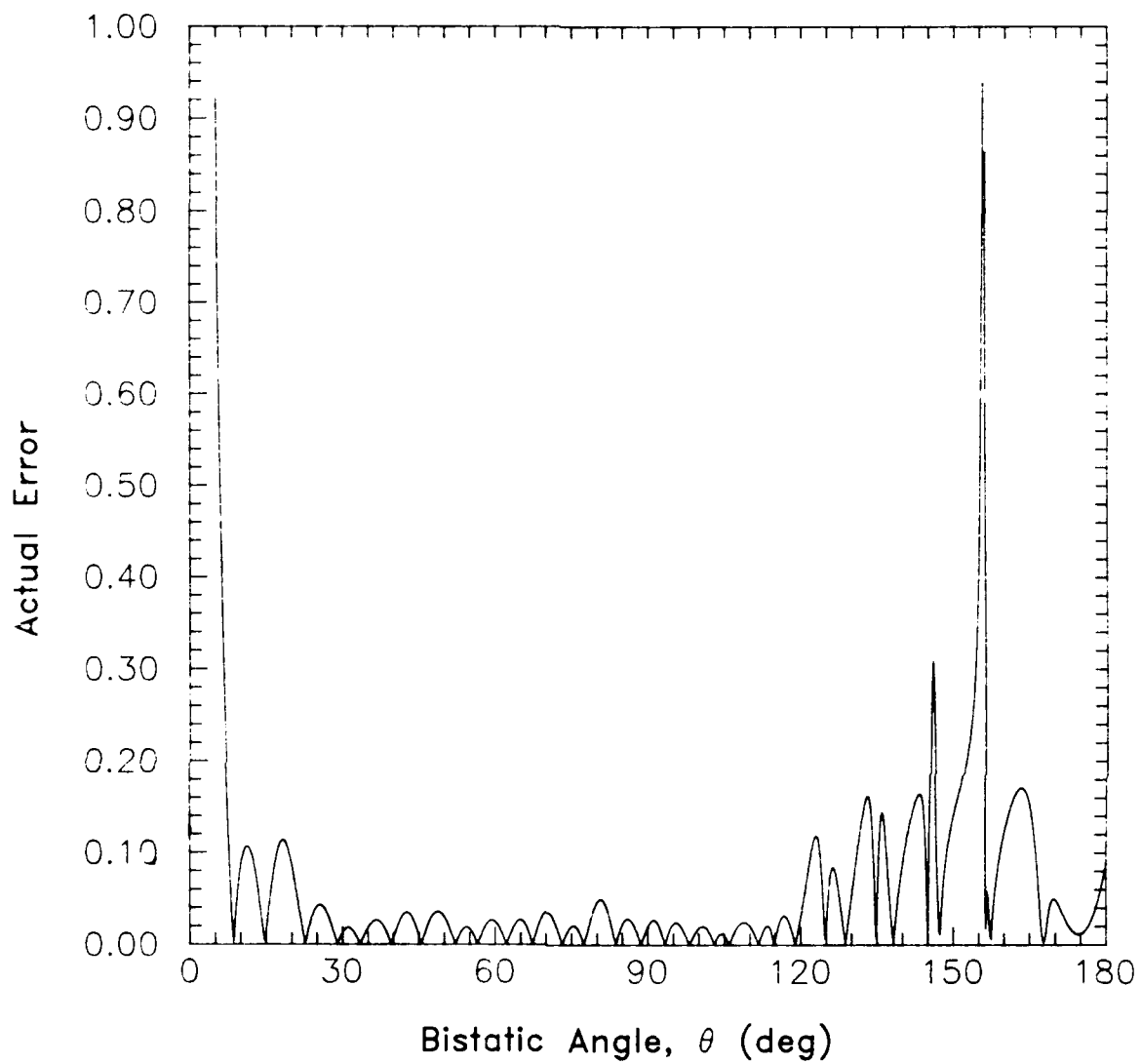


Figure 19. Actual Error in the Filtered Measured E-Plane Scattered Field of an Aluminum Sphere with 18λ Circumference.

5. EXAMPLES OF SPATIAL FILTERING APPLIED TO THE MEASUREMENT OF BISTATIC SCATTERING FROM METAL CUBES

In this section we present further examples that illustrate an application of spatial filtering. Specifically we present the measured unfiltered, measured filtered, and predicted E-plane and 45°-plane scattered fields from the perfectly conducting cubes of side lengths 1.5λ and 3λ , for broadside plane wave incidence. The measured scattered fields were obtained using the background subtraction technique described in Section 2. The E-plane data was collected by effectively[†] moving the receiving probe in the $\phi = 90^\circ$ plane and recording the θ component of the electric field. No other component will be excited so that this data gives the total scattered field after background subtraction. The 45°-plane data was collected in two measurement scans. First, the receiving probe was effectively moved in the $\phi = 45^\circ$ plane and the θ component of the electric field was recorded. Second, the receiving probe was again effectively moved in the $\phi = 45^\circ$ plane but this time the ϕ component of the electric field was recorded. The total scattered field is derived from the superposition of the two data sets after the backgrounds were subtracted.

In the previous sections we presented the E-plane unfiltered (Figure 6) and filtered (Figure 15) scattered fields of a 1.5λ cube for broadside incidence. In the unfiltered data we noted a dip in the backscattering region due to shadowing of the receiving antennas by the transmitting antenna. The filtered data was derived from the straightforward application of the filtering to the measured scattered field (refer to Section 2). We saw that the filtering reproduced (low frequency part) the shadow dip in the backscattering region of the scattered field amplitude [Figure 15(a)]. This shadow-dip error was confined to the backscattering region before filtering, but upon filtering this error becomes distributed throughout the scattered field through the low frequency components that make up the error. To minimize the effect of this known error on the rest of the scattered field, we artificially fit the first 5 degrees of the backscattering lobe in the unfiltered scattered field to the sinc function. We use the sinc function because we know from physical optics that a cube-scattered field varies as $\text{sinc}[(ks)\sin\theta]$ (s is the cube side length) near backscatter. The modified unfiltered E-plane RCS of the 1.5λ cube is shown in Figure 20(a). Figure 20(b) shows the E-plane RCS of the same cube after filtering. The reader will notice that the filtered data is much smoother than the unfiltered data, especially in the forward scattering region.

Figures 21(a) and 21(b) show the 45°-plane unfiltered RCS (modified in the backscattering region) and filtered RCS, respectively, for the 1.5λ cube. In this case the high frequency rippling in the forward scattering region makes the measured scattering pattern somewhat ambiguous. The high frequency rippling is erroneous but without filtering the best representation of the measured scattering pattern would be with the ripple peaks connected as an upper bound and the ripple troughs connected as a lower bound on the data in the forward scattering region. After filtering [Figure 21(b)], the measured scattering pattern is smooth and can be presented without ambiguity.

Figure 22 shows the measured filtered E-plane and 45°-plane RCSs as a function of observation angle θ plotted against two predictions of the RCS for the 1.5λ cube. The solid lines

[†]We write "effectively moving the receiving probe" because in the EECT system, the transmitting antenna and target are moved and the receiving antenna is fixed.

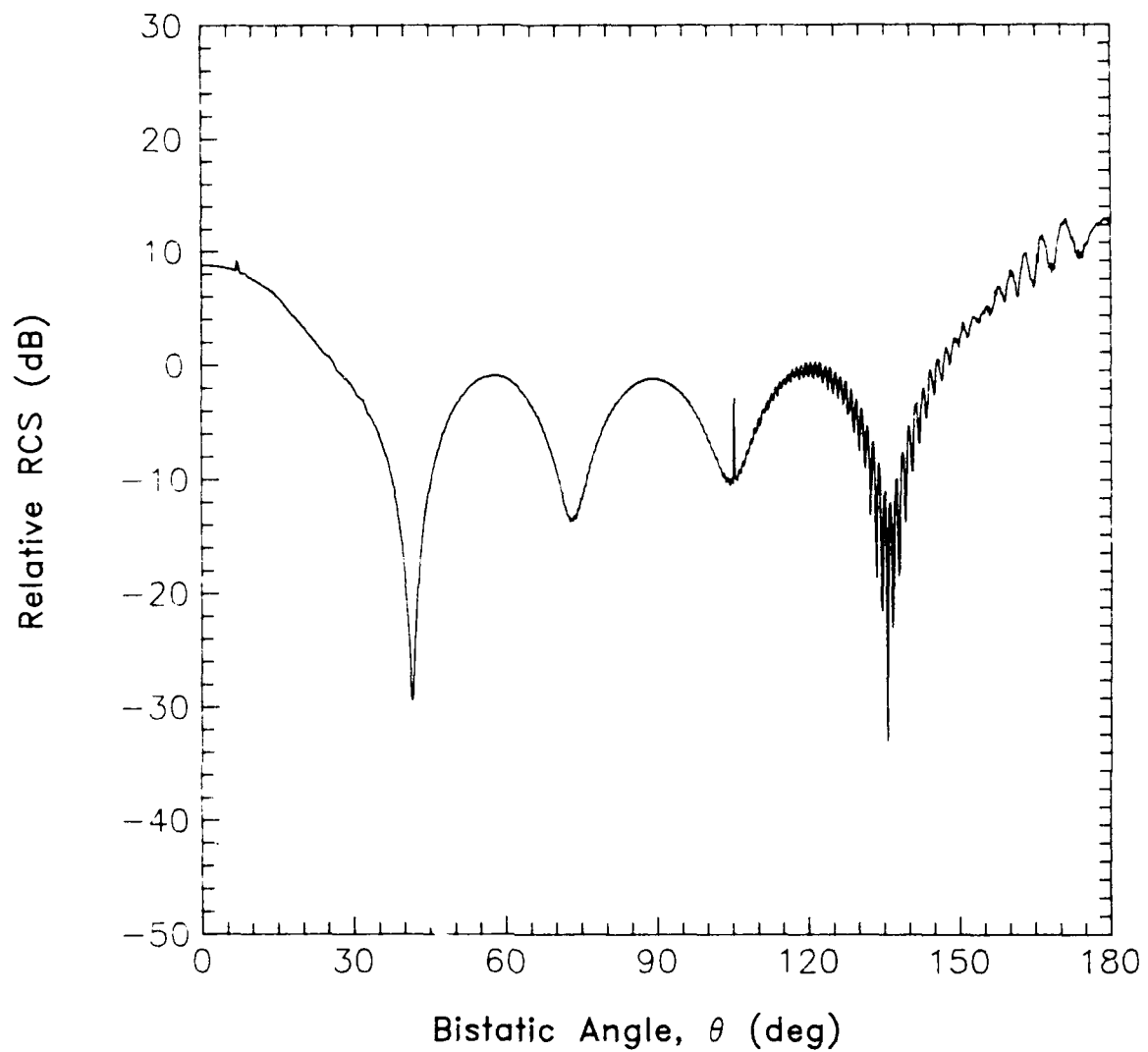


Figure 20(a). Measured E-Plane RCS of an Aluminum Cube with Side Length 1.5λ Before Spatial Filtering and with the Backscattering Lobe Artificially Fit to the $\sin(x)/x$ Function.

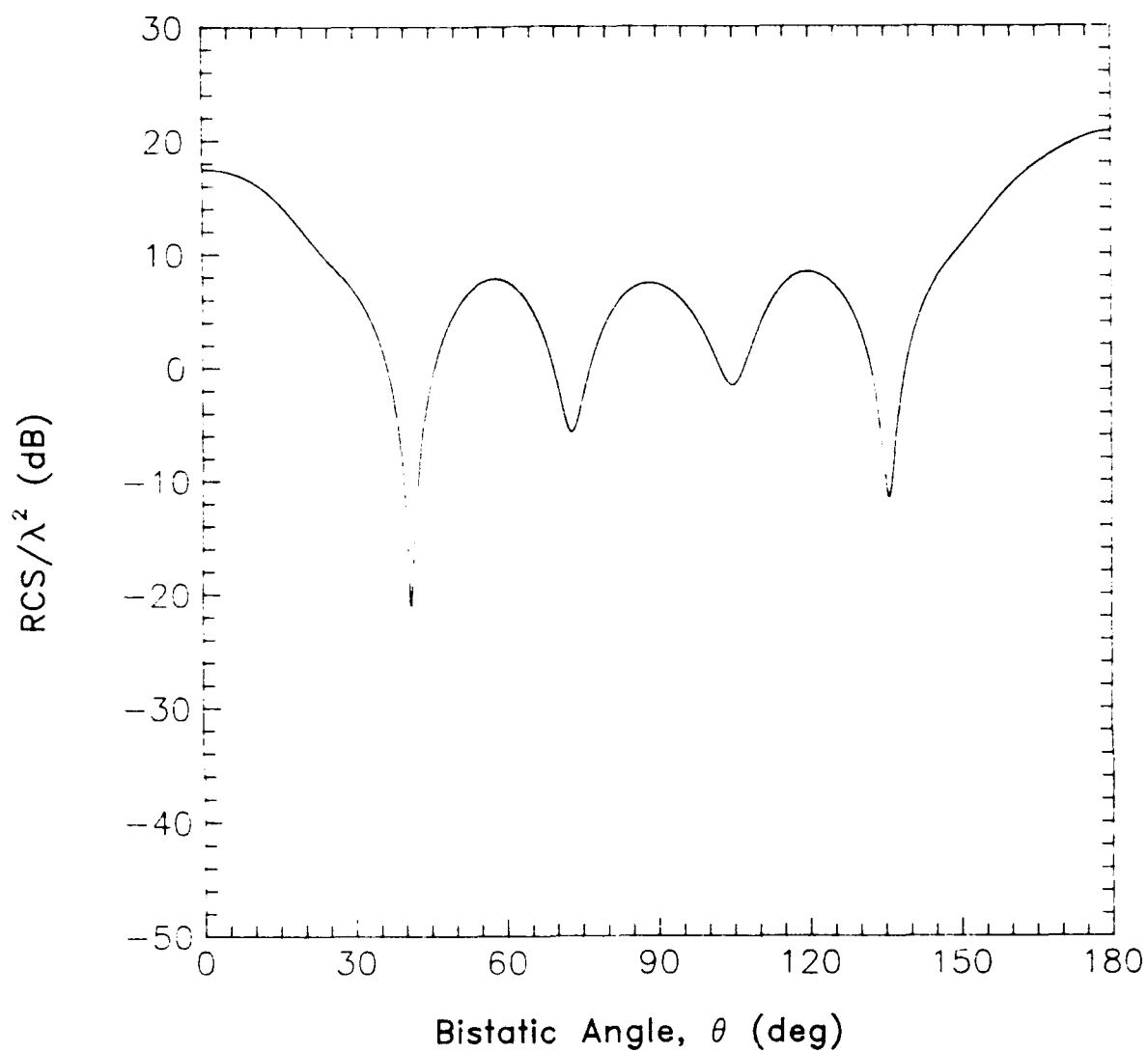


Figure 20(b). Measured E-Plane RCS of an Aluminum Cube with Side Length 1.5λ After Spatial Filtering.

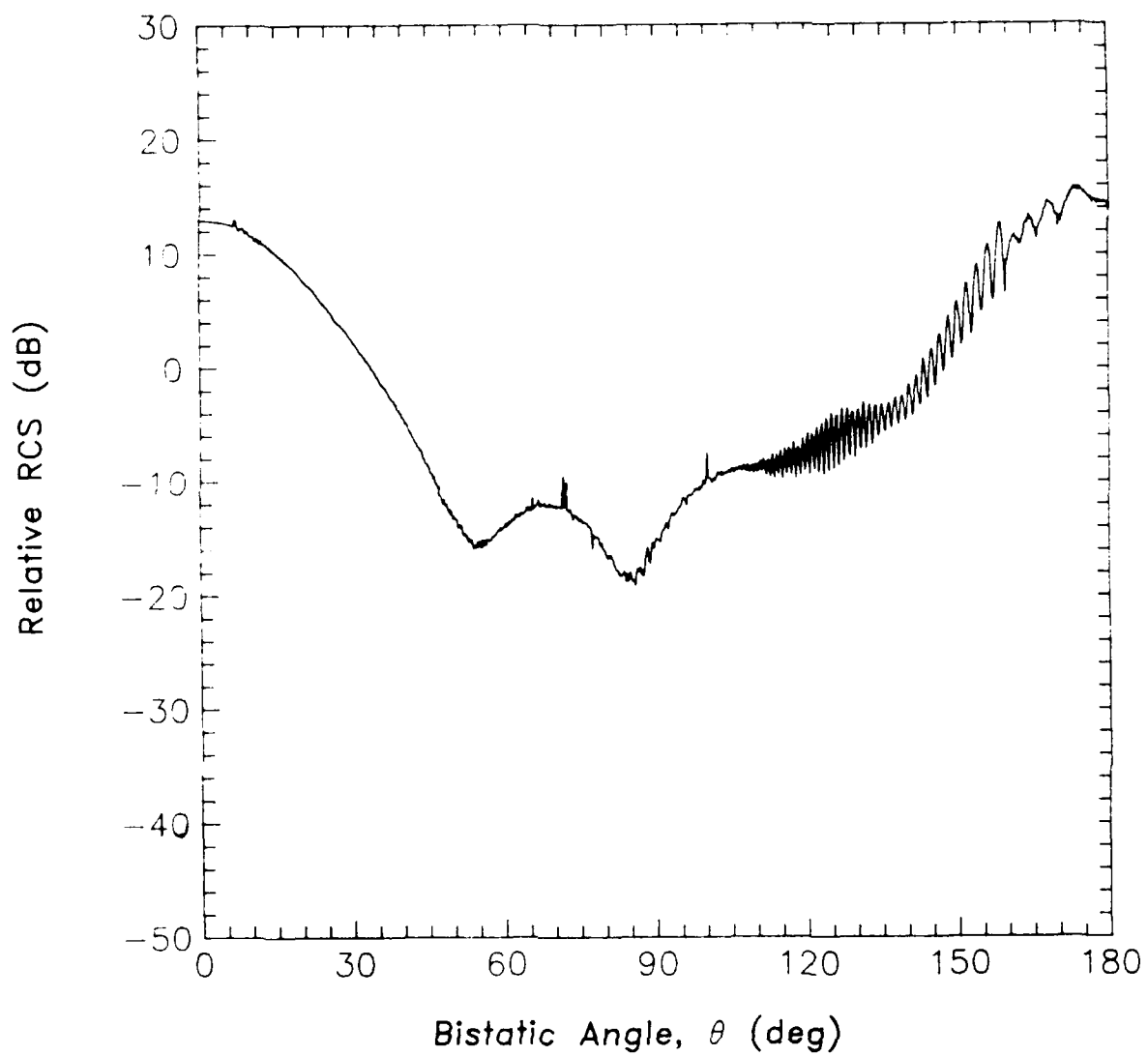


Figure 21(a). Measured 45°-Plane RCS of an Aluminum Cube with Side Length 1.5λ Before Spatial Filtering and with the Backscattering Lobe Artificially Fit to the $\sin(x)/x$ Function.

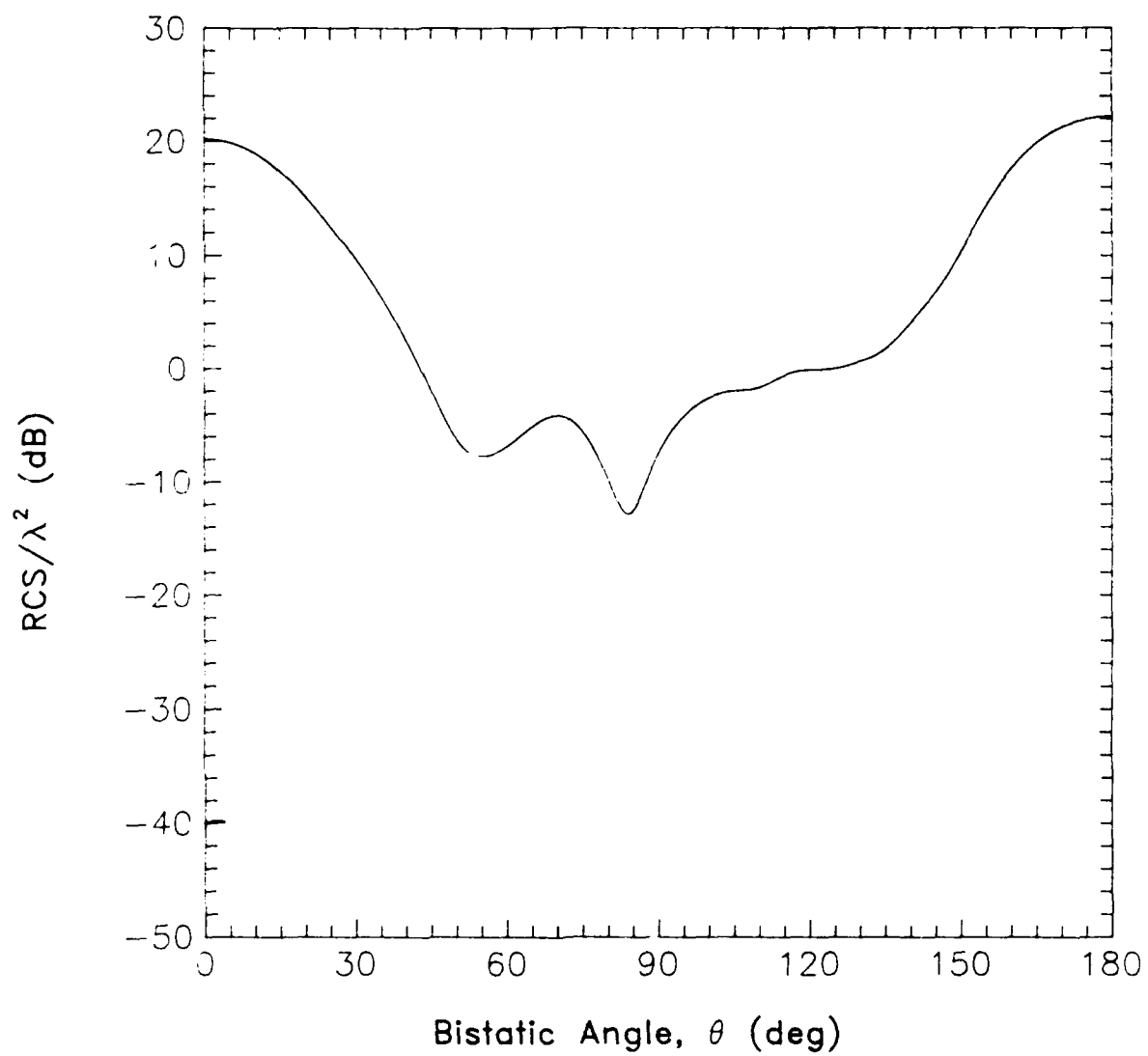


Figure 21(b). Measured 45°-Plane RCS of an Aluminum Cube with Side Length 1.5λ After Spatial Filtering.

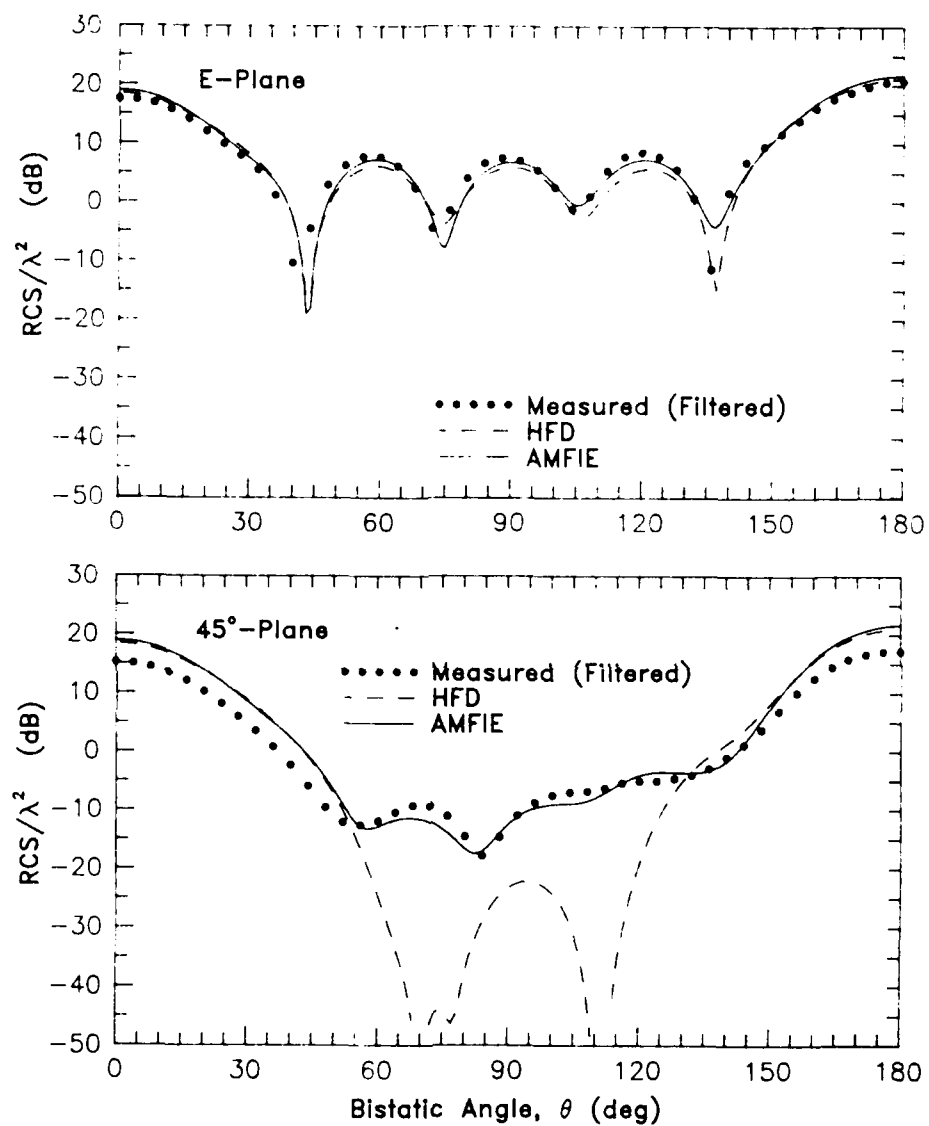


Figure 22. Scattering from Cube with Side Length 1.5λ .

were computed from the augmented magnetic field integral equation² (AMFIE) solution and the dashed lines were computed from the high frequency diffraction (HFD) solution.² We note that the AMFIE solution predicts the cube scattering in the 45°-plane more accurately than the HFD solution. This is because in the 45°-plane diffraction from the corners of the cube dominates the central portion of the scattered field and the HFD neglects these contributions.²

Figures 23 and 24 show the measured E-plane and 45°-plane RCS for a cube with side length 3λ . Figure 23(a) is the measured E-plane RCS, before filtering. Figure 23(b) is the E-plane RCS after filtering. Figure 24(a) is the 45°-plane RCS before filtering and Figure 24(b) is the 45°-plane RCS after filtering. We notice the smoothing effect of the filtering. Figure 25 shows the filtered measured RCS (dotted lines) plotted against the AMFIE (solid lines) and HFD (dashed lines) predictions for this 3λ cube.

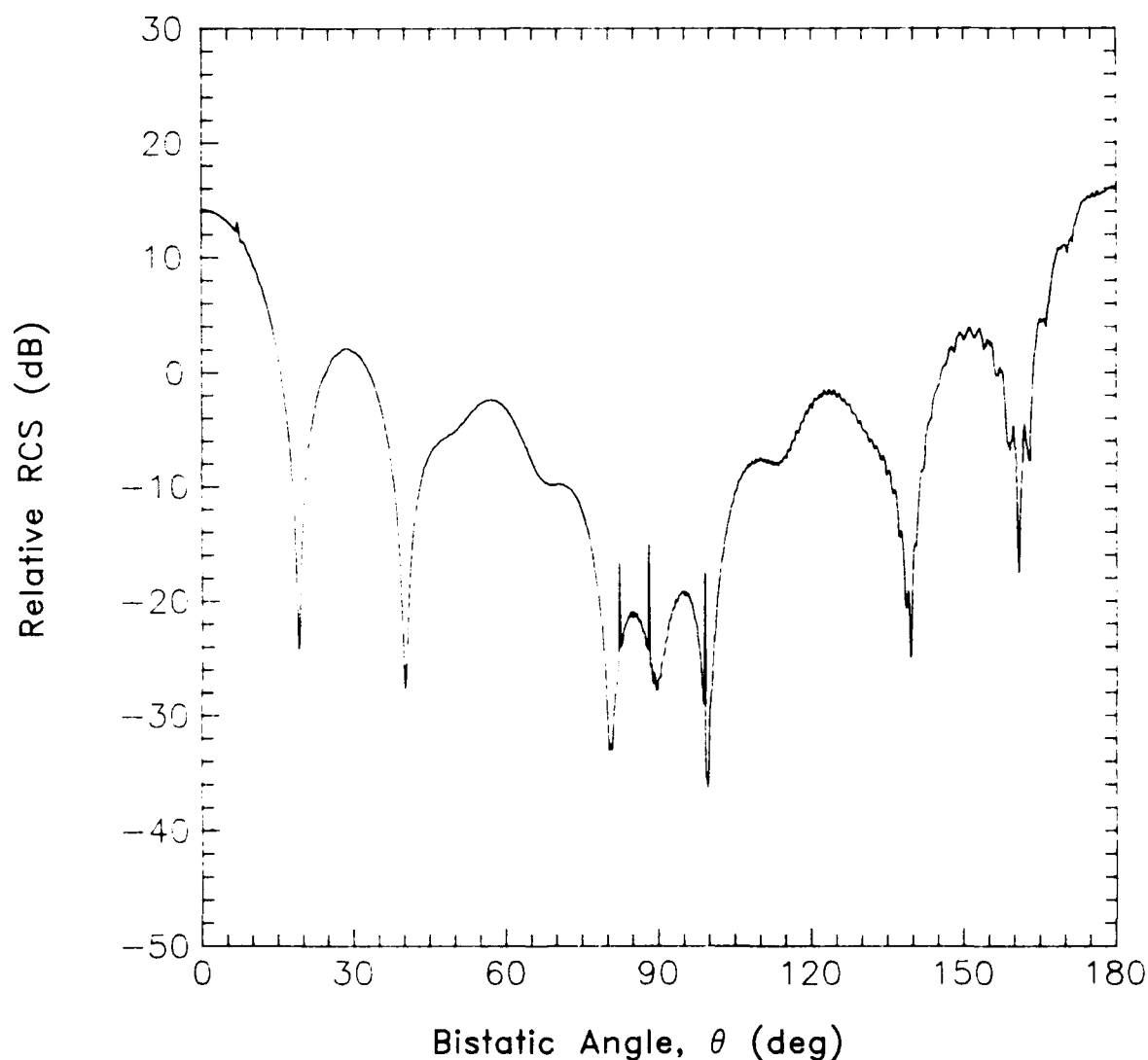


Figure 23(a). Measured E-Plane RCS of an Aluminum Cube with Side Length 3.0λ Before Spatial Filtering and with the Backscattering Lobe Artificially Fit to the $\sin(x)/x$ Function.

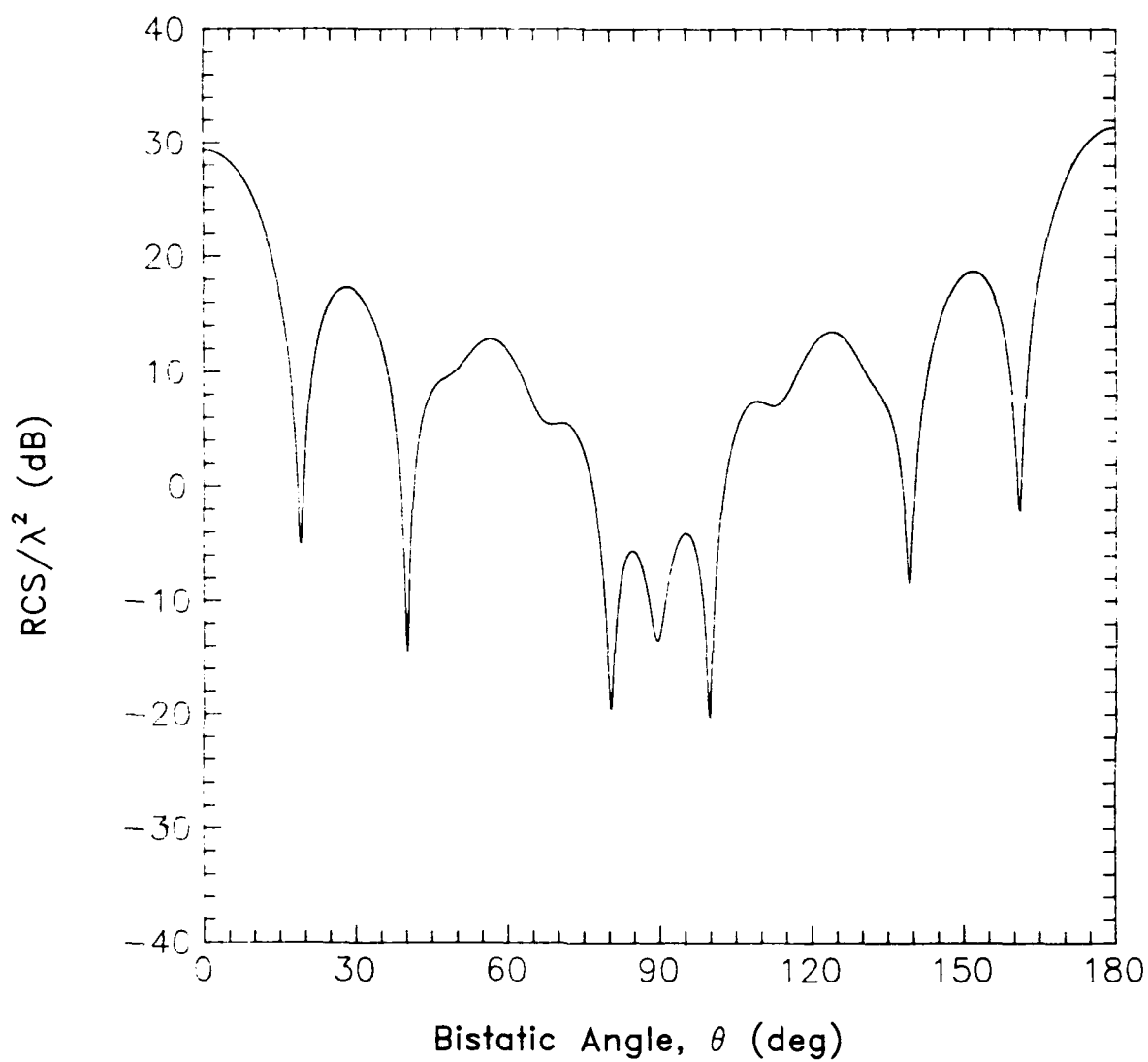


Figure 23(b). Measured E-Plane RCS of an Aluminum Cube with Side Length 3.0λ After Spatial Filtering.

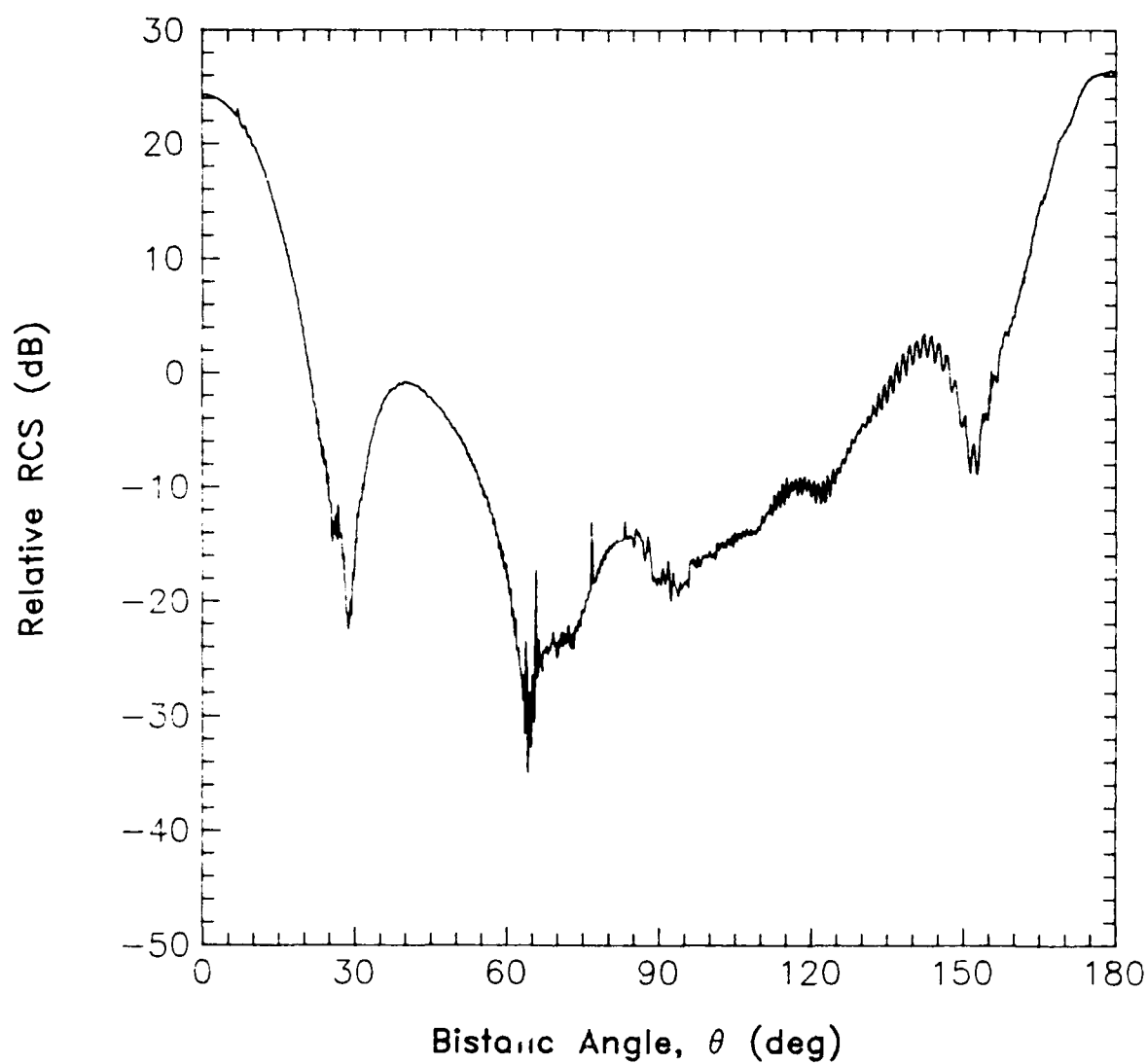


Figure 24(a). Measured 45°-Plane RCS of an Aluminum Cube with Side Length 3.0λ Before Spatial Filtering and with the Backscattering Lobe Artificially Fit to the $\sin(x)/x$ Function.

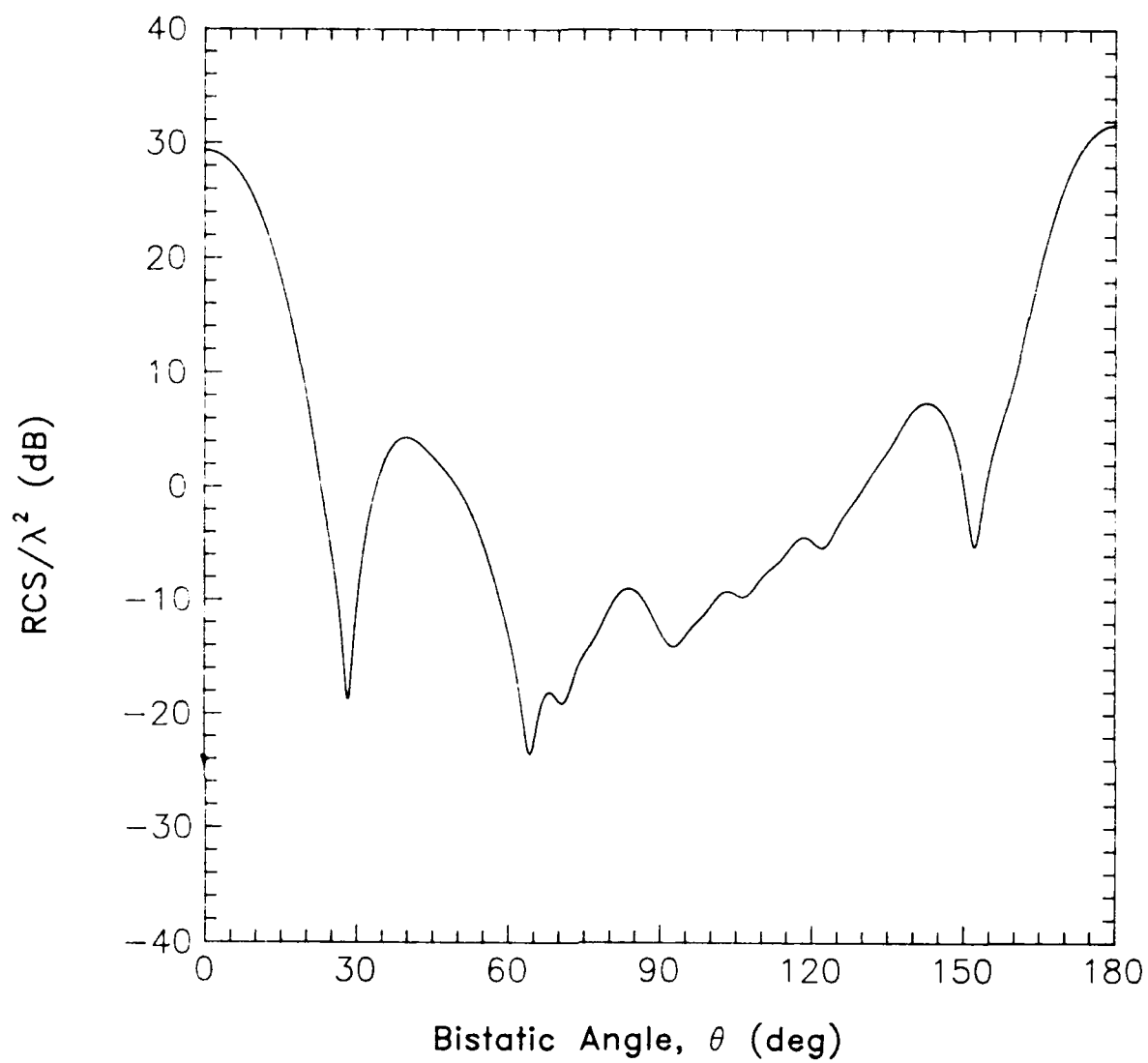


Figure 24(b). Measured 45°-Plane RCS of an Aluminum Cube with Side Length 3.0λ After Spatial Filtering.

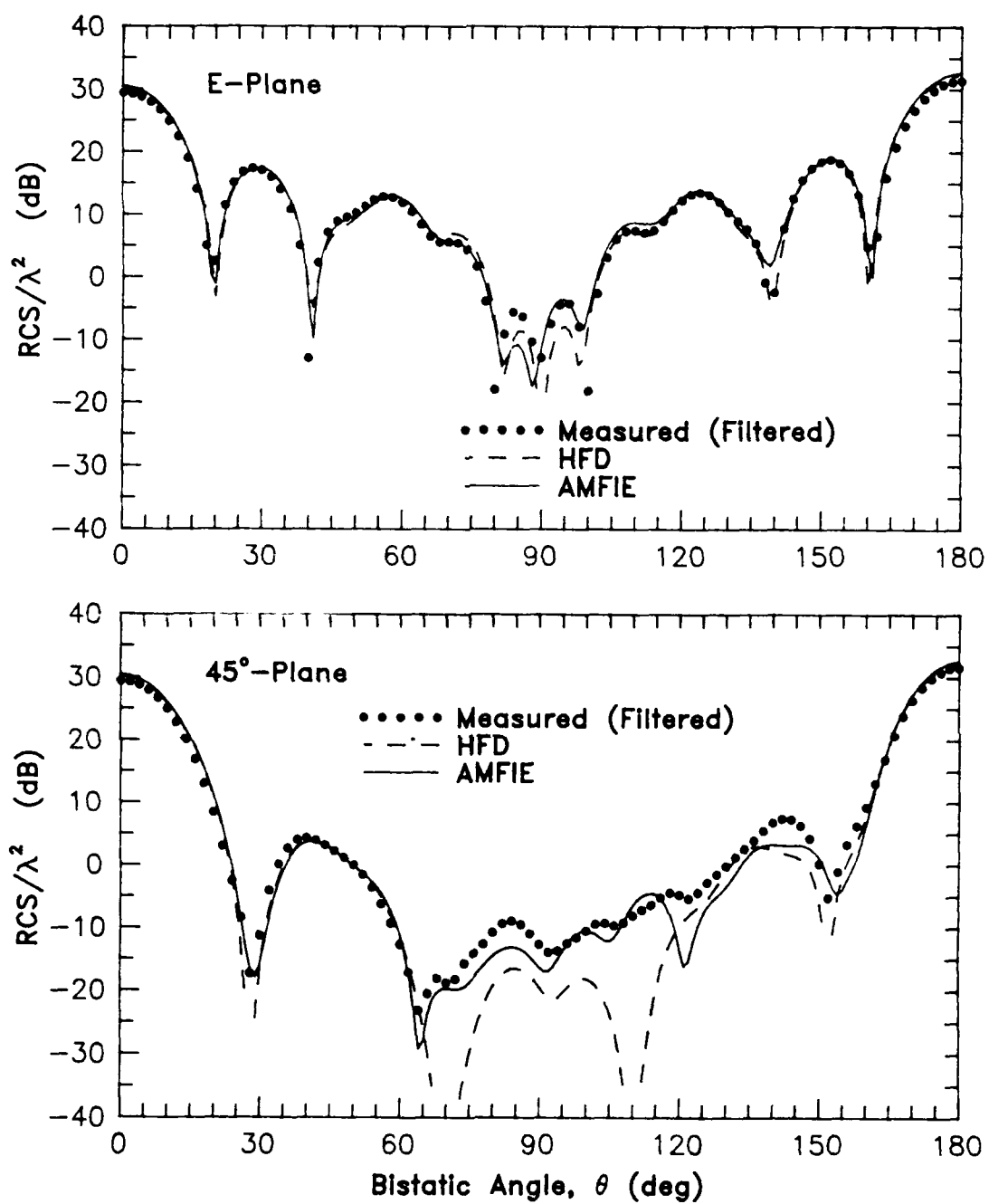


Figure 25. Scattering from Cube with Side Length 3.0λ .

The examples considered thus far in this section have demonstrated the smoothing effect of the spatial filtering. However, in all these examples the gross structure of the scattering pattern before filtering remained after the filtering. We present a final example, that of E-plane scattering from the 3λ metal cube for broadside plane-wave incidence, to demonstrate that the filtering can have a dramatic effect on the raw measured scattered field. Specifically this measured data demonstrates that the filtering can reveal structure in the measured scattered field that was hidden in the unfiltered measurements. The unfiltered RCS is shown in Figure 26(a). The backscattering lobe ($0^\circ \leq \theta \leq 20^\circ$) and part of the forward scattering lobe ($175^\circ \leq \theta \leq 180^\circ$) were artificially taken to be constant. This was done because data was only collected over the observation interval $20^\circ \leq \theta \leq 175^\circ$. We see the familiar high frequency rippling in the forward scattering region. Around $\theta = 90$ degrees we note a low level region with relatively large rippling that gives little clue as to the underlying structure. Figure 26(b) shows the 3λ cube E-plane RCS after filtering (22 modes were used). Here we see the high frequency rippling has been removed but more importantly we see two distinct lobes in the region around $\theta = 90$ degrees. The filtering has revealed information about the measured scattered field that was hidden in the raw data. Figure 27 shows the filtered measured E-plane scattered field of the 3λ cube plotted against the HFD and AMFIE predicted curves. Comparing the curves of Figure 27 we notice that the two lobes (around $\theta = 90$ degrees) do not have the same RCS values as the predicted curves but they do occur at the same observation angles. Thus, this measured data does not show as good agreement with the predicted E-plane RCS of the 3λ metal cube as the previous measured data (Figure 25). However, it does show that the filtering can have a large effect on the raw measurements and uncover information that is hidden in phase errors.

6. SUMMARY AND CONCLUSIONS

Automated swept-angle CW bistatic scattering measurements contain phase errors due to the receiver and the positioning system. When the background data is subtracted from the total field to obtain the measured scattered field, large errors are introduced from the small phase errors in the raw measurements. The size of this error is directly proportional to the amplitude of the background field relative to the true scattered field of the target. Part of the error is manifest as a high frequency rippling riding on top of the measured scattered field. Because electromagnetic energy scattered from targets is band limited [$n < 1.1k(a + \lambda)$] with respect to observation angle, the out-of-band error can be removed by spatial filtering without compromising the integrity of the target scattered-field.

In Section 2 we described the automated swept-angle bistatic scattering measurement procedure. We identified that the three significant error sources ultimately effecting the measured scattered field are receiver amplitude and phase errors, azimuth positioning error and vibrations and shifts of the long boom supporting the transmitting antenna.

In Section 3 we addressed how the non-perfect repeatability of consecutive measurement scans, caused by the errors discussed in Section 2, affects the measured scattered field. We defined the error in the measured scattered field $U(\theta)$. We studied the error by comparing a predicted error curve and an actual error curve for two examples. That of scattering from an aluminum cube with a side length of 1.5λ for broadside incidence, and that of scattering from an aluminum sphere with circumference 18λ . The predicted error curves were computed using the

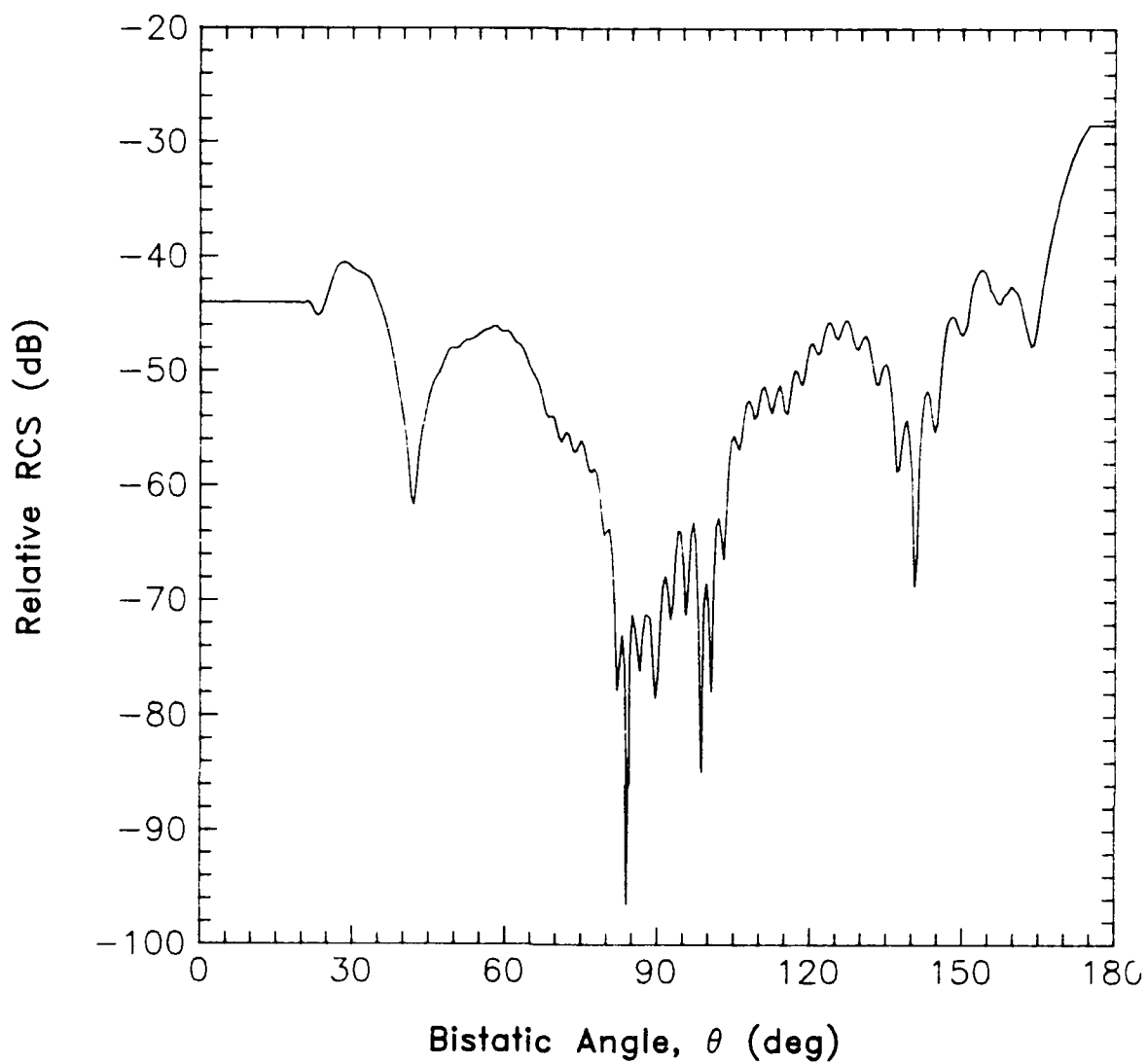


Figure 26(a). Measured E-Plane RCS of an Aluminum Cube with Side Length 3.0λ Before Spatial Filtering and With Both Forward-Scattering and Backscattering Lobes Artificially Set to a Constant.

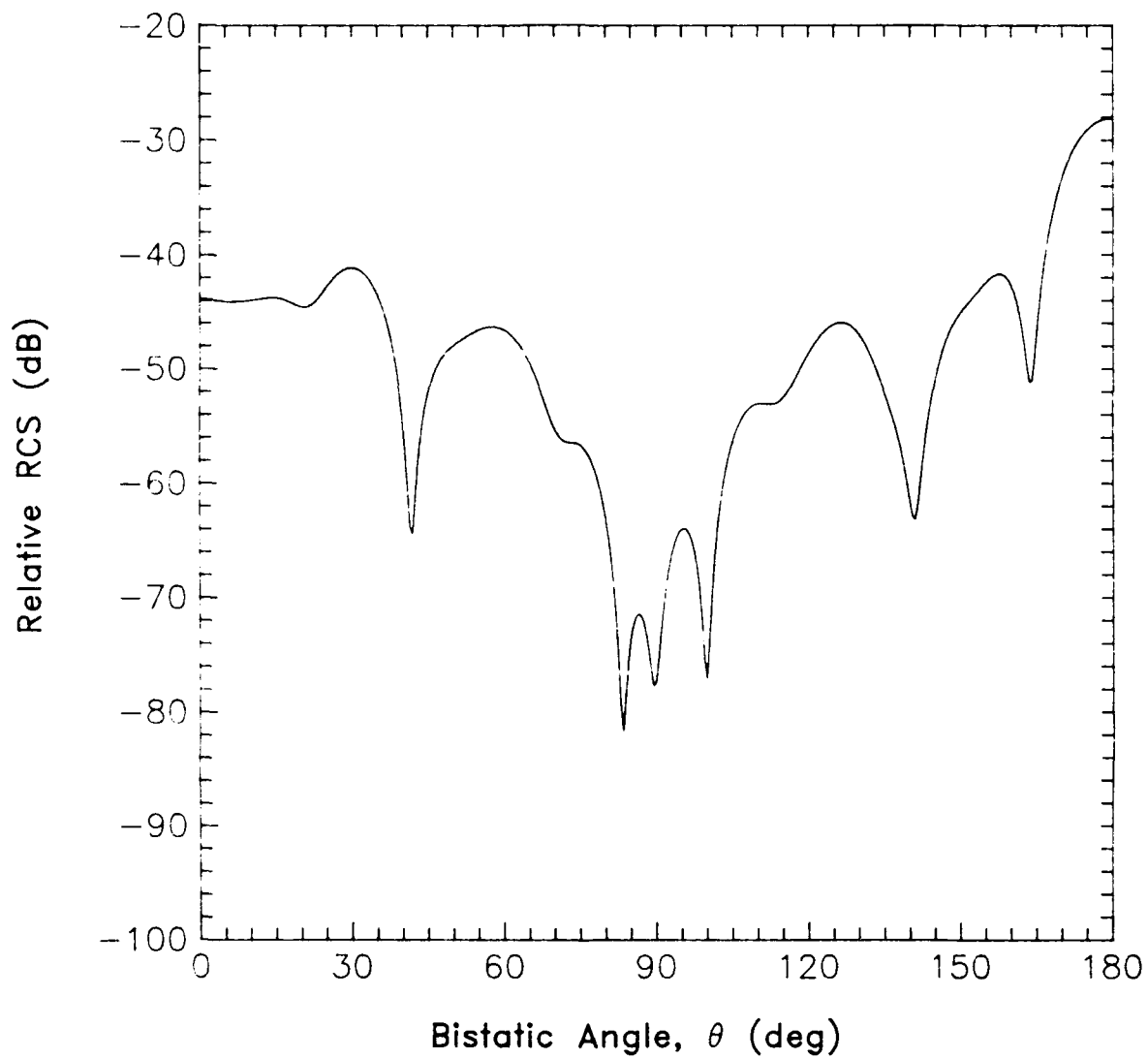


Figure 26(b). Measured E-Plane RCS of an Aluminum Cube with Side Length 3.0λ After Spatial Filtering.

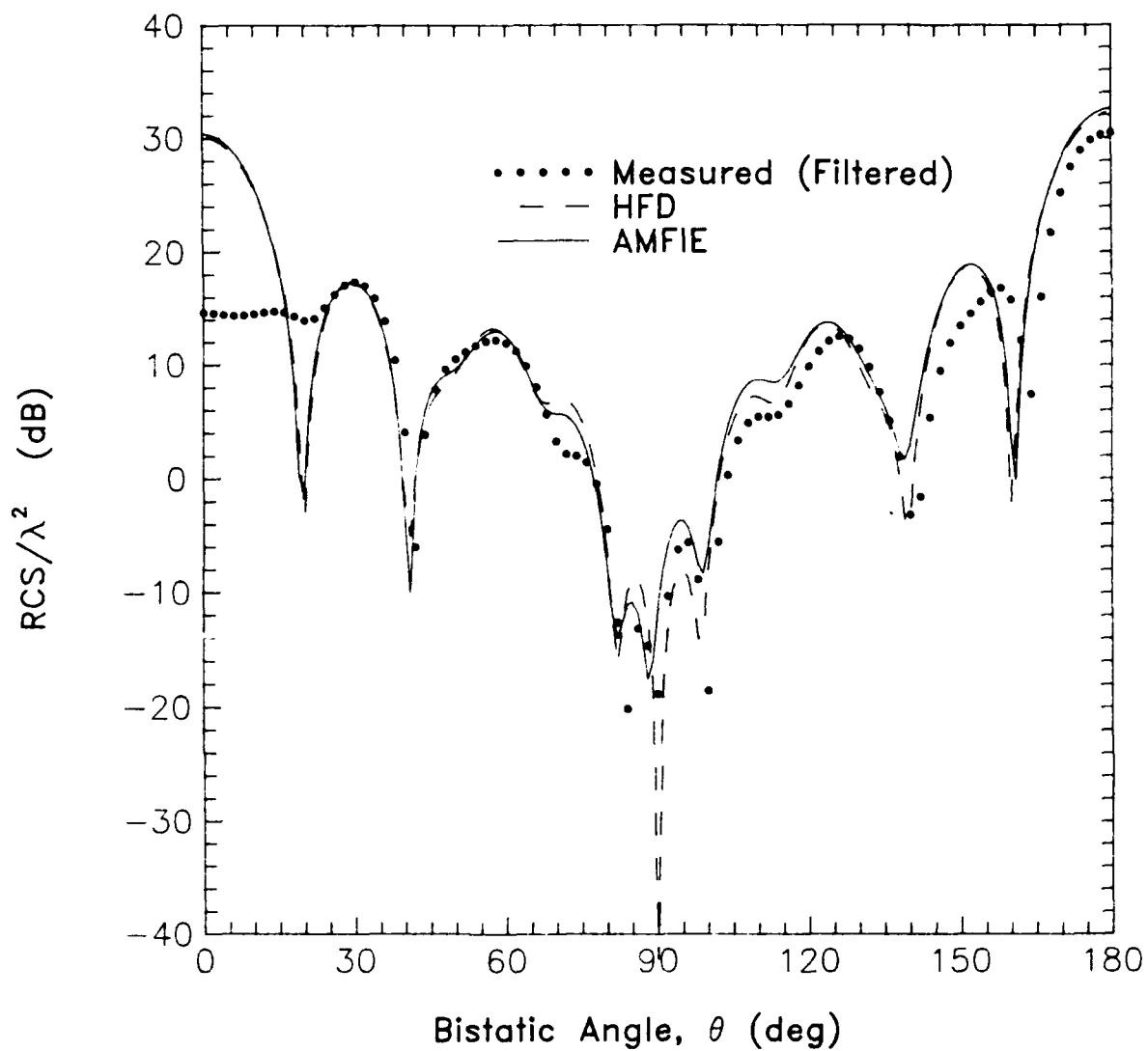


Figure 27. Scattering from Cube with Side Length 3.0λ .

true scattered field of the target and two independent background data sets. The actual error was computed directly using the true scattered field of the target and the measured scattered field. In the cube example, we saw that receiver and positioning errors were not the only sources of error. The other sources were not conclusively identified but are probably caused by errors in the high-frequency diffraction solution used to compute the true scattered field from the cube. In the sphere example, the measured error was consistent with receiver and positioning system sources. We demonstrated that part of the error was manifest as a high frequency variation riding on top of the true scattered field, and that the error was worse in the forward scattering region.

In Section 4 we described the spatial filtering technique. We showed how the natural band limit of the target scattered field could be used effectively to remove the high frequency error in the target measured scattered field.

In Section 5 we presented a number of examples to demonstrate the filtering technique. One example, that of E-plane scattering of a conducting cube with side length of 1.5λ for broadside incidence, showed that in addition to smoothing, the spatial filtering could reveal information in measured scattering patterns that was hidden in the raw measurements. In all examples, the filtering significantly smoothed the high frequency errors in the measured scattering patterns.

References

1. Chu, L. J. (1948), Physical Limitations of Omni-Directional Antennas *Journal of Applied Physics*, **19**:1163-1175, December 1948.
2. Cote M. G., Woodworth M. M., and Yaghjian A.D. (1988), "Scattering from the Perfectly Conducting Cube," *IEEE Transactions on Antennas and Propagation*, Vol. AP-36, No. 9.
3. DiBeneditto, J. P. (1984), *Bistatic Scattering From Conducting Calibration Spheres*, RADC-TR-84-93. ADA154173
4. Collin, R. E. and Rothschild, S. (1963), Evaluation of Antenna Q *IEEE Transactions on Antennas and Propagation*, **AP-12**:23-27, January 1964.
5. Yaghjian A.D. (1986), "An Overview of Near-Field Antenna Measurements," *IEEE Transactions on Antennas and Propagation*, Vol. AP-34, No. 1, 30-45, January 86.
6. Stratton, J. A., (1941), *Electromagnetic Theory*, McGraw-Hill, pp. 392-420.
7. Hansen, J. E. (1988), *Spherical Near-Field Antenna Measurements*, Peter Peregrinus Ltd., London, United Kingdom.
8. Abramowitz, M., and Stegun, I., (1970), *Handbook of Mathematical Functions With Formulas, Graphs, and Mathematical Tables*, United States Department of Commerce, Chapters 9 and 10.
9. Blacksmith, P., Hiatt, R. E., and Mack, R. B., "Introduction to Radar Cross-Section Measurements," *Proceedings of the IEEE*, Vol. 53, No. 8, pp. 901-920, August 1965.

Appendix A:

Discussion of the General Behavior of Scattering From Targets of Finite Size

L. J. Chu¹ showed that current distributions (antennas, targets) produce scattered far fields that are spatial frequency band limited and that the band limit is governed by the target size. Specifically the true scattered field of a target that can fit into a minimum sphere⁷ of radius "a," will have a spatial frequency components no larger than $1.1k(a + \lambda)$. In practice, the measured scattered field may well contain frequencies larger than $1.1k(a + \lambda)$. This is because the measured scattered field is derived from the subtraction of two sets of imperfect measurements, the background field and total field with target present, both of which are produced from currents that are far from the center of the measurement system and thus the radius of the minimum sphere is quite large. For example, in the swept-angle bistatic measurements (see Section 2) there are currents set up on the anechoic chamber wall, the transmitting antenna, and the positioning apparatus. The minimum sphere for these measurements is large enough to contain the entire anechoic chamber. The major contributions to the measured fields, however, will be from the target and the transmitting antenna. Thus, the total and background fields will, in general, have spatial frequency bandwidths of $1.1k(a + \lambda)$ where a is the distance from the center of the probe coordinate system (usually where the target is placed) to the transmitting antenna.

The physics tells us that the total and background fields can contain higher frequency components than the target scattered field, it does not guarantee that they will contain them. We would however, expect that the total and background fields would vary much more rapidly than the target scattered field does, because the direct coupling path length (and thus the phase),

⁷Hansen, J. E. (1988), *Spherical Near-Field Antenna Measurements*, Peter Peregrinus Ltd., London, United Kingdom.

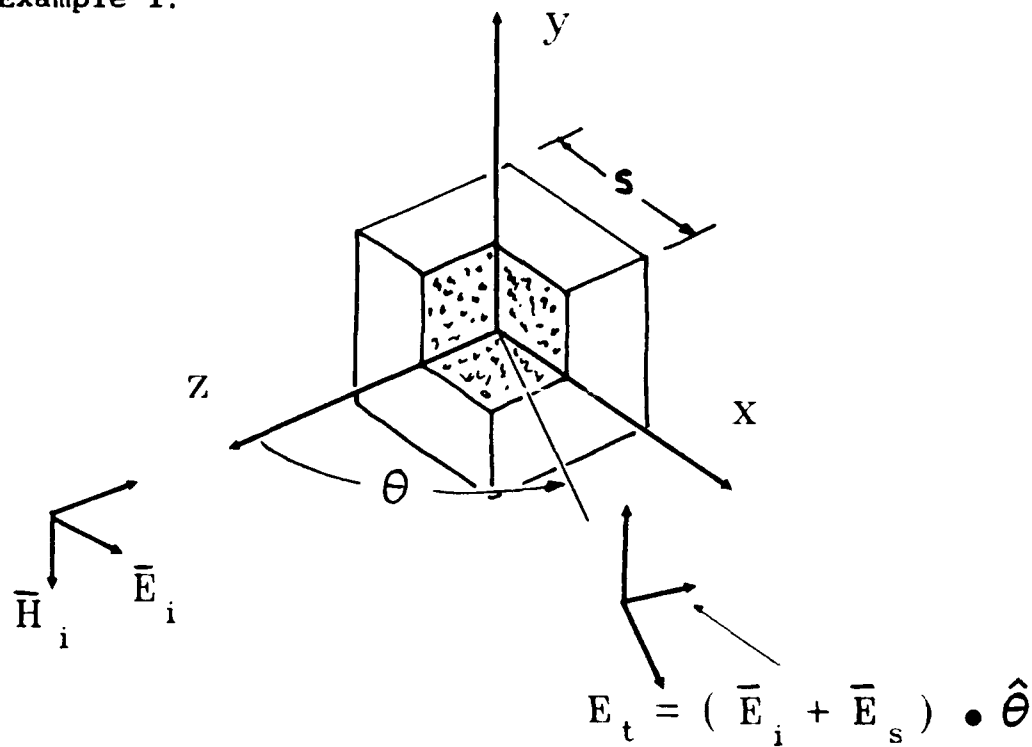
which is present in both the total and background fields, changes very rapidly with observation angle.

Figures A1 through A3 present three examples of the measured background fields and target scattered fields to illustrate that the spatial frequency content is much greater for the background fields than for target scattered fields. Each example is a collection of five (5) pages with each page containing the following information:

- Page 1) Measurement parameters, geometry, and target description.
- Page 2) Measured background field (target not present), amplitude [top graph], and phase [bottom graph].
- Page 3) Measured total field (target present), amplitude [top graph], and phase [bottom graph].
- Page 4) Measured target scattered field (background field subtracted from the total field), amplitude [top graph], and phase [bottom graph].
- Page 5) Spatial spectra of the measured background field [top graph], measured total field [middle graph], and measured target scattered field [bottom graph].

When comparing the curves of each example one should note the contrast between the phase curves in the backscattering regions of the background and total fields. For the examples presented the target scattered fields dominate the backscattering region of the total field so that the phase variations in this region are due to the target scattered field component of the total fields. Since the total field phase curves vary much more slowly than the phase curves of the background field in the backscattering region, we can infer that the phase of the target scattered fields vary much more slowly than the phase of the background fields.

Example 1:



TARGET DESCRIPTION

Name : $.75\lambda$ Cube
 Size : $s = 2.0$ cm
 Material : Aluminum
 Physical Band Limit -
 $1.1k(a+\lambda): 10.37$
 $a = \frac{s}{2} = 1.0$ cm

MEASUREMENT PARAMETERS

Frequency : 11.242 GHz
 Polarization -
 Receive : Horizontal ($\hat{\theta}$)
 Transmit : Horizontal (\hat{x})
 Incidence : Broadside to face
 cut : E-plane

Figure A1(a). Geometry, and Measurement Parameters for E-Plane Scattering from an Aluminum Cube with a Side Length of 0.75λ . [Example 1 page 1]

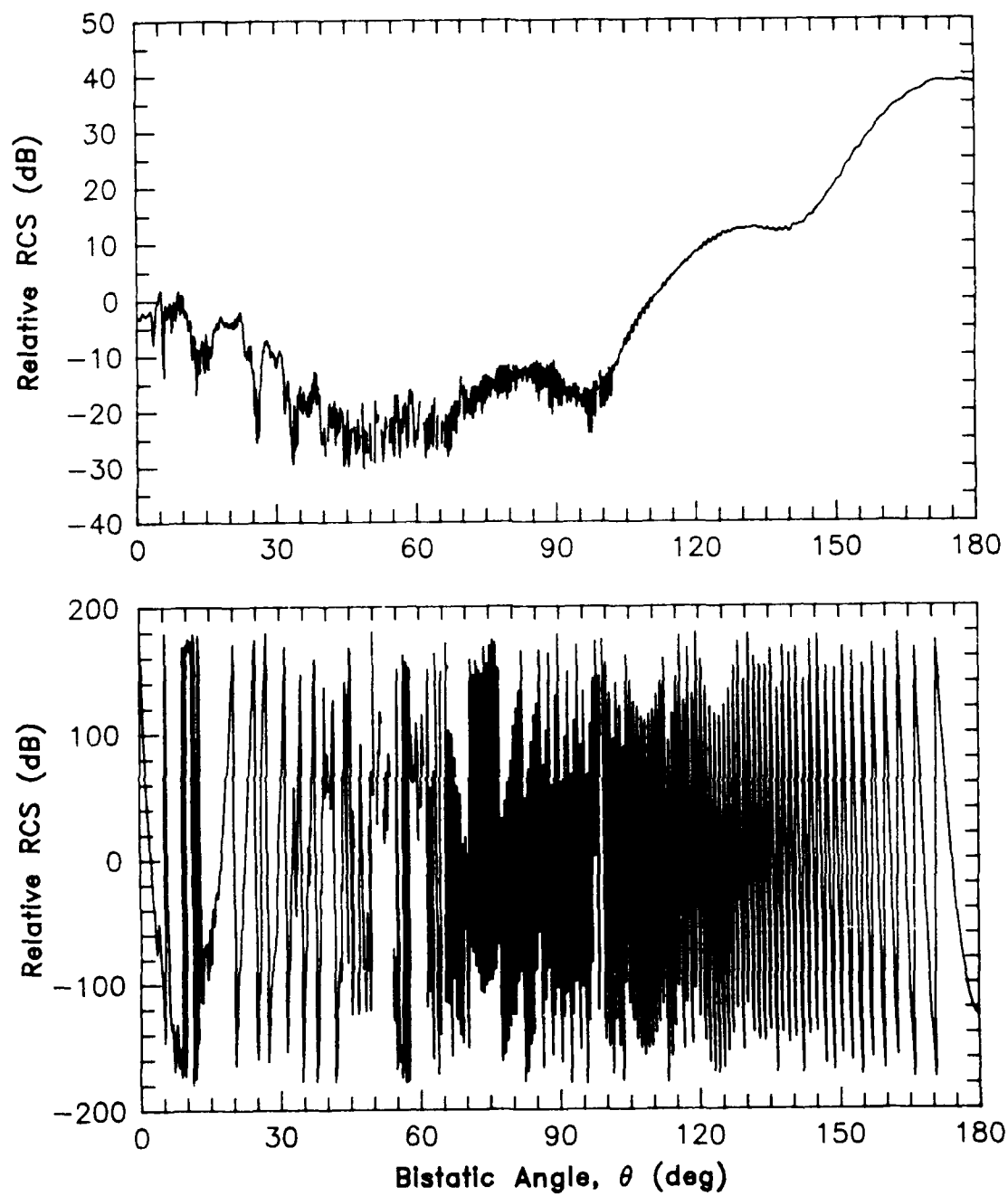


Figure A1(b). Measured Background Field (Amplitude and Phase) Associated with Scattering from a 0.75λ Cube. [Example 1 page 2]

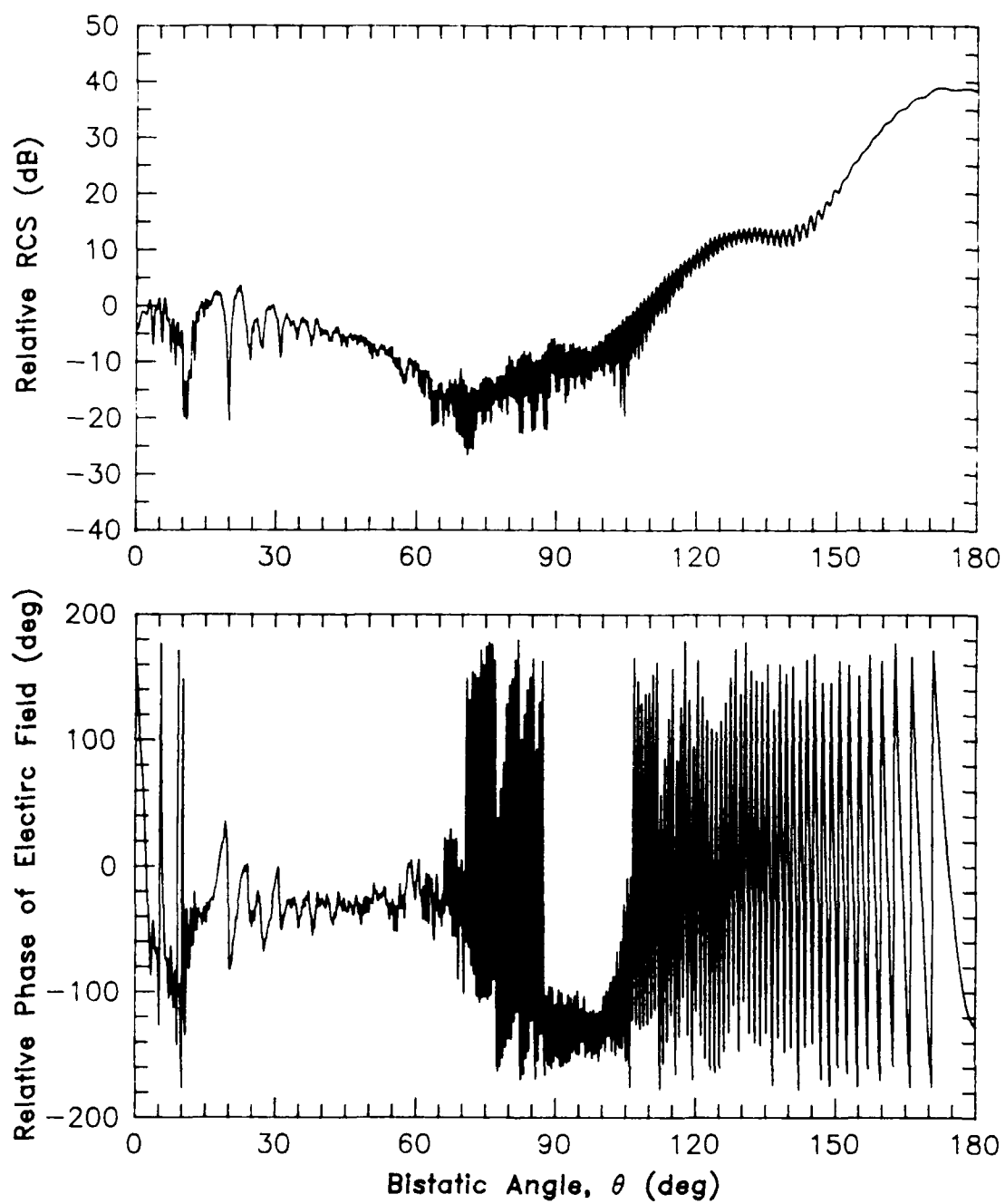


Figure A1(c). Measured Total Field (Amplitude and Phase) Associated with Scattering from a 0.75λ Cube. [Example 1 page 3]

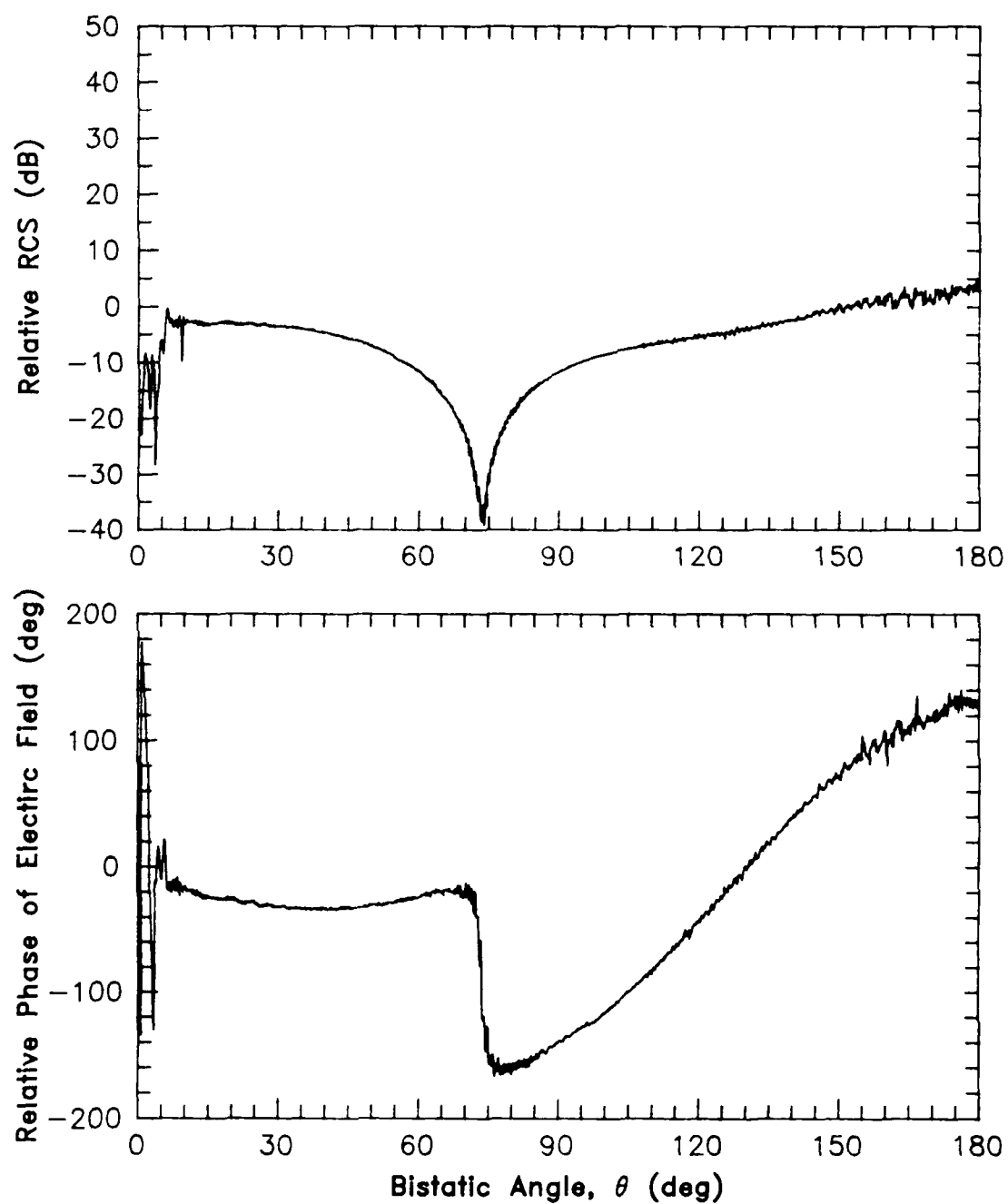


Figure A1(d). Measured Scattered Field (Amplitude and Phase) of an Aluminum Cube with Side Length 0.75λ . [Example 1 page 4]

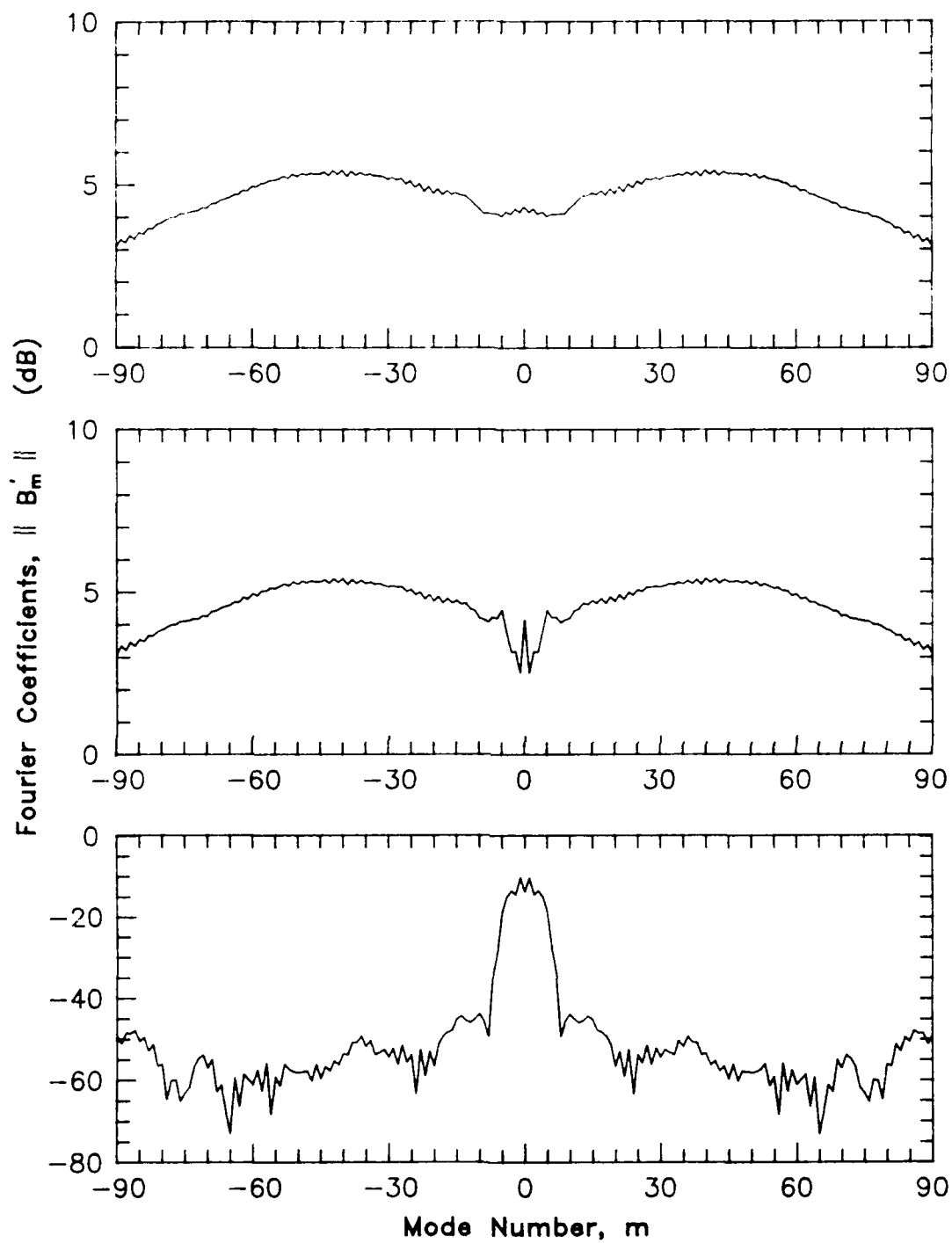
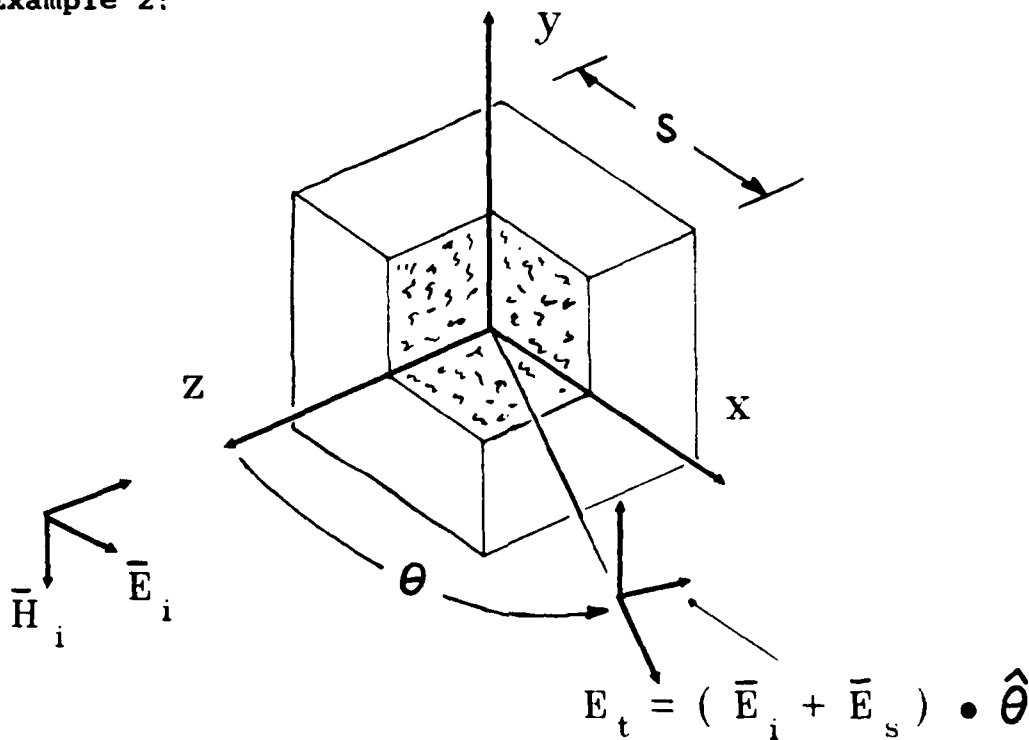


Figure A1(e). Spatial Spectra of the Background, Total, and Target Scattered Fields Associated with Scattering From a 0.75λ Cube. [Example 1 page 5]

Example 2:



TARGET DESCRIPTION

Name : 5λ Cube
 Size : $s = 15.24$ cm
 Material : Aluminum
 Physical Band Limit -
 $1.1k(a+\lambda): 24.19$
 $a = \frac{s}{2} = 7.62$ cm

MEASUREMENT PARAMETERS

Frequency : 9.8356 GHz
 Polarization -
 Receive : Horizontal ($\hat{\theta}$)
 Transmit : Horizontal (\hat{x})
 Incidence : Broadside to face
 cut : E-plane

Figure A2(a). Geometry, and Measurement Parameters for E-Plane Scattering From an Aluminum Cube with a Side Length of 5.0λ . [Example 2 page 1]

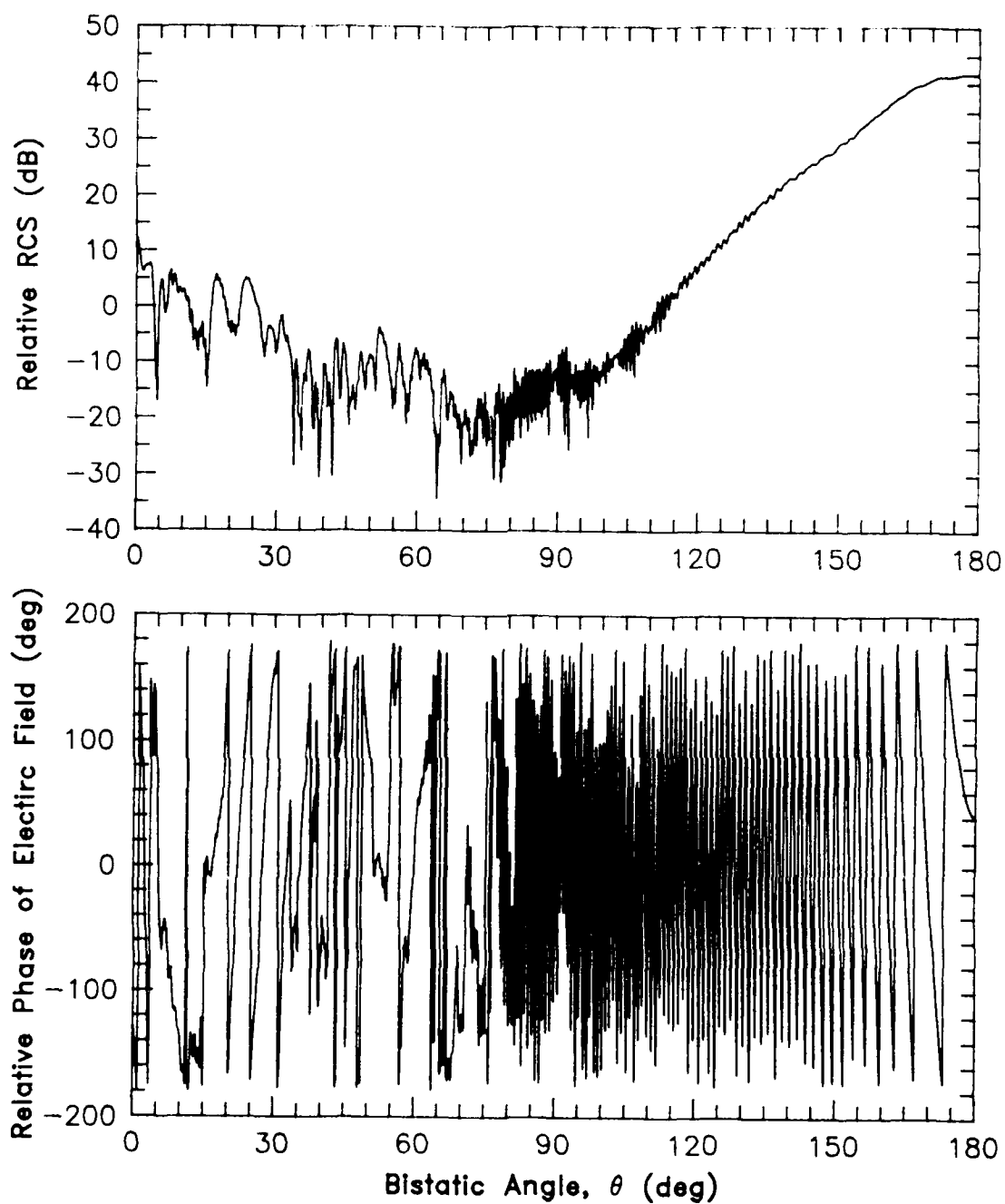


Figure A2(b). Measured Background Field (Amplitude and Phase) Associated With Scattering From a 5.0λ Cube. [Example 2 page 2]

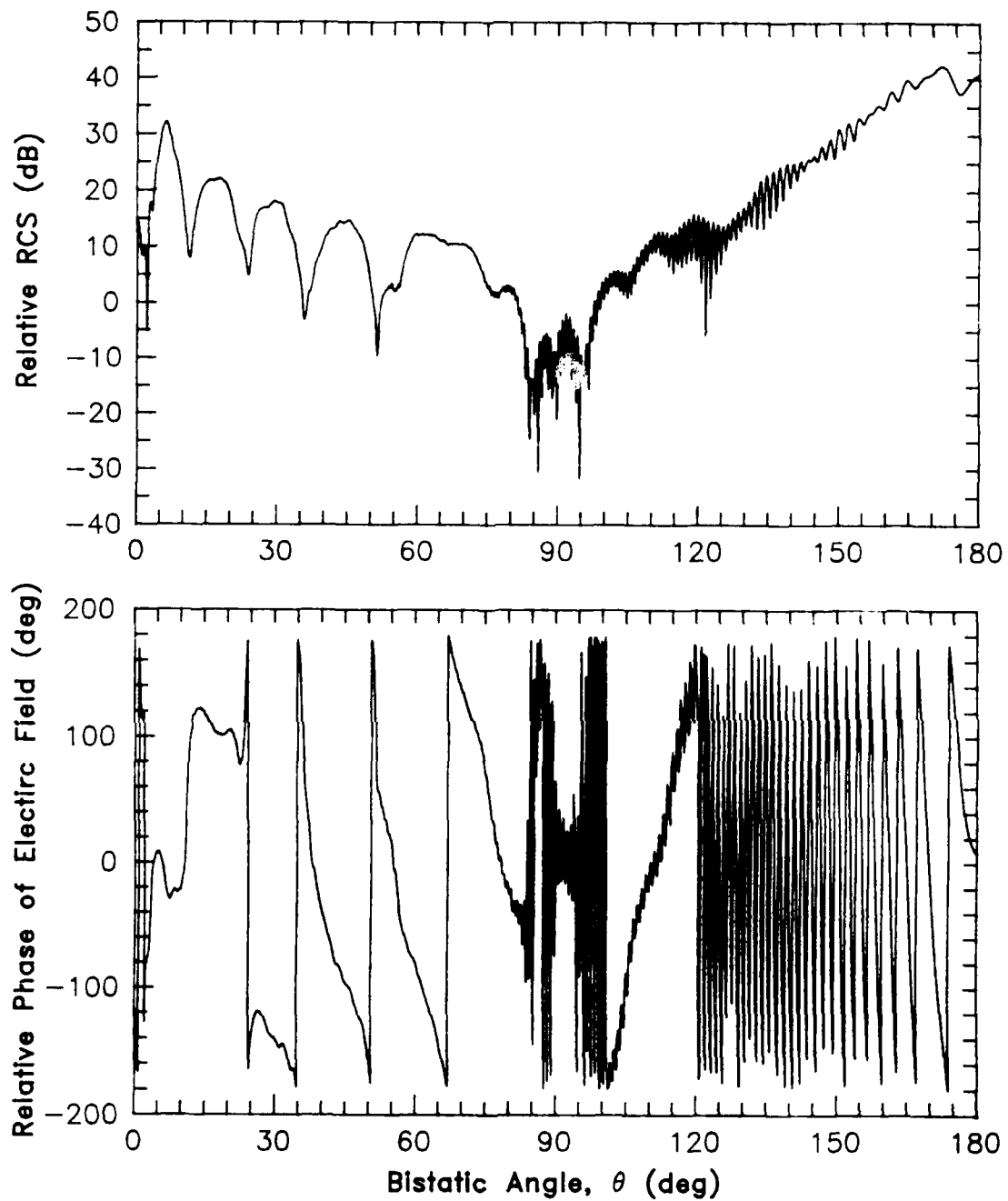


Figure A2(c). Measured Total Field (Amplitude and Phase) Associated With Scattering From a 5.0λ Cube. [Example 2 page 3]

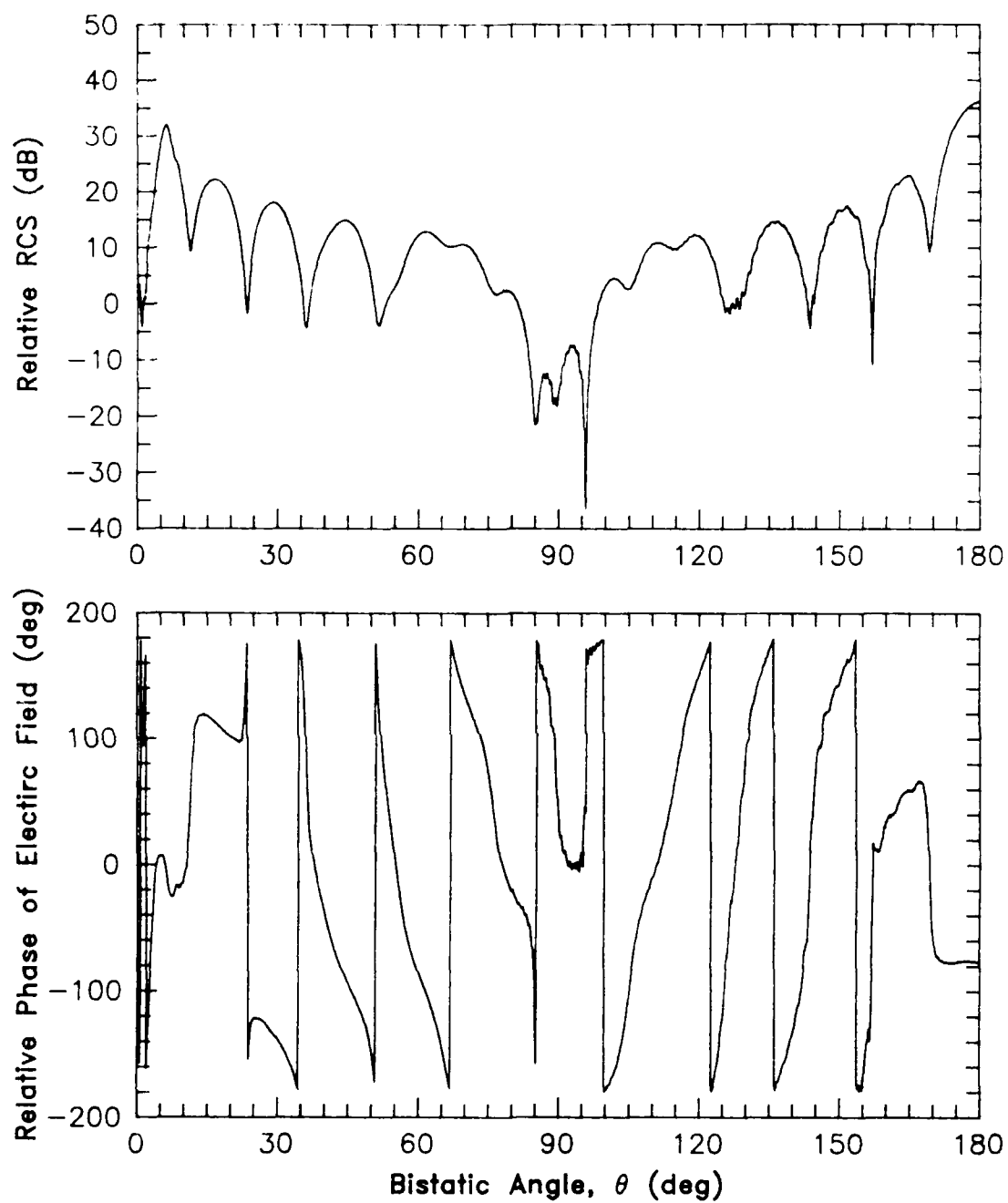


Figure A2(d). Measured Scattered Field (Amplitude and Phase) of an Aluminum Cube With Side Length 5.0λ . [Example 2 page 4]

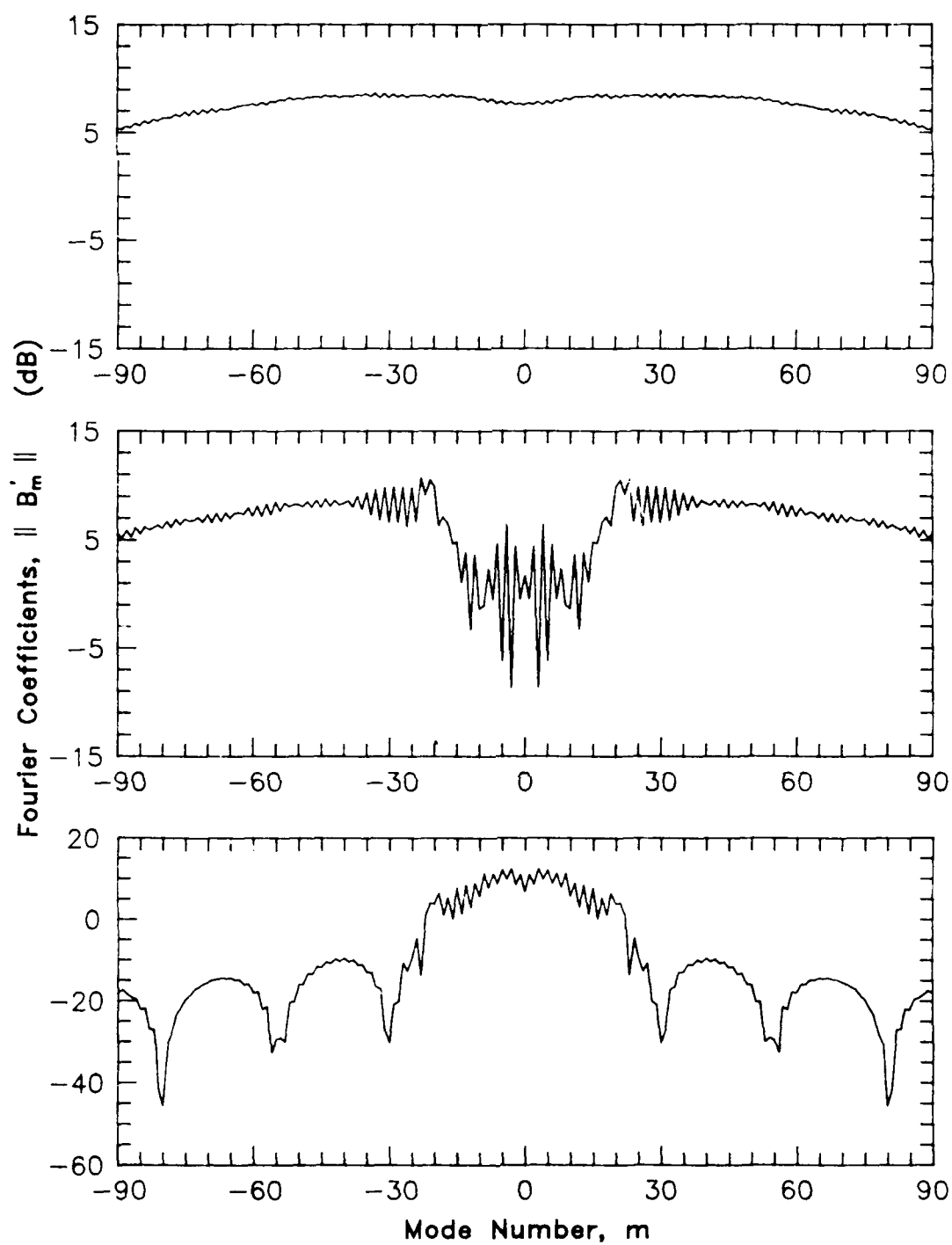
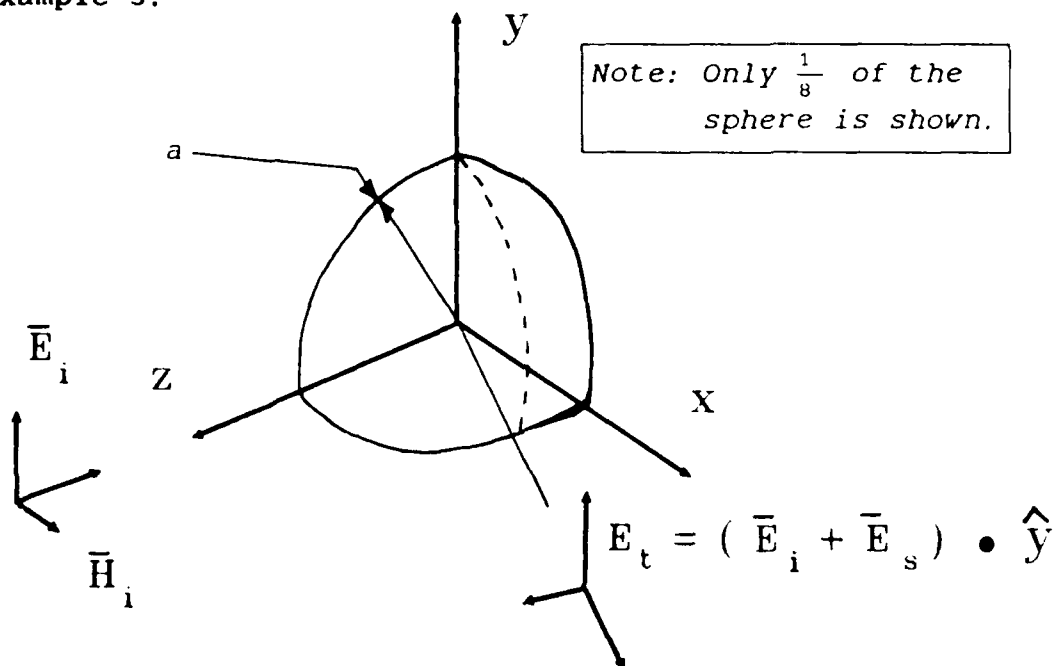


Figure A2(e). Spatial Spectra of the Background, Total, and Target Scattered Fields Associated with Scattering from a 5.0λ Cube. [Example 2 page 5]

Example 3:



TARGET DESCRIPTION

Name : 18λ sphere
 Size : $a = 7.62$ cm
 Material : Aluminum
 Physical Band Limit -
 $1.1k(a+\lambda)$: 26.63
 $a = \text{radius} = 7.62$ cm

MEASUREMENT PARAMETERS

Frequency : 11.242 GHz
 Polarization -
 Receive : Vertical ($\hat{\phi}$)
 Transmit : Vertical (\hat{y})
 Incidence : Along $-z$ axis
 cut : H-plane

Figure A3(a). Geometry, and Measurement Parameters for H-Plane Scattering From an Aluminum Sphere 17.95λ in Circumference. [Example 3 page 1]

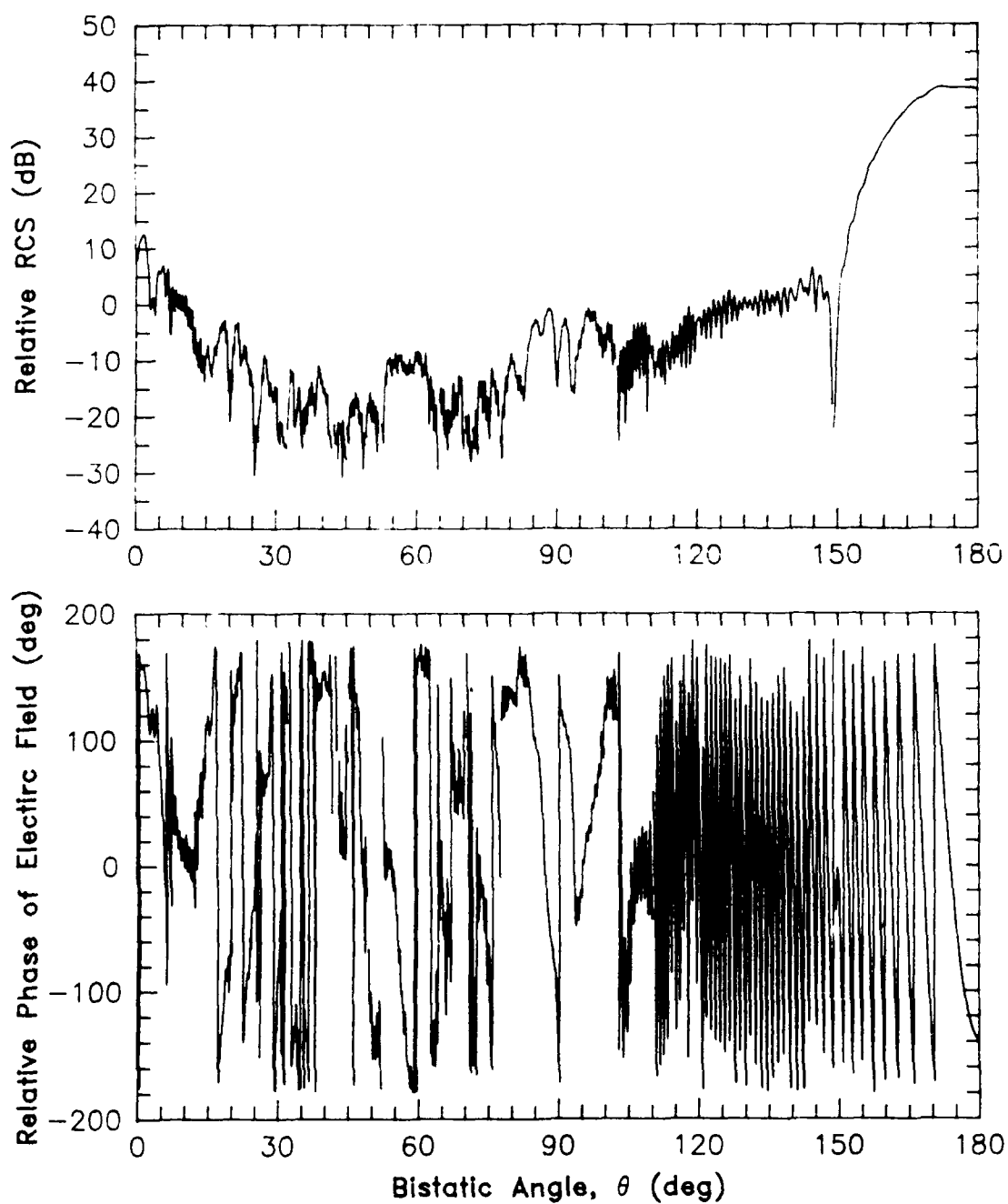


Figure A3(b). Measured Background Field (Amplitude and Phase) Associated with Scattering From a 17.95λ Sphere. [Example 3 page 2]

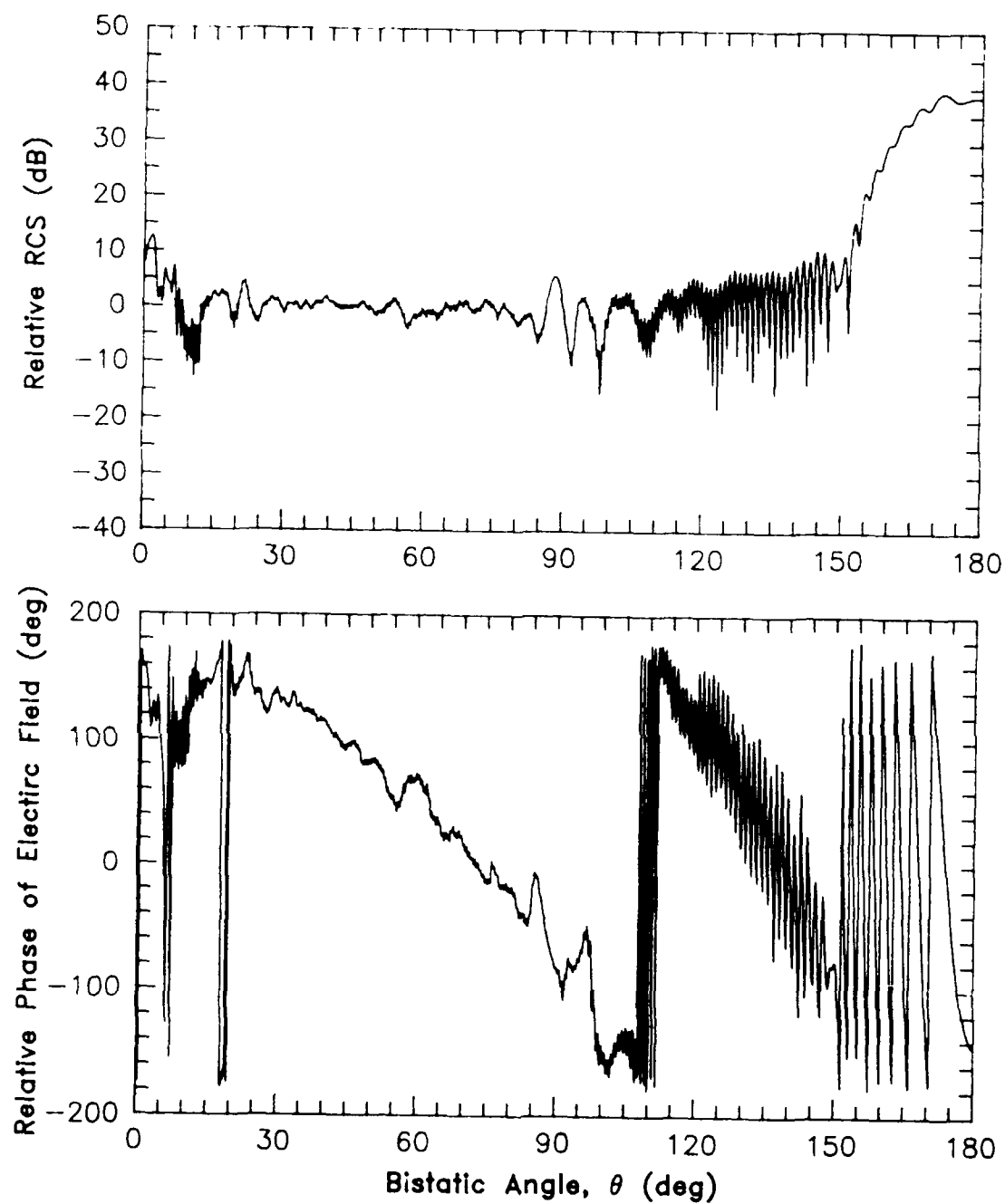


Figure A3(c). Measured Total Field (Amplitude and Phase) Associated with Scattering From a 17.95λ Sphere. [Example 3 page 3]

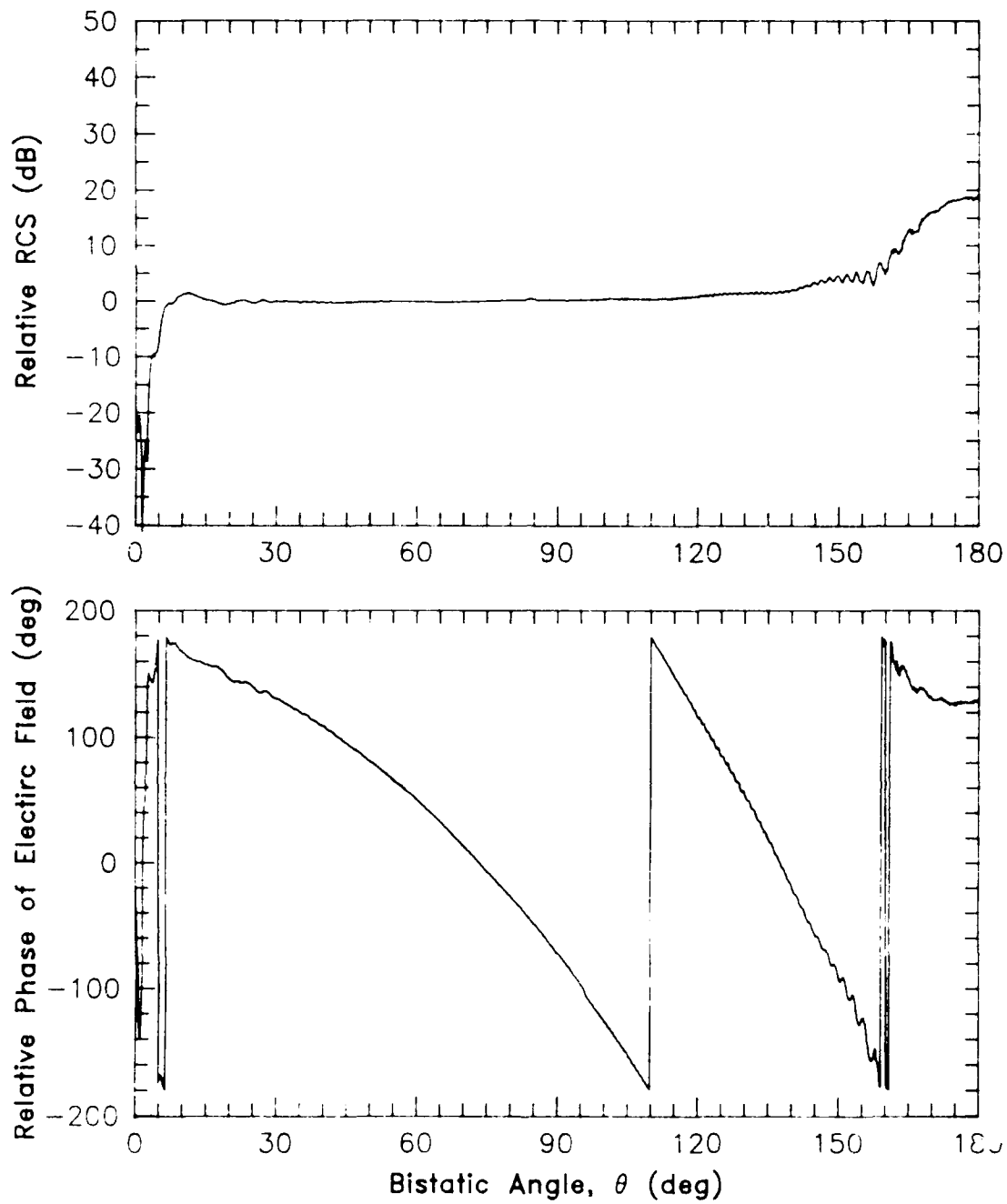


Figure A3(d). Measured Scattered Field (Amplitude and Phase) of an Aluminum Sphere With Circumference 17.95λ . [Example 3 page 4]

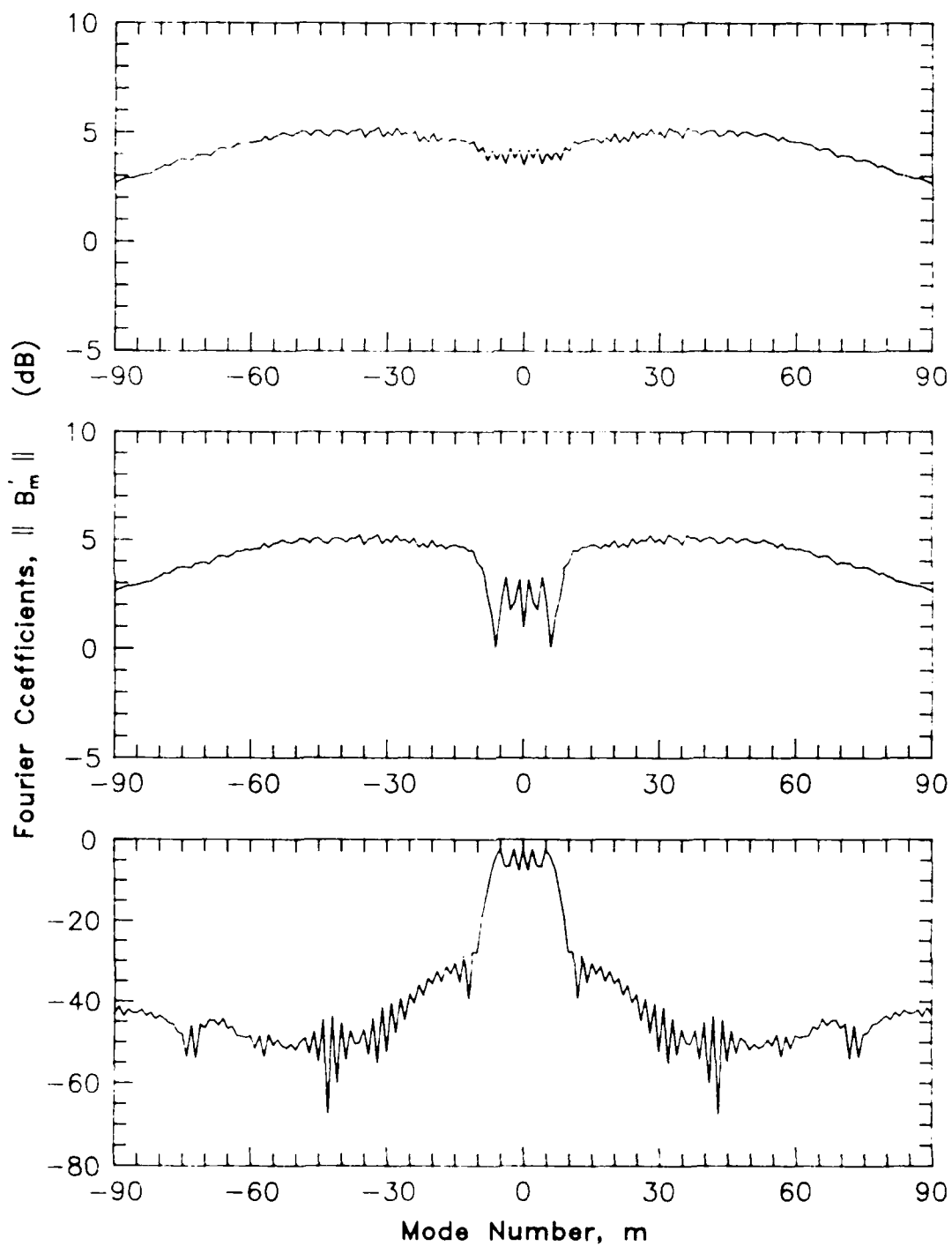


Figure A3(e). Spatial Spectra of the Background, Total, and Target Scattered Fields Associated with Scattering from a 17.95λ Sphere. [Example 3 page 5]

Appendix B:

A Demonstration of the Physical Band Limit of a General Target

Consider two point sources, located, one at each end of a diameter of an imaginary sphere of radius a centered at the origin. We compute a scalar radiated far field, $E(\theta)$, as a function of observation angle, θ .

$$E(\theta) = \frac{e^{-ikr_1}}{4\pi r_1} + \frac{e^{-ikr_2}}{4\pi r_2}, \quad (\text{B-1})$$

where k is the free space wave number, and r_1 and r_2 are the distances from the point sources to the far-field point. If we reference the phase to the origin we can rewrite Eq. (B1) as

$$E(\theta) = \frac{e^{-ik(r-a\sin\theta)}}{4\pi(r-a\sin\theta)} + \frac{e^{-ik(r+a\sin\theta)}}{4\pi(r+a\sin\theta)}.$$

Because $r \gg a$ we can further reduce the expression to

$$E(\theta) = \frac{e^{-ikr}}{4\pi r} \left[e^{+ika\sin\theta} + e^{-ika\sin\theta} \right]. \quad (\text{B-2})$$

We are interested in the spatial frequency bandwidth of the scattered field so we need to take the Fourier transform of $E(\theta)$ with respect to the observation angle θ

$$F[E(\theta)] = \sum_{n=-\infty}^{\infty} \left[\int_0^{2\pi} E(\theta) e^{-in\theta} d\theta \right] = \frac{e^{-ikr}}{4\pi r} \sum_{n=-\infty}^{\infty} \left[\int_0^{2\pi} e^{i(ka \sin \theta - n\theta)} d\theta + \int_0^{2\pi} e^{i(ka \sin \theta + n\theta)} d\theta \right]. \quad (B-3)$$

Both of the integrals on the right hand side of Eq. (B3) reduce to $2\pi J_n(ka)$ so that $F[E(\theta)]$ becomes

$$F[E(\theta)] = \sum_{n=-\infty}^{\infty} \frac{e^{ikr}}{r} J_n(ka). \quad (B-4)$$

where $J_n(ka)$ is the Bessel function of the first kind. For $n < ka$ the Bessel function is oscillatory. As n approaches ka , $J_n(ka)$ begins to decay. Specifically, the asymptotic expansion for large orders of the Bessel function is given by⁸

$$J_n \left(n + zn^{\frac{1}{3}} \right) = 2^{\frac{1}{3}} n^{-\frac{1}{3}} \text{Ai} \left(-2^{\frac{1}{3}} z \right). \quad (B-5)$$

where Ai is the Airy function.⁸ We want to learn the behavior of $J_n(ka)$ when ka is fixed. In order for ka to remain constant while n increases, z must vary according to the relation

$$z = \frac{ka - n}{n^{\frac{1}{3}}}. \quad (B-6)$$

As n becomes large z becomes a large negative number. The Airy function approaches zero quickly for arguments larger than about 3. This means that $J_n(ka)$ will become very small for $n > ka$ provided $-2^{\frac{1}{3}}z \geq 3$, or $z < -3/2^{\frac{1}{3}}$. We let $z = -3$ and ask what value of n is needed to insure that $J_n(ka)$ is insignificant compared to $(2/n)^{\frac{1}{3}}$. Table B1 lists the ka value for various values of n ($z = -3$) and the derivative* of n with respect to ka obtained by differentiating Eq. (B6) with $z = -3$. The derivative of n with respect to ka gives a truncation criterion. For example, a target of $ka = 34.33$ will not have significant frequency contribution above $n = ka \times 1.086$ or 45 modes. We can see from the table that the truncation criterion varies with ka value. The larger the ka percentage-wise the fewer the modes above ka required. This makes sense because the reactive region of a target extends a greater proportioned distance for a smaller target, and as we saw in Section 4 it is the reactive region that defines the spatial frequency band limit of an object. Thus, we have demonstrated the existence of the truncation criterion.

*For fixed ka , n increasing past dn/dka requires $z < -3$ which means the Airy function factor will become smaller.

⁸Abramowitz, M., and Stegun, I., (1970), *Handbook of Mathematical Functions With Formulas, Graphs, and Mathematical Tables*, United States Department of Commerce, Chapters 9 and 10.

Table B1. Truncation Criterion

Mode Number (n)	ka	d(n)/d(ka)
10.000000	3.536696	1.274605
15.000000	7.601364	1.196765
20.000000	11.856747	1.157034
25.000000	16.227947	1.132452
30.000000	20.678303	1.115542
35.000000	25.186802	1.103094
40.000000	29.740145	1.093492
45.000000	34.329319	1.085826
50.000000	38.947906	1.079541
55.000000	43.591145	1.074281
60.000000	48.255398	1.069802
65.000000	52.937824	1.065936
70.000000	57.636143	1.062559
75.000000	62.348511	1.059579
80.000000	67.073395	1.056927
85.000000	71.809509	1.054549
90.000000	76.555786	1.052403
95.000000	81.311295	1.050454
100.000000	86.075233	1.048675

Bibliography

- Beyer, W. H. (1984), *Standard Math Tables*, CRC Press, Sections IV and X.
- Hancock, J., and Livingston, P. (1974), *Program for Calculating Mie Scattering for Sphere, Using Kerker's Formulation, Over a Specified Particle Size Distribution*, NRL Report 7808, Naval Research Laboratory, Washington, DC.
- Harrington, R. F. (1960), Effect of Antenna Size on Gain, Bandwidth, and Efficiency *Journal of Research of the National Bureau of Standards—D: Radio Propagation*, Vol. 64D, No. 1, pp. 1-12, January-February 1960.
- Harrington, R. F. (1961), *Time Harmonic Electromagnetic Fields*, McGraw-Hill, Chapter 6.
- Ojeba, E., Bello and Walter, C. H. (1977), On the Cylindrical and Spherical Wave Spectral Content of Radiated Electromagnetic Fields *IEEE Transactions on Antennas and Propagation*, Vol. AP-27, No. 5, pp. 634-639, September 1979.
- Scientific Atlanta Series 1780 Programmable Microwave Receiver Operators Manual*, Third Edition (May 1984), Publication No. 41 R045C Manual Part No. 221705, pp. 1-8 through 1-15.



MISSION of Rome Air Development Center

RADC plans and executes research, development, test and selected acquisition programs in support of Command, Control, Communications and Intelligence (C³I) activities. Technical and engineering support within areas of competence is provided to ESD Program Offices (POs) and other ESD elements to perform effective acquisition of C³I systems. The areas of technical competence include communications, command and control, battle management information processing, surveillance sensors, intelligence data collection and handling, solid state sciences, electromagnetics, and propagation, and electronic reliability/maintainability and compatibility.